



Swansea University Prifysgol Abertawe

Mechanical Impacts of Embedded Fibre Optics in 3D Printed Structures via Fused Deposition Modelling

Nathaniel Yeo, BEng

Submitted to Swansea University in fulfilment of the requirements for the Degree of Master
of Science by Research

Swansea University

2020



Summary

This project explores the mechanical effects of embedded optical fibres in additively manufactured structures using the fused deposition modelling method. The aim is to develop a new and broad understanding of the effects these fibres have on the tensile and flexural properties of 3D printed polylactic acid. The bonding strength between the fibre and matrix material is also investigated by way of a fibre pull-out test. Micro-CT X-ray scanning is also used to visualise the internal structures of printed specimens and how different printing parameters; specifically infill pattern and infill density, impact the quality of the embedded fibre.

Infill patterns cubic, grid and triangles were examined as plain samples without fibre at low, medium, high, and maximum density. Triangle infill was chosen to be the underlying infill pattern for samples containing fibre. A concentric infill was also selected to see behaviours when infill raster lines are coaxial to an embedded optical fibre. Manual fibre laying was found to be the most suitable method for producing fibre samples.

Fibre sample variables were devised to investigate how different print settings may alter the quality of fibre embedding and mechanical properties. These included: adding extra material around the fibre, rotating the fibre, and altering the direction of raster lines over a central fibre. The type of buffer coating the optical fibre was also altered for micro-CT imaging and fibre pull-out testing.

It was found that, in most cases, a single embedded optical fibre improves tensile and flexural mechanical properties.

Declarations and Statements

DECLARATION

This work has not previously been accepted in substance for any degree and is not being concurrently submitted in candidature for any degree.

Signed:



Date:

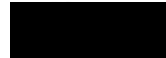
13.04.2021

STATEMENT 1

This thesis is the result of my own investigations, except where otherwise stated. Where correction services have been used, the extent and nature of the correction is clearly marked in a footnote(s).

Other sources are acknowledged by footnotes giving explicit references. A bibliography is appended.

Signed:




Date:

13.04.2021

STATEMENT 2

I hereby give consent for my thesis, if accepted, to be available for photocopying and for inter-library loan, and for the title and summary to be made available to outside organisations.

Signed:



Date:

13.04.2021

Contents

Summary	2
Declarations and Statements	3
Contents	4
Acknowledgements	8
Lists of Figures, Tables and Equations	9
Figures	9
Tables	11
Equations	12
Abbreviations	12
1 Introduction	13
1.1 Objectives	14
2 Technical Overviews	15
2.1 Additive Manufacturing	15
2.1.1 A Brief History of 3D Printing	16
2.1.2 Methods of Additive Manufacture	16
2.1.3 Hybrid Manufacturing	22
2.1.4 Additive Manufacturing Materials	23
2.1.5 Software	24
2.1.6 Advantages and Disadvantages of Additive Manufacturing	26
1.1 Optical Fibres	28
2.1.7 Manufacture	29
2.1.8 Applications	29
2.2 X-ray Micro-CT Imaging	31
2.2.1 Gathering μ CT Image Data	32
2.2.2 Reconstruction	33

2.2.3	Image Analysis.....	33
3	Literature Review.....	34
3.1	ECHOES by AV Optics Ltd.....	34
3.1.1	Printed Optical Waveguides.....	34
3.1.2	Fibre Embedding in Additive Manufacturing.....	36
3.1.3	Guideways for post-print fibre insertion.....	37
3.1.4	Incorporated Optical Connectors.....	38
3.1.5	ECHOES Research Summary.....	40
3.2	Academic Literature.....	41
3.2.1	Mechanical Properties of FDM Structures Printed in PLA Without Fibre.....	41
3.2.2	Reinforcing Fibre Integration Process in FDM Additive Manufacturing.....	44
3.2.3	Optical Fibre Integration in FDM.....	46
3.3	Academic Research Summary.....	48
3.4	Literature Review Conclusion.....	48
4	Methodology.....	49
4.1	Design Parameters.....	49
4.1.1	Plain Sample Types.....	49
4.1.2	Standard Fibre Infill.....	52
4.1.3	Fibre Sample Types.....	52
4.2	Fibre Details.....	54
4.3	Sample Fabrication.....	55
4.3.1	Global Parameters.....	55
4.3.2	Tensile Samples.....	58
4.3.3	Flexural samples.....	59
4.3.4	Fibre Pull-out.....	60
4.3.5	Issues Encountered.....	61
4.4	Testing.....	62
4.4.1	Micro-CT X-ray Imaging.....	62

4.4.2	Tensile	64
4.4.3	Flexural.....	65
4.4.4	Fibre Pull-out.....	67
5	Results and Discussions	70
5.1	Micro-CT X-Ray Images	70
5.1.1	A1	71
5.1.2	A2	72
5.1.3	B1, B2, B3	74
5.1.4	C1, C2, C3	78
5.1.5	E1, E2, E3.....	81
5.1.6	CT Images Summary.....	84
5.2	Tensile Results.....	85
5.2.1	Dimension Results.....	85
5.2.2	Tensile Modulus Calculation Correction	85
5.2.3	Tabulated Mean Values	86
5.2.4	Plain Samples	89
5.2.5	Plain vs. Fibre Samples Direct Comparison.....	92
5.2.6	Extra Layers	95
5.2.7	Fibre Direction.....	99
5.2.8	Tensile Mass Modulus Ratios.....	102
5.2.9	Tensile Summary	104
5.3	Flexural Results	105
5.3.1	Dimension Results.....	105
5.3.2	Manufacturing Discrepancies	105
5.3.3	Flexural Modulus Calculation Correction.....	105
5.3.4	Tabulated Values.....	106
5.3.5	Plain Samples	108
5.3.6	Plain vs. Fibre Samples	110

5.3.7	Extra Layers	112
5.3.8	Fibre Direction.....	114
5.3.9	Flexural Mass Modulus Ratios	117
5.3.10	Flexural Summary	120
5.4	Comparison with Material Vendor Specifications	122
5.5	Fibre Pull-out.....	123
5.5.1	Tabulated Values.....	123
5.5.2	Pull-Free Force	124
5.5.3	Pull-out Summary	125
5.6	Results Summary.....	127
5.6.1	Recommended Actions	127
5.6.2	Additional Considerations.....	127
6	Further Work.....	128
6.1	Improvement to the Work Done in this Project	128
6.2	Continuation of this Project	128
6.3	Future Opportunities	129
7	Conclusion.....	130
Appendices.....		132
Appendix A – Optical Fibre Specifications		132
Appendix B – Cura 4.0.0 Fibre Printing Profile Settings.....		138
Appendix C – Filament Specification.....		150
Appendix D – Tensile Modulus Correction		151
Appendix E – Flexural Modulus Correction.....		152
Appendix F - Material Vendor Print Guidance for PLA		153
Bibliography		154

Acknowledgements

Thanks to Professor Richard Johnston as my primary supervisor for his advice, guidance, and input. Also, to Dr Rhys Charles, my secondary supervisor, for his openness during discussions.

Thanks to Andrew Lee and Ian Read as contacts from AV Optics for their input and insight from an industrial perspective.

Thanks to Dr Feras Korkees and Dr Sue Alston for a great deal of recommendation, specifically regarding composite testing and data calculations.

And thanks to Dr Ria Mitchell, for her time spent scanning X-ray specimens, and Jeremy Davies for allowing me free reign in the 3D printing lab.

The author would finally like to acknowledge the funding from the European Social Fund via the Welsh Government, the Engineering and Physical Sciences Research Council and AV Optics Ltd that has made this research possible.

Lists of Figures, Tables and Equations

Figures

Figure 2.1.1:1 Subtractive vs. additive manufacturing workflows	15
Figure 2.1.2:1 Vat Photopolymerization	17
Figure 2.1.2:2 The Material Extrusion process	18
Figure 2.1.2:3 Material Jetting process.....	19
Figure 2.1.2:4 Binder Jetting process.....	20
Figure 2.1.2:5 The Powder Bed Fusion process	21
Figure 2.1.5:1 Example of Ultimaker Cura slicing software	26
Figure 2.1.6:1 Optical fibre cut-away.....	28
Figure 2.1.8:1 μ CT process flow chart.....	31
Figure 3.1.1:1 SLA printed waveguide test structure	35
Figure 3.1.1:2 The second iteration of an SLA printed waveguide	36
Figure 3.1.2:1 Concept showing fibre the management	37
Figure 3.1.3:1 FDM printed bracket demonstrating integrated guides for fibres	37
Figure 3.1.4:1 Two concepts for integrated optical connectors.....	38
Figure 3.1.4:2 Printed connectors with friction fit POF	39
Figure 3.1.4:3 POF inserted into printed aluminium housing.....	40
Figure 3.2.2:1 3 potential ways to integrate fibre into an FDM printer	45
Figure 4.1.1:1 Infill patterns and varying densities are shown in slicer software	51
Figure 4.1.1:2 Printed infill examples	51
Figure 4.3.1:1 Cura infill adjustment.....	56
Figure 4.3.1:2 Ultimaker 2+ FDM printers	56
Figure 4.3.1:3 A tensile sample with affixed fibre just after print resume	58
Figure 4.3.2:1 Tensile specimen dimensions	59
Figure 4.3.2:2 Tensile specimen paused at the mid-layer for fibre insertion.....	59
Figure 4.3.3:1 Flexural sample dimensions.....	60
Figure 4.3.3:2 Flexural samples paused mid-print.....	60
Figure 4.3.4:1 Fibre pull-out samples just after the print resume.....	61
Figure 4.4.1:1 Chamber of the Nikon XT H 225	62
Figure 4.4.1:2 Nikon XT H 225 gun, and detector.....	63
Figure 4.4.2:1 Tensile test setup.....	65
Figure 4.4.3:1 Flexural testing underway.....	67

Figure 4.4.4:1 Retention apparatus for fibre pull-out	68
Figure 4.4.4:2 Specimen in fibre pull-out test rig	68
Figure 4.4.4:3 Fibre pull out sample fully secured in the test rig	69
Figure 4.4.4:1 Axis planes in ORS Dragonfly in 3D model view	70
Figure 5.1.1:1 Sample A1 CT slices.....	71
Figure 5.1.2:1 Sample A2 CT slices.....	73
Figure 5.1.3:1 Sample B1 CT slices.....	75
Figure 5.1.3:2 Sample B2 CT slices.....	76
Figure 5.1.3:3 Sample B3 CT slices.....	77
Figure 5.1.4:1 Sample C1 CT slices.....	78
Figure 5.1.4:2 Sample C2 CT slices.....	79
Figure 5.1.4:3 Sample C3 CT slices.....	80
Figure 5.1.5:1 Sample E1 CT slices	81
Figure 5.1.5:2 Sample E2 CT slices	82
Figure 5.1.5:3 Sample E3 CT slices	83
Figure 5.2.2:1 5.2.2 Tensile modulus calculation correction	86
Figure 5.2.4:1 Tensile modulus vs. infill parameters for all plain samples	89
Figure 5.2.4:2 UTS vs. infill parameters for all plain samples	90
Figure 5.2.4:3 0.2% Proof Stress vs. infill parameters for all plain values	91
Figure 5.2.5:1 Tensile modulus comparison between plain and fibre samples	92
Figure 5.2.5:2 UTS comparison between plain and fibre samples	93
Figure 5.2.5:3 0.2% proof stress direct comparison between plain and fibre samples.....	94
Figure 5.2.6:1 Tensile modulus vs. extra layers	95
Figure 5.2.6:2 Comparison of UTS when extra solid layers are introduced	96
Figure 5.2.6:3 Proof stress vs. extra layers	97
Figure 5.2.6:4 Comparison of tensile modulus values of samples with additional layers.....	98
Figure 5.2.7:1 Comparison of tensile modulus values with fibre rotation	99
Figure 5.2.7:2 UTS vs. fibre direction.....	100
Figure 5.2.7:3 0.2% proof stress vs. embedded fibre direction.....	101
Figure 5.2.8:1 Tensile mass modulus ratios for plain and fibre samples.....	103
Figure 5.3.3:1 Stress-strain plot for a plain 40% triangle flexural specimen	106
Figure 5.3.5:1 Flexural modulus of all plain samples.....	108
Figure 5.3.5:2 Flexural strength values for plain samples	109
Figure 5.3.6:1 Flexural modulus comparison of equal samples with and without fibre	110
Figure 5.3.6:2 Flexural strength values of plain and fibre equivalent samples.	111

Figure 5.3.7:1 Flexural modulus vs. additional layers.....	112
Figure 5.3.7:2 Flexural strength vs. additional 100% infill layers	113
Figure 5.3.8:1 Change in flexural modulus with fibre direction	114
Figure 5.3.8:2 45° fibre options with triangular infill.....	115
Figure 5.3.8:3 Flexural strength vs. fibre direction.....	115
Figure 5.3.9:1 Flexural mass modulus ratios	118
Figure 5.5.2:1 Force displacement curve for samples B1a, B2b and C1a. B1a	124
Figure 5.5.2:2 Pull-free force per unit length for each tested sample.....	125

Tables

Table 2.1.6-1 Some advantages and disadvantages of additive manufacturing.	27
Table 3.2.1-1 Summary of some of the previous research findings	43
Table 4.1.1-1 Infill parameters for plain samples.	50
Table 4.1.3-1 Parameters and testing methods for fibre samples	53
Table 4.1.3-1 Optical fibre details.....	54
Table 4.4.2-1 Summary of tensile testing parameters.....	64
Table 4.4.3-1 Summary of flexural testing parameters	66
Table 4.4.4-1 Summary of fibre pull-out testing parameters	69
Table 5.1.1-1 Sample A1 μ CT details.....	71
Table 5.1.2-1 Sample A2 μ CT details.....	72
Table 5.1.3-1 Samples B1, B2 and B3 μ CT details.....	74
Table 5.1.4-1 Samples C1, C2 and C3 μ CT details.....	78
Table 5.1.5-1 Samples E1, E2 and E3 μ CT details.....	81
Table 5.2.1-1 Tensile specimen dimensional conformity.	85
Table 5.2.3-1 Mean values for plain samples tensile results	87
Table 5.2.3-2 Mean values for fibre samples tensile results.	88
Table 5.2.8-1 Tensile mass modulus ratio values for plain and fibre samples	102
Table 5.3.4-1 Flexural results for plain samples	107
Table 5.3.4-2 Flexural results for fibre samples.....	107
Table 5.3.9-1 Mass modulus ratios for flexural samples.	117
Table 5.3.10-1 Vendor material specifications vs. experimental result	122
Table 5.5.1-1 Mean values for fibre pull-out testing	123

Equations

Equation 1	66
Equation 2	66

Abbreviations

ALM	Additive Layer Manufacturing
AM	Additive Manufacturing
CAD	Computer Aided Design
CNC	Computer Numerically Controlled
DED	Directed Energy Deposition
DLP	Digital Light Projection
DMLS	Direct Metal Laser Sintering
FBG	Fibre Bragg Grating
FDM	Fused Deposition Modelling
FFF	Fast Filament Fabrication
LOM	Laminated Object Manufacturing
Micro-CT/ μ CT	Micro Computed Tomography
MMR_F	Flexural Mass Modulus Ratio
MMR_T	Tensile Mass Modulus Ratio
PBF	Powder Bed Fusion
PLA	Polylactic Acid
POF	Polymer Optical Fibre
SFI	Standard Fibre Infill
SHS	Selective Heat Sintering
SLA	Stereolithography
SLM	Selective Laser Melting
SLS	Selective Laser Sintering
UAM	Ultrasonic Additive Manufacturing
UTS	Ultimate Tensile Strength

1 Introduction

Additive manufacturing (AM), commonly referred to as 3D printing, is a relatively new manufacturing technology and is becoming more widespread in industrial and design environments [1]. The layer-by-layer process of AM leads to key advantages over traditional subtractive methods, one of these benefits being the ability to embed additional elements, at any stage, into a printed component [2].

As demand for advanced materials and structural design becomes ever more sophisticated, the ability to embed sensors capable of monitoring internal properties of components and structures [3] enables engineers and operators to monitor the conditions inside otherwise inaccessible areas. With this facility, the creators of such structures can push the boundaries of design in the knowledge that they will be able to observe and quantify what is happening inside over time.

One such element capable of being embedded into a 3D printed part and acting as a sensor is an optical fibre [4]. Optical fibres are designed to transmit data via pulses of light, resulting in greater speeds and bandwidths over traditional metallic cables. Optical fibres can also be used to produce a type of sensor known as a Fibre Bragg Grating (FBG). The small size of FBGs, their immunity to electromagnetic interference and their ability to withstand harsh environments makes them a great candidate for embedding into additively manufactured components.

However, due to the young age of AM technology, gaps exist in the knowledge base regarding the combination of additive manufacturing and fibre optic technologies. One such gap is the mechanical effects an optical fibre may have on a 3D printed component or structure.

This project will investigate and present the mechanical impacts associated with embedding an optical fibre into additively manufactured structures. Fused Deposition Modelling (FDM) is the chosen 3D printing method due to its availability and ease of use. Mechanical testing will be carried out via suitable standards to determine the mechanical changes caused by the embedded optical fibre. A new test method is also developed to investigate the required forces to pull the fibre free from the encapsulating material, and finally, micro-CT scanning is used to investigate the fibre-matrix interface and visualise internal structures.

The research presented provides insight into the mechanical impacts an optical fibre has on a 3D printed structure and also aids in the understanding and development of embedded fibre optics to produce multi-functional or smart components via FDM.

AV Optics is an independent, specialist company supplying photonic solutions for use within harsh environments, including fibre optics. They see opportunities in AM with embedded fibre optics and have supported this project as an industrial sponsor.

1.1 Objectives

The following list specifies the intended goals of this research project.

- Present outlines of the 3 major technologies used within this project: Additive Manufacturing, Fibre Optics and Micro-CT imaging.
- Summarize research presented by AV Optics regarding the combination of additive manufacturing and fibre optic technologies within their ECHOES report.
- Investigate and present existing literature to determine the current state of the art regarding the mechanical impacts of embedded fibre optics within an FDM 3D printed structure.
- Utilizing literature findings, produce a methodology for relevant testing that will advance the current knowledge base.
- Display, describe, discuss, and summarise results findings.
- Explore how this project and its findings may be used to conduct or aid further research.

2 Technical Overviews

This Chapter is targeted at presenting an outline of the 3 key technologies brought together for this project: Additive Manufacturing, Fibre Optics and X-ray Micro Computed Tomography Imaging.

2.1 Additive Manufacturing

Additive manufacturing (AM), additive layer manufacturing (ALM), or more commonly known as 3D printing^a, is a method of digital fabrication employing the deposition and accumulation of multiple material layers to produce a digitally specified part. This is opposed to subtractive manufacturing techniques which rely on the removal of material from an oversized stock piece to form the same part. Figure 2.1.1:1 depicts a simplified comparison of additive and subtractive workflows.

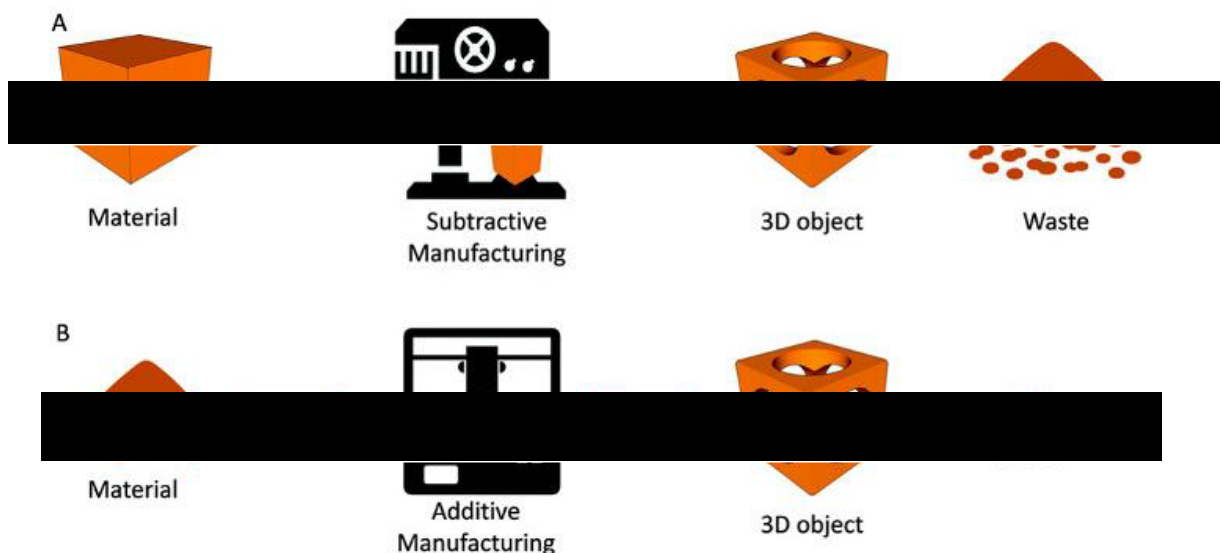


Figure 2.1.1:1 Subtractive vs. additive manufacturing workflows. As indicated by the flow diagram, AM can reduce the waste produced significantly. [5]

AM is a direct digital manufacturing method, as such final component design must be completed in Computer Aided Design (CAD) software to allow Computer numerically Controlled (CNC) hardware to realize the physical component. Direct digital manufacturing workflows offer numerous qualities including allowing designed parts to be sent directly to a remote printer with little to no machine interaction and minimal operator training. AM also allows the fabrication of multiple designs without the need for multiple machines, different tooling, jig fixtures or further operator training. 3D printing has many more benefits over

^a This document will use the terms AM, 3D printing and ALM interchangeably.

traditional manufacturing techniques, such as reduced waste and ‘free complexity’, but also exhibits drawbacks, one example being a lack of standardisation. Further pros and cons are detailed in Section 2.1.6.

There exist 7 top-level categories of AM processes defined by ASTM International (American Society for Testing and Materials), each having an assortment of pros and cons. Each category process along with brief introductions to the history, materials, software, and some general advantages and drawbacks will be outlined below.

2.1.1 A Brief History of 3D Printing

The first 3D printer was developed by Charles Hull utilizing the stereolithography process, (Section 2.1.2.1) with a patent issued in 1984 [6]. The patent for fused deposition modelling (Section 2.1.2.2) was assigned in 1989 to Stratasys and co-founder Scott Crump [7]. Both 3D Systems, co-founded by Charles Hull, and Stratasys are still major companies within the AM industry.

In 2009 patents on the fused deposition modelling process expired, allowing individuals, such as Dr Adrian Bowyer, the instigator of the RepRap movement, and companies alike to further develop innovative new processes and machines. The goal of the RepRap movement was to produce a system capable of replicating itself by printing individual parts for a user to assemble. 2009 also saw the establishment of the ASTM Committee F42 [8] for additive manufacturing technologies, which have developed standards for processes, design, materials, terminology and more.

Many aspects of additive manufacturing have advanced significantly since 2009, to a point where components for prosthetics, turbo chargers, rocket engines [9,10] and even human organs can be manufactured via 3D printing.

The 3D printing market was estimated to be USD 8.58 billion in 2018 [11], USD 11.58 billion in 2019 [12] and anticipated to reach USD 34.8 billion by 2024 with metal-based technologies accounting for the majority of the market share [13].

2.1.2 Methods of Additive Manufacture.

Numerous different additive manufacturing technologies exist which have been categorized into 7 core groups: Vat Photopolymerization, Material Extrusion, Material Jetting, Binder Jetting, Powder Bed Fusion, Directed Energy Deposition and Sheet Lamination. Many of the methods within each category have proprietary industry names, along with the continual development of new technologies. The ASTM F42 and ISO/TC (International Organization for

Standardisation/Technical committee) 261 have defined standards and general principles for the range of additive manufacturing technologies. ISO ASTM 52900:2017 [14] specifically defines the process categories used to group the different AM method. The following section gives an overview of the 7 groups of additive manufacturing processes.

2.1.2.1 Vat Photopolymerization

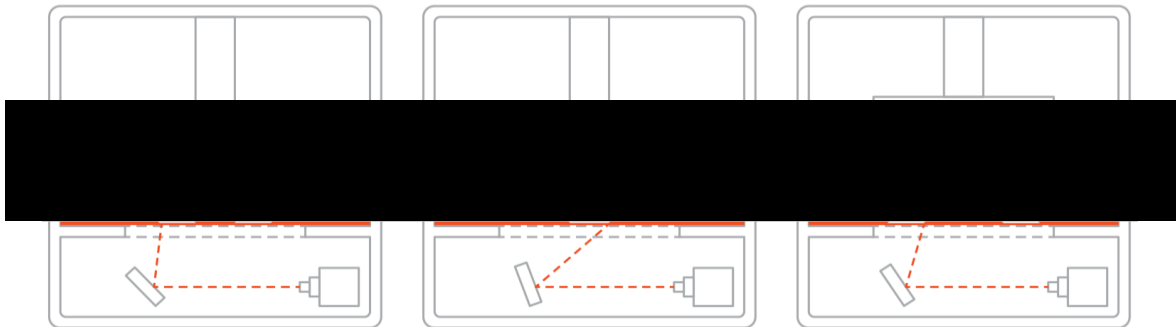


Figure 2.1.2:1 Vat Photopolymerization. The images show a laser scanning SLA system in which a mirror assembly (mirror galvanometer) is used to control the laser direction. [15]

Vat photopolymerization exploits photosensitive liquid polymer feedstock, known as resin, which is selectively cured to produce a solid part. Stereolithography (SLA) and Digital Light Processing (DLP) are both methods of vat photopolymerization. SLA utilizes a precisely controlled scanning laser (Figure 2.1.2:1) to cure the resin, whilst DLP uses a digital projector screen to cure entire layers at a time. Both methods have their benefits over the other but utilize the same resin curing principle. Once each layer has been exposed to UV light and cured, the build platform moves a 'one-layer height' distance away from the liquid vat and the process repeats until all layers have been completed. SLA is sometimes used to refer to Vat Photopolymerization processes in general.

SLA is capable of producing highly detailed and intricate parts due to the light-curing process. This has resulted in suitability for use in the dental and jewellery industry and growing interest in hobbyist consumer markets as machine price reduces.

A noteworthy requirement of Vat Photopolymerization is the often necessary post-print processing. The green-state printed part must be cleaned of any remaining uncured resin and then fully cured using a UV light source. Some systems are capable of the washing and curing phase without operator interaction, where others require separate systems and operator intervention to complete the process.

2.1.2.2 Material extrusion

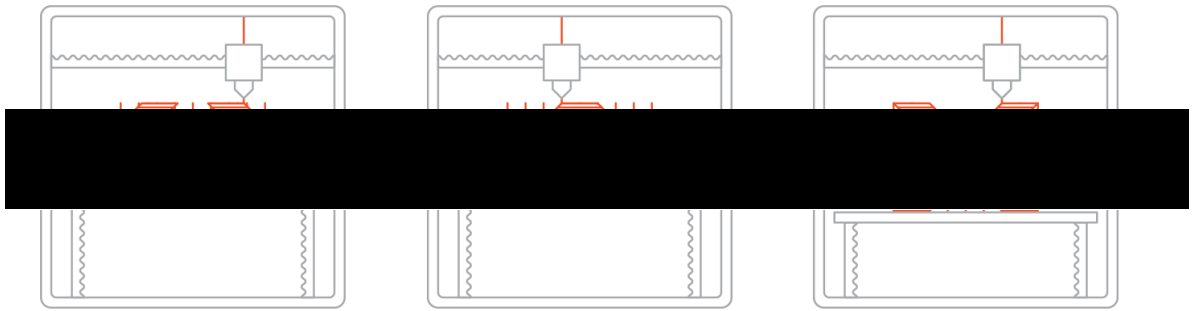


Figure 2.1.2:2 The Material Extrusion process. Vertical lines in the image represent support structures required to produce parts that would otherwise overhang in space. [16]

Material extrusion, shown above in Figure 2.1.2:2, is one of the most common methods of 3D printing for non-industrial, consumer systems. Fused Deposition Modelling (FDM) and Fused Filament Fabrication (FFF) are both material extrusion processes coined by different companies and ultimately describe the same process. In FDM stock material is most commonly in the form of a cylindrical polymer filament or as pellets for very high flow rate systems. The raw material is fed via a precise extruder system to a heated CNC extrusion head, referred to as the hot end. The hot end contains temperature sensors and heating elements capable of precisely heating the hot end to a specified temperature at which the feed stock becomes semi-molten. In this state, the extruder can drive filament out of the nozzle to deposit the material onto a build platform. The extrusion head is capable of moving in X, Y and Z axes relative to the build platform, enabling controlled deposition of material to form a layer. Once each layer is complete the Z distance is increased to allow the deposition of the next layer.

FDM machine design can vary greatly, some have stationary build plates with the extrusion head and gantry moving in all 3 axes and some move the build plate in the Z-direction whilst the hot end moves in X and Y axes. FDM systems can also be mounted to multi-axis robot arms enabling increased functionality and design complexity. These mechanical differences do not alter the core material deposition process.

Polymers are the most common feedstock material, ranging from the less costly consumer-grade PLA (Poly lactic acid) to high-end engineering materials such as PEEK (polyether ether ketone). Material suitable for FDM has also advanced with printer hardware. Filaments are available with additions such as embedded metal particles, carbon fibres, glow in the dark, flexible, conductive properties and many other options.

A standout feature of FDM is the scalability of the technology, from compact desktop systems suitable for rapid prototyping to warehouse size machines capable of printing an entire boat

hull mould [17]. Forms of material extrusion are candidates for use in future manufacturing of shelters on the Moon and Mars [18].

2.1.2.3 Material Jetting

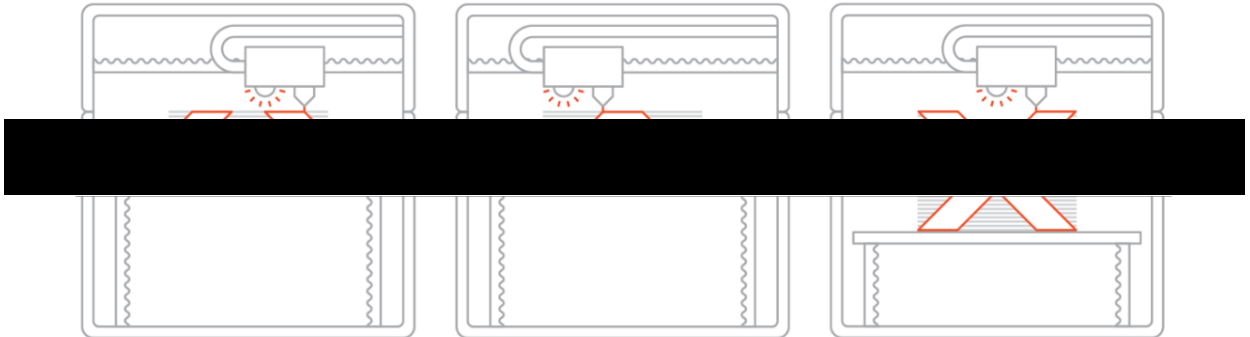


Figure 2.1.2:3 Material Jetting process, similar to inkjet printers. Precisely depositing photosensitive liquid before being immediately cured using UV light. [19]

Material jetting (MJ), Figure 2.1.2:3, systems operate similarly to 2D inkjet printers. Liquid phase photosensitive feedstock is precisely dispensed as droplets onto a build platform via a print head and cured using a UV light source, usually located on the print head. This system is referred to as Drop on Demand (DOD). Material jetted parts exhibit high dimensional accuracy with a smooth surface finish, exceedingly suitable for high-quality rapid prototyping. Materials suitable for material jetting are limited, having to be photocurable, liquid in phase and have the correct viscosity for the dispensing system. This makes MJ systems expensive and complex. Polymers and waxes are the most common feedstock and can come with a variety of properties, such as various hardness values or as dissolvable support material. Full colour and multi-material printing are also possible within a single print cycle.

Material jetting is suited to large format printers where multiple print heads or a single head spanning the entire build platform can lay down entire layers in a single pass. Due to the required complex rheology, printing parameters are often established by the material or printer manufacturer and offer little flexibility to the operator.

2.1.2.4 Binder Jetting

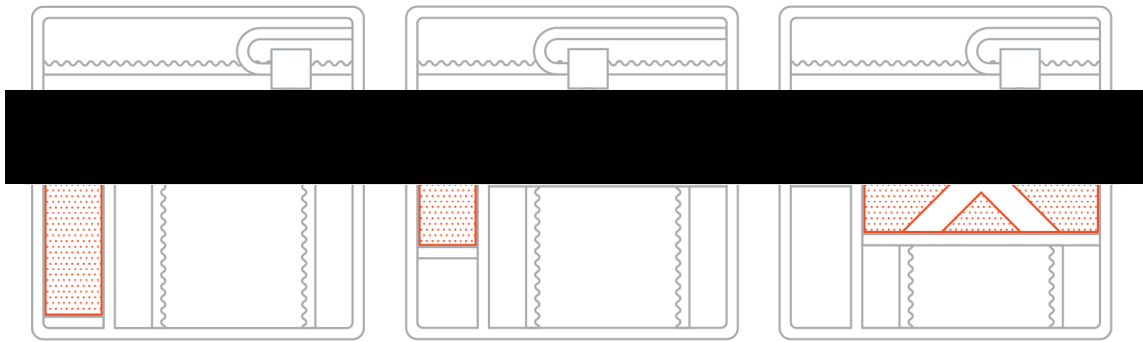


Figure 2.1.2:4 Binder Jetting process operates similarly to material jetting. Instead of depositing the build material, a binder is dispensed to hold together the powdered build material. [20]

Similar to material jetting, a Binder Jetting (BJ) print head precisely dispenses a liquid binding agent onto a bed of powdered stock material (Figure 2.1.2:4). The binder acts as an adhesive, holding together powder material in the desired geometry until printing is complete. After each layer has been completed a recoating system deposits a new layer height worth of powder across the whole build platform. This reduces the requirement for support structures and allows the entire print volume to be utilized. As in material jetting, the print head can span the entire build area allowing whole layers to be completed in a single pass. Full-colour printing can also be achieved by introducing dyes within the binder.

The benefit of having an entire build volume of powder to act as support material also leads to the downside of requiring far more feed material than is necessary for a single object. This makes optimizing the build volume crucial and why binder jetting systems are more suited to industrial-scale environments. Fine powder handling also demands additional safety considerations.

Unbound powder must be removed upon print completion and often cannot be reused unless reprocessed due to stringent quality requirements for the stock material.

Depending on the material being used and final part requirements, post-processing may be necessary. Ranging from leaving the printed component on the print bed to allow the binder to fully cure, to removing the green state component and sintering it in a furnace. Other methods involve infiltrating the structure with a lower melting temperature material to replace and burn out the binder increasing component density and strength.

Binder jetting is a 'cold' process and can be used with a variety of materials that are available in a powdered form, such as metals, ceramics, and sands suitable for casting moulds.

2.1.2.5 Powder Bed Fusion

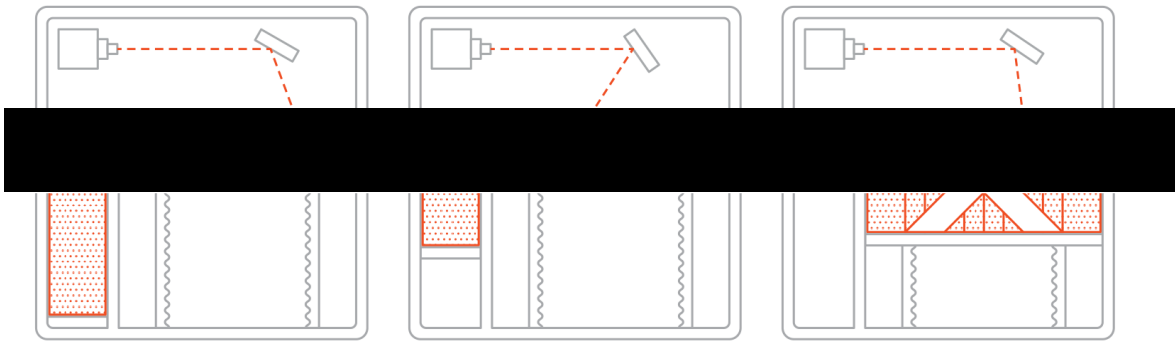


Figure 2.1.2:5 The Powder Bed Fusion process uses a high power, precisely directed heat source to selectively sinter or melt a powdered feedstock. There are several sub-categories depending on the exact process. [21]

Powder bed fusion (PBF) (Figure 2.1.2:5) is somewhat like binder jetting mixed with SLA. However, rather than using a chemical-based binder or photosensitive liquid, a high-power precisely directed heat source is used to sinter or melt the powder to form the layers. Heat sources can be in the form of lasers or electron beams and can be used to create polymer and metal components. There are several methods under the PBF umbrella: Direct Metal Laser Sintering (DMLS), Selective Heat Sintering (SHS), Selective Laser Melting (SLM) and Selective Laser Sintering (SLS). Sintering does not result in liquefaction of the material and metal-based systems require careful atmospheric control.

Due to associated costs and the capability to process metallic material, PBF is less commonly used for component prototyping. Instead, the benefits of additive manufacturing are exploited to produce functional components that cannot be or are cost-prohibitive to fabricate with traditional methods.

PBF printed components must go through post-processing steps to produce the final part. Mandatory stages involve removing unfused powder and any support structures. Surface finishing, heat treatment and machining are common optional steps to bring the final component to specification and dimension.

Some key points pertaining to PBF include the requirement for fine powder handling (pre- and post-fabrication), build chamber atmosphere control, particularly for reactive material, and the ability to work with multiple metals e.g., titanium, Inconel alloys and precious metals like gold.

2.1.2.6 Directed Energy Deposition

Directed Energy Deposition (DED) involves the deposition and fusion of feed material onto either a build platform, damaged component under repair or a part to be clad in material. Both powdered or wire stock material can be used, with heat for fusion being supplied by a

laser, plasma arc or electron beam. Whilst plastics and ceramics are available, metal is the most common feedstock material.

DED is a similar process to wire fed or spray welding techniques with the requirement of CNC systems. Compared to the other techniques discussed, DED is most often used in conjunction with a multi-axis robot arm allowing material deposition in any direction, particularly useful for the repair or cladding of complex geometry components. DED can be used to clad structures with a more costly and optimum surface material whilst the bulk material can be selected to keep costs to a minimum. The use of robot arms also allows a potentially unlimited build volume by repositioning the arm, although environmental control must still be regarded.

DED is regularly used along with CNC machining to produce the final shape dimensions and surface finish, in a hybrid manufacturing process (Section 2.1.3).

2.1.2.7 Sheet lamination

Sheet lamination involves the layering and binding of sheet material, either paper-like material in Laminated Object Manufacturing (LOM) or metal foils in Ultrasonic Additive Manufacturing (UAM). The LOM process utilizes a simple adhesive and is not used for structural purposes due to a lack of mechanical properties. UAM can join dissimilar metals together using ultrasound and pressure to weld sheets to one another.

UAM feed material is supplied in sheet or tape format, hence subtractive machining is often required in between additive phases to produce the final net shape. The use of sheet stock material enables UAM to lay and fuse large amounts of material quickly to produce significantly sized structures. Machining steps are only required to shape the structure outline rather than the entire cross-section.

2.1.3 Hybrid Manufacturing

Hybrid manufacturing refers to the combination of additive and subtractive methods to fabricate a component, usually within a single machining system. The allowable complexity and other benefits associated with AM are used to produce a near-net-shape component whilst giving less consideration to the drawbacks of dimensional tolerances or surface finish. Subtractive machining steps compliment the additive process at key stages to produce the required dimensional specifications and surface finishes. A final component can be produced with the complexity and material efficiency derived from AM but with the dimensional tolerances and surface finish of a subtractively machined part.

2.1.4 Additive Manufacturing Materials

3D printing was originally developed using a polymer-based photocurable resin. Current technologies are pushing the limits of materials available for additive manufacturing, with companies and academics developing ever more advanced and specialised materials for demanding applications.

The following section is by no means an exhaustive list of available materials but highlights part of the wide selection of materials.

2.1.4.1 Polymers

Polymers are a commonly used feedstock in the majority of the 7 AM methods. Some common materials used in FDM include PLA (Polylactic acid), ABS (acrylonitrile butadiene styrene), PETG (polyethylene terephthalate glycol) Nylons, TPEs (Thermoplastic elastomers), PC (Polycarbonate) and PEEK (Polyether Ether Ketone). Each material has varying properties giving rise to differing suitability for certain applications. Other key considerations include print process requirements, safety concerns, post processability and cost. Material modifications can be made at a chemical level to alter properties, such as thermal resistance, flexibility, hardness or print quality. Additives can be employed to alter properties like electrical conductivity, magnetism, or mechanical characteristics. Polymers are also seen in Vat Photopolymerization, Material Jetting, Binder Jetting and PBF.

2.1.4.1.1 PLA

PLA (Polylactic acid) is the material of choice for this project^b. PLA is one of the most common materials used in consumer-orientated FDM 3D printing due to its ease of printing and low cost. It is a bioplastic, derived from plant matter, such as corn, sugar beet, potatoes, and wheat. Whilst PLA is often suggested to be biodegradable the conditions required for this process are generally unrealistic in a natural environment. In reality, industrial conditions with controlled pH, moisture, microbial activity and temperature are required for PLA breakdown [22].

2.1.4.2 Metals

Metal AM is of generally greater interest to the industry over polymers due to the favourable mechanical characteristics. The advancement in material design, hardware capabilities and process control enable functional components to be produced from metals where plastics would only be suited for prototyping.

^b Specific material specifications are shown in Appendix C – Filament Specification.

Metals such as stainless steels, aluminium, titanium, nickel alloys, and cobalt alloys are all available for use in AM. Coupling advanced metal materials with AM allows the fabrication of highly complex, lighter, and stronger components, which cannot be realised with traditional machining methods. Precious metals such as gold, silver and platinum are also available for use in specialist applications or the jewellery industry.

2.1.4.3 Ceramics

Ceramics are most often associated with binder jetting due to their high melting temperatures and the lack of required heat in the process. However, ceramics are seeing growing use in SLA, FDM and PBF technologies as material and process design improves. AM of ceramics enables the manufacture of components where other materials would be infeasible whilst retaining the ability to produce complex geometries, for example in the dental industry [23].

2.1.4.4 Concrete

Large format and mobile 3D printers have been designed to utilize concrete as a feed material. This enables the production of multiple meter-sized structures, such as bridges [24] or affordable housing [25].

2.1.4.5 Biomaterials

Biomaterials suitable for 3D printing are a highly active topic of research and development with the potential to revolutionise the medical sector [26–28].

2.1.5 Software

As a direct digital manufacturing method, AM would not be possible without supporting software. Modern computers and user-friendly software packages enable individuals to develop and produce components, particularly with the wide array of open-source, free applications available.

There are 3 major stages of software required for AM:

- a) 3D modelling.
- b) Slicing.
- c) Hardware operation.

3D CAD modelling is common to both additively and traditionally manufactured parts. Once the desired part has been conceptualised it must be generated in 3D CAD software. Components destined for additive manufacture must be designed in a way to be suitable for

the method of production. A good example is minimising overhanging geometry when using the FDM method or including resin drain holes for parts destined for SLA.

The model can be additionally subjected to Finite Element Analysis (FEA) as required to further refine the design. Some CAD packages include FEA capability, or more specialised options are available. A distinctive difference when analysing a part intended for additive manufacturing is the intrinsic laminate nature of the structure. An FEA study not intentionally specified for 3D printed parts may produce significantly inaccurate results. The array of possible print options leads to FEA of AM parts being challenging. Process simulation is also a key factor for the optimisation of industrial systems.

Upon design finalization, the digital part must then be exported into software capable of converting the 3D body into the multiple layers or slices suitable for the selected printing process^c. This software is known as a slicer and can alter an enormous number of parameters to optimize the printing process. Different methods of AM require vastly different process parameters, as such there exist many open source and proprietary slicing software packages. One example is shown in Figure 2.1.5:1 below. More complex printing methods like Material Jetting are hardware and material optimised and often have closed or proprietary software with far less customisable parameters. Enthusiast level technologies such as FDM and SLA have a multitude of open-source options available with a huge number of user-controllable variables. Operator interaction with either individual or multiple machines also relies on software to allow efficient operation.

The file formats used to transfer the digital files between the various software is another consideration. The way the file type handles the 3D model is not trivial and can ultimately impact the quality of the final part [29]. Many 3D formats exist, including STL, OBJ, AMF and 3MF.

The Standard Tessellation Language (STL) is one of the most commonly used formats and dates back to the inception of 3D printing. STL functions by creating a tessellating mesh of triangles on the model's surface resulting in an approximate interpretation of the surface geometry. Smaller triangles can be used to produce a more accurate approximation at the cost of increased file size, particularly for curved regions. A major drawback of the STL format in the modern AM landscape is the inability to store additional object data such as colour, material, and textures. Newer formats such as AMF (Additive Manufacturing Format) and

^c Some CAD software packages have integrated slicer functions.

3MF (3D Manufacturing Format) have been developed to address these issues, amongst others, to allow the support of further details such as those stated above and others like orientation, and densities.

However, even as a technologically weaker format, STL is still the most common file format used in the hobbyist space.

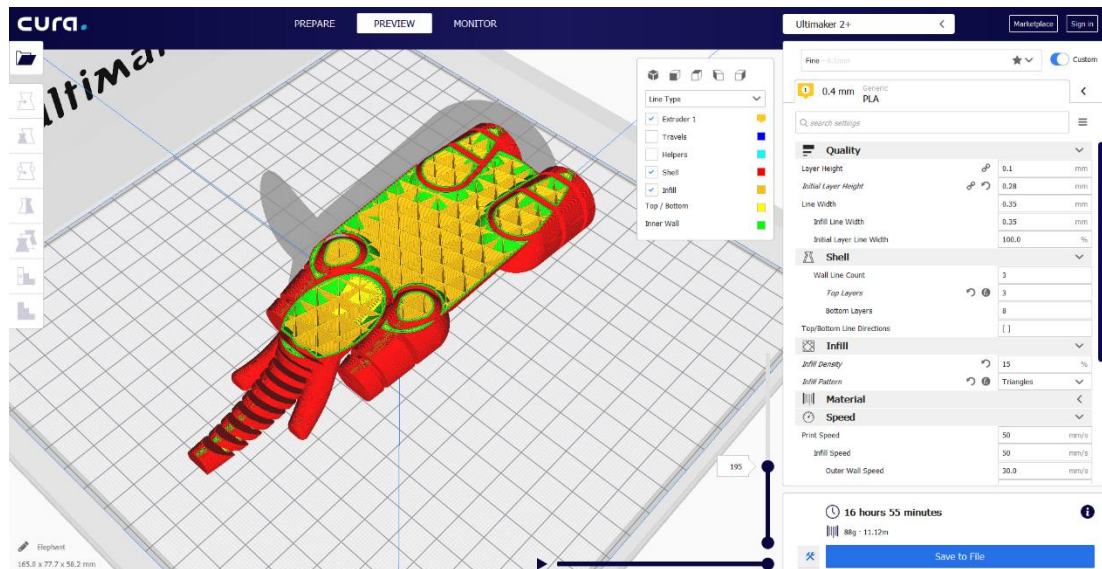


Figure 2.1.5:1 Example of Ultimaker Cura slicing software. This shows how the object has been sliced into discrete layers to form the part. In this view, the different colours represent different line types.

2.1.6 Advantages and Disadvantages of Additive Manufacturing

Table 2.1.6-1 outlines several general benefits and drawbacks of additive manufacturing. Whilst all the listed pros and cons apply to AM as a whole, each 3D printing process can exhibit different pros and cons to a greater or lesser extent.

Table 2.1.6-1 Some advantages and disadvantages of additive manufacturing.

Advantages	Disadvantages
<p>Rapid Prototyping <i>Desktop sized printers allow designers to produce working prototypes quickly, even within an office environment.</i></p>	<p>Lesser Mechanical Properties <i>Mechanical properties of 3D printed parts are generally poorer than those of parts manufactured by traditional subtractive means.</i></p>
<p>Direct Digital Manufacturing <i>3D printers require digital files to produce an object. The use of digital media allows the sharing of designs to be highly accessible anywhere in the world.</i></p>	<p>Limited Build Volume <i>Some printing processes and materials requiring controlled atmospheres can limit the size of the build chamber enclosure.</i></p>
<p>Machine Training Requirements <i>Industrial systems often restrict operator input. Instead, printing parameters are set by the material or machine manufacturer. Reduction in operating complexity allows for lower entry training and improved ease of use.</i></p>	<p>Lack of Standardization <i>Due to the relatively young age of AM technology, the standardization and characterization of 3D printed components are still in their infancy.</i></p>
<p>Free Added Complexity <i>More complex geometry does not require altering the AM process. Overhanging shapes in methods such as FDM may require support material. Products produced via powder bed methods can be highly complex with only increased processing time required.</i></p>	<p>Post-Processing <i>More complex models may require supporting material. Once printing has completed this support material must be removed, adding an extra processing step leading to increased fabrication time and cost. Powder based methods require extensive health and safety for powder handling.</i></p>
<p>Material Flexibility <i>A wide selection of materials suitable for 3D printing exists. Processes such as material jetting can lay multiple materials and/or colours in a single print e.g. a soluble support material alongside the bulk material.</i></p>	<p>Design Simulation <i>The layered structure of 3D printed parts is not always considered in FEA, leading to inaccurate modelling results.</i></p>
<p>Dissimilar Parts/Materials Concurrently <i>Large area print beds can accommodate multiples of the same part or several different parts. Combined with material flexibility different parts can be printed concurrently in different colours or materials.</i></p>	<p>Volume Production <i>High volume production runs of a single part are generally not suited to AM methods due to restrictions such as build volume and processing time.</i></p>
<p>Reduced Tooling <i>Multiple tools and machines required to produce a component can be reduced to a single 3D printer. Multiple tool heads can exist on a single printer and be automated. Some AM methods sometimes require secondary systems, such as vat photopolymerization needing to be washed and fully cured in UV light post-printing.</i></p>	<p>File Security <i>Digital models and design files are required for AM. Whilst this allows easy sharing of files for remote manufacturing, protected IP or sensitive designs must be safeguarded to prevent unlimited sharing via the internet or other means.</i></p>

1.1 Optical Fibres

Optical fibres generally refer to a type of signal wire capable of transmitting data via light pulses, using a glass or polymer-based waveguide. Figure 2.1.6:1 shows a cut away of a single fibre. Properties of light are harnessed to create a total internal reflection within the fibre core, allowing the transmitted light to 'bounce' through the length of the cable. To create this total internal reflection a layer surrounding the core, called cladding, is employed. The cladding is designed to have a lower refractive index than that of the core material causing light pulses to be reflected at the core-cladding interface, as opposed to leaving the core. In some applications, such as telecommunications, many of these fibres can be bundled together to form a cable.

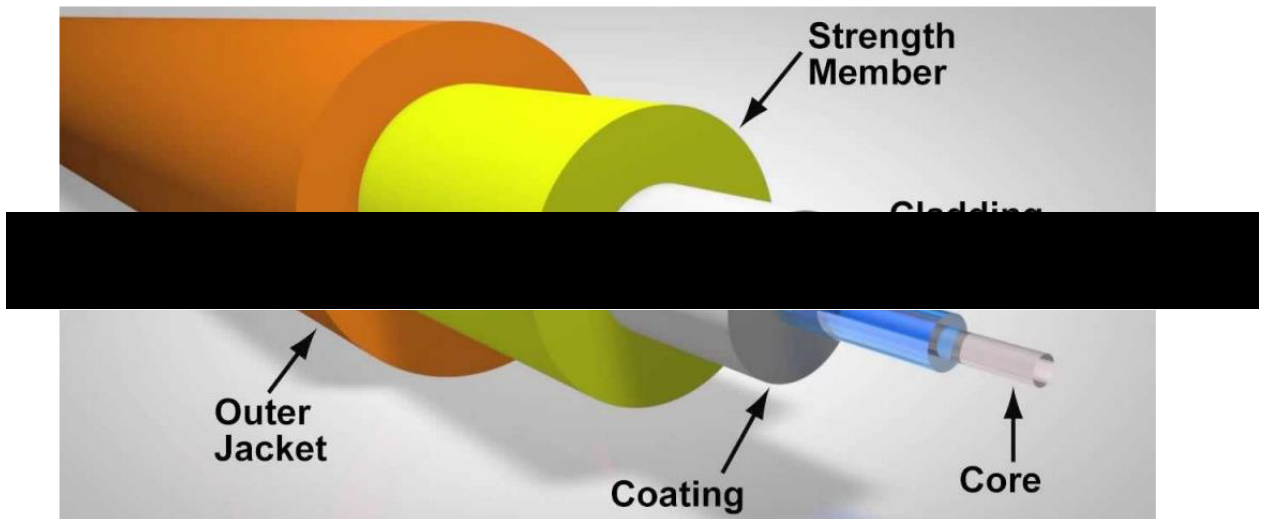


Figure 2.1.6:1 Optical fibre cut-away showing the basic composition of a single core fibre optic. Each layer can vary in diameter and material depending upon the application and environmental requirements. [30]

Silica glass-based core/cladding material is commonly used. The cladding being ultra-pure glass whilst the core is doped to obtain the desired optical properties. Polymer-based optical fibres are also available with their own set of merits and drawbacks but are not part of this overview.

There are two main types of optical fibres: single-mode and multi-mode. Single-mode fibres are designed around a smaller core diameter which constrains light pulses to travel relatively straight down the centre of the fibre. Multi-modal fibre cores are significantly larger making it easier to couple light into the fibre by allowing light to travel via multiple paths. These paths have slightly different lengths, causing light pulses to spread out and reduce in amplitude. Thus, the drawback of multi-modal fibres is a shorter available transmission distance. Single-

mode fibre core diameters are commonly $\sim 9 \mu\text{m}$ whilst multi-mode fibre cores are available as $50 \mu\text{m}$ or $62.5 \mu\text{m}$ diameters.

2.1.7 Manufacture

Glass optical fibres are commonly manufactured from ultra-pure silica glass, although other materials are utilized for specialized applications. The starting material can also be doped to obtain more specific properties, such as altering the refractive index.

Commonly, optical fibres are created by drawing a single fibre from a larger diameter component known as a preform, manufactured via modified chemical vapour deposition. The preform cross-section is produced to match the desired cross-section of the final fibre. The preform is then precisely heated and a series of pulleys are used to draw out the fibre in an apparatus known as a drawing tower. The diameter of the new fibre is repeatedly measured utilizing lasers and used to determine the speed of the drawing process to maintain an exact fibre diameter. Once the fibre has been created a buffer material can be applied over the bare fibre. The buffer material is designed to protect the fragile glass core and cladding from mechanical stress and external interference, it can also be coloured for use in multi-core cables. The buffer can be applied during the drawing process and consists of different materials depending on use, such as polyimide or acrylate. After the buffer, many more layers can be applied depending on the cable's final application and environment. These further layers do not aid in optical transmission but act as a mechanical or chemical defence.

Fibre termination and splicing are further complex topics that will not be explored.

2.1.8 Applications

The high bandwidth of fibre optic cables lends well to many applications and industries which rely heavily on high data transfer rates. Modern internet, cloud storage/computing and television infrastructure are all examples.

The medical industry deploys optical fibres designed to enter the human body where flexibility and miniaturization are key. Optical fibres in these scenarios offer high-quality video and light transmission.

Immunity to electromagnetic (EM) radiation enables reliable performance in high EM interference environments. Military applications benefit well from replacing metallic cabling with fibre, reducing the impact of potential electronic-based attacks. High-quality audio-visual transmission also benefits from the use of fibre optics where interference from other nearby equipment is mitigated.

Another key use of fibre optics is for sensing duties. Optical fibres can be used to sense temperatures, strains, pressures, and other quantities depending upon fibre design. One type of fibre optic sensor is the Fibre Bragg Grating.

2.1.8.1 Fibre Bragg Grating

A Fibre Bragg Grating (FBG) is a purposely designed and implemented periodic imperfection in the core of an optical fibre. This permanent imperfection is capable of reflecting or blocking selectively desired wavelengths. The affected wavelength(s) is known as the Bragg wavelength(s), whilst the remaining wavelengths are unaffected. This allows an FBG containing fibre to act as a filter or reflector depending upon the type of sensing duty required and the position within a component. For example, a reflecting type FBG sensor could be embedded within a structure where access to only one end of the fibre for monitoring is available.

External forces such as strain or temperature alter the dimensions of the FBG causing a shift in the Bragg wavelength which is detected by equipment known as an interrogator. Multiple FBGs can be inscribed allowing an array of sensing locations or multiple sensors of differing capabilities within a single fibre.

FBGs are often made using precise laser exposure which permanently alters the refractive index at that point in the core. The periodic index alteration and hence the properties of the FBG are dictated by the inscribed pattern, which can be configured to suit differing applications.

The small nature and versatility of FBG containing fibres make them ideal for embedding into composite or additively manufactured structures. Fully embedded FBG sensors allow for sensing of intrinsic structural properties as opposed to surface conditions collected by traditional face-mounted sensors.

2.2 X-ray Micro-CT Imaging

Micro Computed Tomography (micro-CT/ μ CT) is an X-ray based, non-destructive^d 3D imaging technique. It enables the gathering and interpretation of volumetric data non-invasively. The data, once processed, allows the analysis and visualization of internal and external features in three dimensions at micro scale resolutions.

2D image data is initially captured as projections and then processed to produce a 3D volumetric dataset of the sample. This dataset is comprised of an image stack of individual 'slices', much like in 3D printing. Each image slice has a known thickness and is therefore made up of voxels, the 3-dimensional equivalent of 2D pixels.

CT imaging is also found within the medical realm. However, the energy and exposure times in industrial and laboratory-based μ CT systems are greater and consequently unsuitable for human exposure. Medical X-ray scanning techniques commonly involve keeping the object of interest (the patient) stationary whilst the scanning equipment moves. Laboratory-based research systems instead often rotate and translate the sample which is usually much smaller.

The process of obtaining images from X-ray micro-CT is broken down into three main sequence steps and visualized in Figure 2.1.8:1.

- a) Gathering μ CT Image Data.
- b) Processing scan data, known as reconstruction, to generate an image stack.
- c) Manipulation of the image stack to allow image analysis and visualisation of the 3D imaged sample.

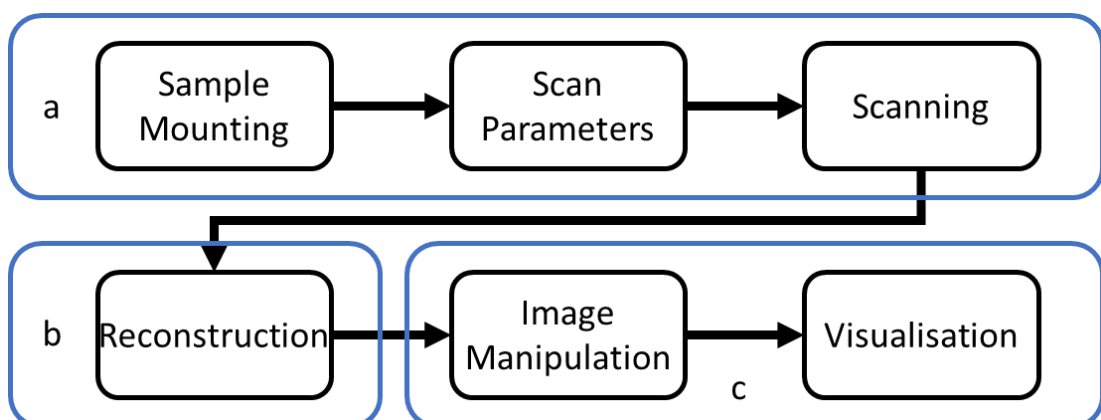


Figure 2.1.8:1 μ CT process flow chart.

^d Radiation damage may still occur to sensitive material.

2.2.1 Gathering μ CT Image Data

To begin, the specimen is mounted to a rotary stage within the machine, capable of moving in the X, Y and Z axis relative to the X-ray source. This is achieved by moving the specimen stage, the source (target), the detector or a combination depending upon machine design. In the instance of this project, the target and detector are stationary whilst the specimen stage translates in X, Y and Z and rotates about the Y-axis. (Figure 4.4.1:1)

X-ray emission energy is dictated by the operator who sets power levels in terms of kilovolts (kV) and milliamps (mA). X-ray energy is selected depending upon the nature of the sample, e.g., size, material type. Once the scan is initiated X-rays are emitted in a controlled manner from the target via a, commonly, tungsten filament, penetrate the specimen and terminate at the detector. Some X-rays are absorbed or redirected by the specimen, known as attenuation. The extent of attenuation is dictated by the material density and the size (thickness). Higher density and greater thickness lead to more attenuation, thus requiring higher X-ray energies.

X-rays leave the target and travel to the detector in a cone-shaped beam, causing intensity to vary with distance from the target. Magnification of the specimen is therefore controlled by moving the stage closer to or further from the target (Z-axis). This affects resolution, where the smallest voxel sizes (i.e., highest resolution) are collected nearest the X-ray source where intensity is highest.

The detector consists of a scintillator, a device capable of converting the energy of an impinging photon into luminescent flashes. The detector scintillates when impacted by the high energy X-ray photons. These light flashes are then converted into electrical signals, with X-ray intensity being related to the electrical charge, a higher intensity leading to a greater charge.

The X-rays that reach the detector create a 'shadow' of the specimen. This generates a negative image of the sample leading to a single 2D projection. A series of 2D projections of the object is captured, with the stage rotating by a small set amount between each projection to a total of 360°. Longer scan times consisting of more projections generally result in higher quality (less noisy) scans.

Before imaging of the sample begins, a background correction scan is produced. This is done with no objects in view of the detector to allow the system to calibrate a greyscale range. No object in view of the detector leads to a fully white image. Complete attenuation of X-rays

will lead to a fully black image i.e., nothing captured by the detector. Partial attenuation of X-rays by a sample will lead to a range of values in between, hence object scanning results in a greyscale image for each projection.

2.2.2 Reconstruction

Obtained scan data must be processed prior to viewing in a step known as reconstruction. This process takes the individual 2D object projections (slices) and 'reconstructs' the full 3D volume by piecing together the collected projections using mathematical algorithms. Noise and artefacts can be minimized at this stage, often automatically.

2.2.3 Image Analysis

Once the full 3D volume has been reconstructed the associated files can be imported into CT image manipulation software. It is at this stage that the full object volume can be analysed visually and quantitatively or manipulated to develop images suitable for further analysis.

There are no set requirements to produce a useable image. Requirements for the final images are dependent upon project requests and user discretion. Depending on the software used, there are many hundreds of options to alter the image in terms of quality and positioning. Ultimately, the goal is to have a clear 3D model of the specimen and any regions of interest for interpretation. The model can be 'moved through' from any direction to see exactly the internal structure and features.

3 Literature Review

This review will firstly summarize AV Optics' work regarding the integration of optical fibre technology and additive manufacturing. Not all aspects are pertinent to this project, but it displays the wide possibility of combinations of the two technologies.

Secondly, an outline and description of some of the current academic literature revolving around the integration of fibres and fibre optics into AM structures.

The purpose of the review is to establish an understanding of existing relevant research, with which to develop a suitable pathway for the continuation of study.

3.1 ECHOES by AV Optics Ltd

The ECHOES (Embedded Channels for Optically Enhanced Structures) report [31] outlines research and technology development by AV Optics Ltd. Focus on the following 4 key aspects of optical fibre integration with relation to additive manufacturing have been investigated and, in some instances, prototyped and tested:

- a. Design, printing, and testing of 3D printed optical waveguides.
- b. 2-dimensional embedding of optical fibres within a 3D printed structure using FDM.
- c. Cavities and pathways within an FDM 3D printed component for post-print fibre insertion.
- d. Development and testing of 3D printed optical connectors for termination and connection purposes.

3.1.1 Printed Optical Waveguides

The feasibility of AM optical waveguides was initially tested using FDM. A series of hollow waveguides with varying diameters were designed and produced using a transparent material. The waveguides were then planned to be filled with a transparent epoxy resin. Due to the nature of FDM technology laminations between layers were visible, leading to sub-optimal optical properties of the waveguide and core-cladding interface. Attempts were made to resolve this via solvent smoothing techniques but were found to be inadequate. Due to the multiple shortcomings, it was decided that the FDM technique in its current form is not suitable for the fabrication of optical waveguides.

A commercial 3D printing company with access to multiple transparent materials and high-resolution SLA printers was used to produce the next iteration of test specimens. An arch-

shaped structure was designed (Figure 3.1.1:1), containing two types of waveguides: one consisting of simple holes to be filled with a resin and the second with a solid printed core and air cladding. Total encasement in air cladding is not possible, thus support struts were included in the design to support the core. One of the resin-filled guides also included a 1 to 2 channel Y-shaped splitter to investigate optical splitting and coupling within a printed waveguide.



Figure 3.1.1:1 SLA printed waveguide test structure. The internal Y structure was included to investigate coupling [31].

Initial testing of the air-clad guides demonstrated significant losses due to the mandatory inclusion of support struts produced from the same materials as the waveguide core. The remaining channels were filled with a substance with a higher refractive index than the bulk material. An epoxy resin and oil with a similar refractive index were selected. Testing showed potential for the epoxy waveguides but demonstrated that the oil was not a suitable medium. On further analysis of the cured epoxy channels, it was seen to contain many small bubbles, possibly caused by the shrinkage of the epoxy when cured and potential gasses trapped within the liquid resin. These voids cause light scattering within the waveguide and reduce transmission efficiency. Losses of 40dB were estimated for both types of waveguides.

A second test specimen (Figure 3.1.1:2), consisting of 6 waveguides, was commercially printed with improvements learnt from the first design. 3 of the waveguides were filled with epoxy, with extensions of the waveguides to act as reservoirs as the curing resin shrank. Before and after resin injection the fluid mix was held in a vacuum to degas the mixture, this proved successful in preventing most bubbles from forming with only two visible bubbles

forming in the largest core. The extensions were cut off once the resin had fully cured to leave a smooth and flat edge. The remaining waveguides were once again air clad with only 3 support struts to hold the printed core in place.

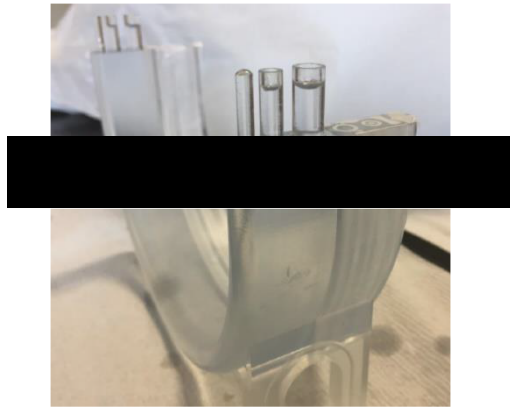


Figure 3.1.1:2 The second iteration of an SLA printed waveguide [31].

Testing of white light transmission showed a slight colour shift in both waveguide types. The epoxy filled guides demonstrated a slight blue shift with the air-clad guides showing a slight green shift, caused by the difference in absorption of the different plastic cores. Measured losses in each core showed the larger waveguides to have lower losses and that the air-clad waveguides were more effective than the epoxy filled guides by a small proportion.

Other factors impacting efficiency are also stated, such as contamination of the air cladding, the longevity of the epoxy-filled core and the inherent layer problem associated with additive manufacturing.

3.1.2 Fibre Embedding in Additive Manufacturing

Equipment and time-related constraints prevented the physical testing of fibre embedding techniques. However, an outline of the potential required fibre management was given if the embedded fibre was required to traverse between Z layers. Figure 3.1.2:1 shows the print head (in green) laying material in the FDM process. As the print head moves in the direction of the arrow, the fibre (red) must be held taught and clear of the nozzle and newly deposited material. As the print head returns in the opposite direction the fibre is angled 180 degrees so that the new material line, along with the previous one, encapsulates the fibre and allowing it to move up through the Z layers.

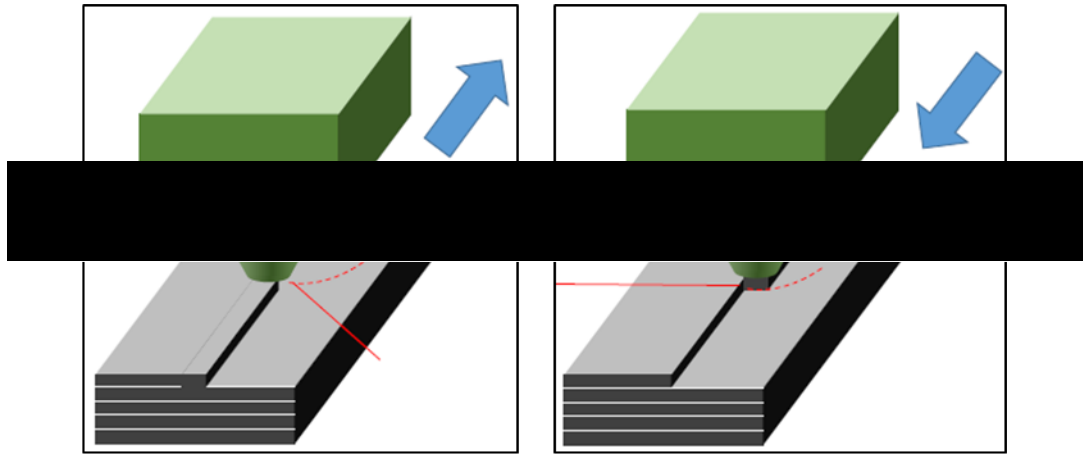


Figure 3.1.2:1 Concept showing fibre the management(red) that would be required when embedding an optical fibre into an FDM print [31].

3.1.3 Guideways for post-print fibre insertion

The development of a right-angled bracket was used to demonstrate the ability of an FDM printer to produce a component with internal cavities (Figure 3.1.3:1). These cavities act as pathways for internal fibre routing after the part has been fabricated. Whilst the post-insertion of fibres may be easier than during printing, consideration must be given to pathway design to prevent fibres from getting caught within tight radius corners or on sharp features. Limitations are also imposed on the complexity of the fibre routing path, such as the number of permissible path corners and avoiding structural weakening. Routing fibres in this manner only act as a simple passthrough and do not allow FBGs to monitor the components structural health. Post insertion of the fibres also leads to added manufacturing steps, possibly increasing production time and cost. The report also outlined the inclusion of input ports and vents along the cavity route to allow injection of a resin material to fix fibres in place.



Figure 3.1.3:1 FDM printed bracket demonstrating integrated guides for fibres [31].

3.1.4 Incorporated Optical Connectors

Fibres integrated within a 3D printed structure will have to be accessed to allow the input and output of the light transmission. Much like electrical cables, this can be achieved with connectors.

Two major considerations revolving around optical fibre connectors are optical alignment, both fibre with the connector and the connector to an adjacent connector, and the optical transmission efficiency. Alignment issues were suggested to be solved in two manners: one using magnets to mechanically align the end of the fibre to the next connector, the second using a threaded insert and gradient-index (GRIN) lens (Figure 3.1.4:1). A GRIN lens is a type of lens created by a gradient in the refractive index of the material to create a lens with a flat surface allowing the fibre tip to butt against it.

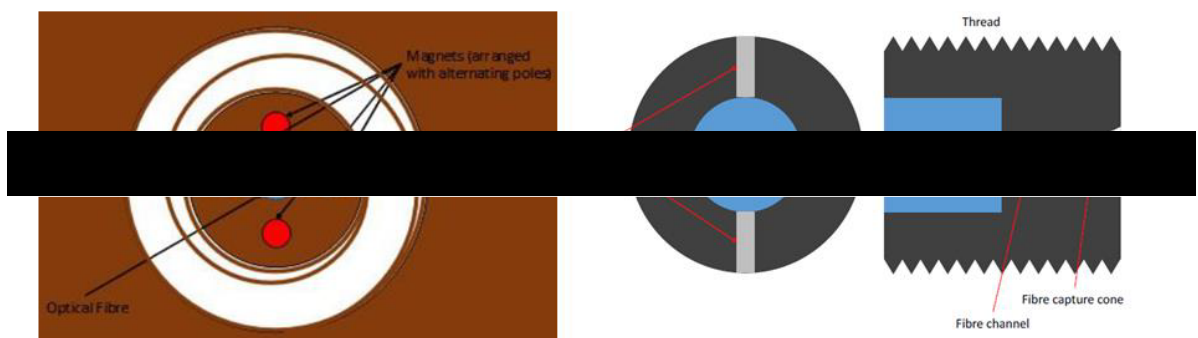


Figure 3.1.4:1 Two concepts for integrated optical connectors within a 3D printed structure. The first (left) using magnets with alternating poles facing outward to mechanically align the matching external connector. The second (right) incorporates a GRIN lens mounted in a threaded housing which can be screwed into a printed structure [31].

Magnets arranged with alternating poles in a circular manner around the optical fibre would be able to mechanically locate the fibre against an adjacent connector with the same arrangement. The end of the fibre and magnets would be contained in a floating housing to allow a small range of movement letting the magnets automatically locate the fibre tip. This solution would require the development of a robust structure capable of the required movement whilst being able to withstand multiple connects and disconnects. The use of magnets also leads to further required manufacturing steps.

The insert solution consists of a threaded component housing a GRIN lens, which would be inserted into a receptacle within the printed structure at the centre of which the fibre is located. A 'fibre capture cone' would guide the fibre into a channel causing the fibre tip to butt up against the GRIN lens. This method shows a form of fibre termination at the printed structure interface; however, it does not suggest a system to which an external device could be coupled.

A connector prototype was designed and printed for use with plastic optical fibre (POF) commonly found in consumer applications. The connector comes in two halves employing a friction push fit to house each of the POFs. One connector half is considered male and the other female, utilizing a hole and dowel system to allow alignment and connection of the two connector halves, thus creating a butt connection between each segment of POF. A teardrop-shaped hole was used to create a tolerance for fibre insertion and to ensure friction did not prevent the fibre tip from reaching the end of the connector. Upon testing a measured loss of 2.02 dB was recorded and it was noted that glass fibre cores are typically smaller diameter, leading to possible greater misalignment and losses due to the accuracy levels of the FDM technique employed here.



Figure 3.1.4:2 Printed connectors with friction fit POF. One half is male, the other female enabling a butt connection of the two halves to enable optical pass through [31].

A second prototype connector was developed based on the GRIN lens insert and POF connector outlined above. A fibre terminator design was commercially 3D printed in aluminium to house a GRIN lens and the tip of a 600 μm Hard Clad Silica optical fibre. The insert was then push fit into a printed plastic housing (similar to the one shown in Figure 3.1.4:2) using 3 'guide fins' to correctly locate and orientate the connector with the GRIN lens, collimating light supplied by the fibre resulting in the final expanding beam connector. Testing of this connector recorded losses of 6.75 dB when compared to a homogenous optical fibre of the same length. Losses were found to be highest at the fibre tip and GRIN lens interface which was improved using transparent adhesive, leading to lower loss values of 5.18 dB. This connector type was seen to be less sensitive to optical misalignment between the two halves when compared to previous tests.

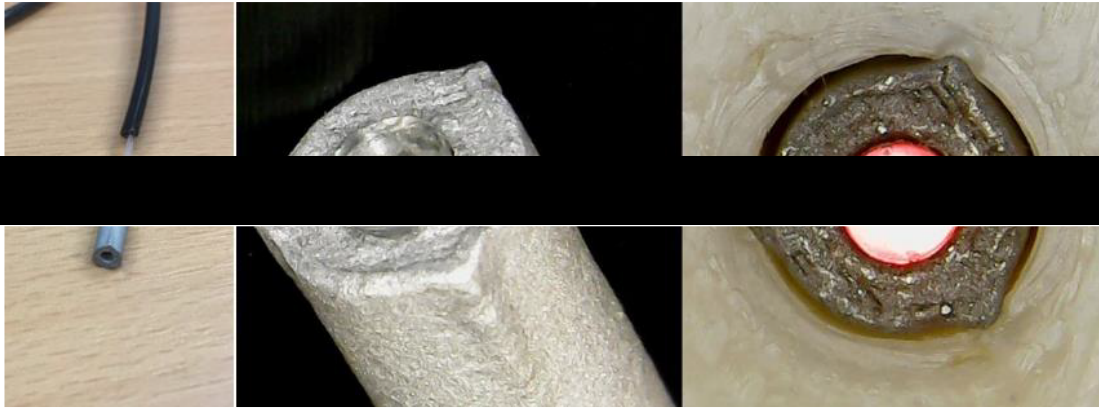


Figure 3.1.4:3 POF inserted into printed aluminium housing (Left). Close up shows GRIN lens and guide fins of housing (Middle). Assembly fit into the printed connector housing and demonstration of optical function (Right) [31].

3.1.5 ECHOES Research Summary

- AV Optics have shown the plausibility of 3D printed optical waveguides using the FDM and SLA processes. The low layer resolution of currently available FDM machines has proven it to be an unsuitable technology for this purpose. Greater success was found using the SLA process but with several challenges still to be overcome.
- Printed guide paths for post-fabrication fibre insertion were found to be a success but does not offer full incorporation into the structure. Extra fibre handling steps post manufacture is also required.
- Whilst the experimentation of automated fibre embedding was not carried out, a suggestion for the required fibre handling was proposed for 3-dimensional incorporation into an FDM produced component.
- Multiple solutions to incorporated optical connectors were suggested and some tested with varying success. Future work is required to reduce optical loss across the prototyped connectors and to develop a fully integrated solution.
- Mechanical properties or impacts of any of the presented concepts were not explored.

3.2 Academic Literature

The following sections of the review focus on academic research regarding fibre integration with 3D printed structures and components. Different methods of AM for fibre integration have been investigated, including UAM [32] and PBF [33] methods, however, this review will focus on FDM.

3.2.1 Mechanical Properties of FDM Structures Printed in PLA Without Fibre

To understand the impacts of embedded fibre, a reference of mechanical properties for FDM printed structures must first be established. Mechanical properties of printed PLA structures have been well investigated and documented. However, the relatively young age of the technology and lack of standardization for both testing and manufacturing gives rise to varying results. The large number of potential variables also lends to difficulty in a direct comparison of research results, particularly when not all print parameters are stated.

Letcher et al. [34] investigated the material properties of PLA specimens produced on an “entry-level” 3D printer. In today’s consumer-orientated 3D printer market, entry-level printers can be found for considerably less than the MakerBot Replicator 2X used, and with greater feature sets. The research focused on the impact of raster angles at 0, 45 and 90 degrees, on tensile, flexural and fatigue properties. It was concluded that a 45° raster angle was superior in tensile testing and a 0° angle for 3-point flexural testing was strongest. Testing of the feedstock PLA filament showed similar tensile properties to the printed samples. However, the brand of filament used was not specified, nor were experimental results compared to those stated by the material manufacturer. The layer height used to produce specimens was also not identified, which affects mechanical properties [35].

Kim et al. [36] also examined the raster orientation on tensile properties, but rather than alter slicer parameters, the angle of the model on the print bed was adjusted to achieve a similar goal. However, this leads to raster angles of $\pm 45^\circ$ and 0, 90 degrees alternating each layer, opposed to the same raster direction throughout. It was discovered that a raster angle of $\pm 45^\circ$ led to the highest tensile strength, although values were significantly lower than other findings [34].

Patel et al. and Rismalia et al. [37,38] examined the effects of infill patterns on tensile properties. Significantly different results are presented by the two papers when considering similar infill patterns and infill densities, with Rismalia et al. [38] stating a UTS value for 25% grid infill of 29.7 MPa, compared to 19.1 MPa for 40% grid infill tested by Patel et al. [37].

Jaya Christiyani et al. and Travieso-Rodriguez et al. [39,40] investigated the flexural properties of PLA. Jaya Christiyani et al. [39] varied the layer height and maintained the infill density at 40% but did not state the pattern. Print speed was also varied between 38 and 52 mm/s, conservative values for modern printers. It was found that the lowest layer height of 0.2mm and the slower printing speed led to the highest flexural strength of 68 MPa. Travieso-Rodriguez et al. [40] employed a Design of Experiments to run a more conclusive evaluation of the effect of different printing parameters, including layer height, infill density, infill pattern and print speed. The authors concluded, similarly, that the lowest tested layer height of 0.1mm and a slower printing speed of 20mm/s was preferred to maximise Young's Modulus, yield strength and the maximum tensile force. Infill density and pattern played a less significant role than print speed, extrusion width and layer height on the same properties.

Table 3.2.1-1 displays a summary of presented results from some of the outlined papers. No two tabulated specimen print parameters are equal. Further parameters such as the number of walls, material manufacturer, print hardware, cooling fan speed or print temperature have not been included. In some instances, these parameters are not stated. This highlights the need to conduct testing of mechanical properties specific to this project to produce results capable of direct comparison.

Table 3.2.1-1 Summary of some of the previous research findings. (- = not tested, x = not stated.)

Ref.	Layer height	Infill density (%)	Raster orientation or Infill Pattern	Print speed (mm/s)	UTS (MPa)	Tensile Modulus (MPa)	Flexural Strength (MPa)	Flexural Modulus (MPa)
[34]	x	100% infill	0	100	58.45	3330	102.203	3187
	x		45		64.03	3600	69.649	2985
	x		90		54.01	3490	86.136	3000
	Pure filament				59.518 (at 200mm/min strain rate)	1868	-	-
[37]	0.3	40%	Lines	x	20.6	-	-	-
			Grid	x	19.1	-	-	-
			Concentric	x	18.8	-	-	-
		60%	Lines	x	26.1	-	-	-
			Grid	x	24.6	-	-	-
			Concentric	x	24.0	-	-	-
[38]	0.1	25%	Grid	50	29.7	2760	-	-
			Tri-hexagonal		27.8	2610	-	-
			Concentric		32.6	3140	-	-
		50%	Grid		31.5	2800	-	-
			Tri-hexagonal		30.6	2720	-	-
			Concentric		44.3	3270	-	-
		75%	Grid		35.4	3280	-	-
			Tri-hexagonal		37.3	3010	-	-
			Concentric		42.2	3897	-	-
			-		-	-	-	-
[35]	0.1	100%	±45 (rectilinear)	x	-	-	43.6	1190
	0.2			x	-	-	44.1	1180
	0.3			x	-	-	43.8	2130
	0.4			x	-	-	43.9	1890
	0.5			x	-	-	59.6	1540
[40]	0.1	25	Rectilinear	20	-	-	64.2	2360
	0.2	75	Linear		-	-	80.8	2710
	0.3	50	Honeycomb		-	-	64.1	2780
	0.1	50	Honeycomb	40	-	-	83.7	3340
	0.2	25	Rectilinear		-	-	72.3	2410
	0.3	75	Linear		-	-	35.7	1440
	0.1	75	Linear	30	-	-	93.1	3230
	0.2	50	Honeycomb		-	-	86.4	2850
	0.3	25	Rectilinear		-	-	60.4	1900

3.2.2 Reinforcing Fibre Integration Process in FDM Additive Manufacturing

Fibre integration is frequently used in traditionally manufactured composite construction, both as discontinuous (short) fibres and long, continuous fibres to form Fibre Reinforced Polymer Composites (FRPCs). Glass fibre spraying is an example of short fibre composite manufacture while automated tape laying can be considered an example of continuous fibre use. Discontinuous and continuous reinforcing fibres have been shown to be successfully integrated into 3D printed structures to the extent of commercial systems being available [41,42].

Fibre reinforcement in additive manufacturing garners high interest due to the combination of advantages associated with AM and the mitigation or elimination of disadvantages associated with traditional FRPC construction. One example is the exclusion of mould requirements for individual components in some forms of FRPC construction, another would be the ability to adjust fibre fraction and location on the fly.

The primary desired outcome of embedded optical fibres is not to act as fibre reinforcement, but for data transmission and sensing duties. However, due to prevalent research and the use of reinforcing fibres in AM, the aspect of the fibre embedding process has already been investigated and presented.

3.2.2.1 Deposition and Integration

The methods of fibre integration can differ depending on factors such as the type of fibre, length of the fibre, fibre diameter, fibre volume and if the fibre is continuous or discontinuous. Optical fibres would be considered long and continuous, hence, only continuous reinforcing fibres are investigated.

Fibre deposition and method of encapsulation are critical to the impact the fibre can have on the structure. Baumann et al. [43] shows 3 different methods of fibre integration in an FDM based system (Figure 3.2.2:1) and investigates new methods of fibre integration.

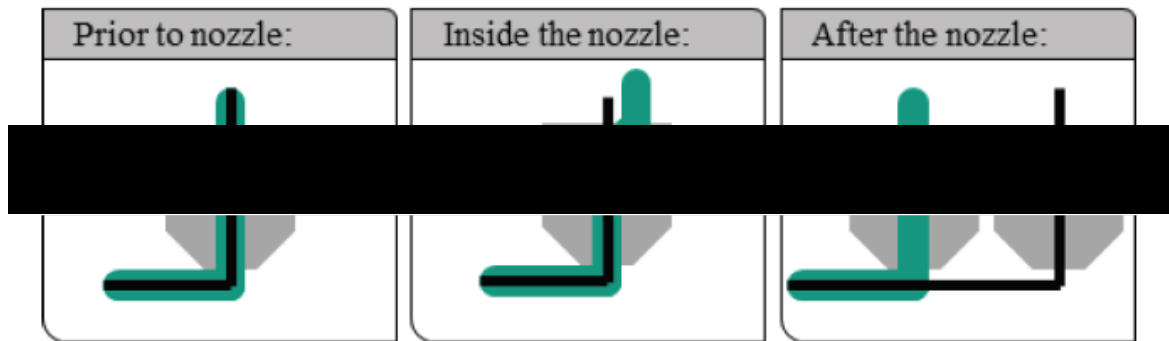


Figure 3.2.2:1 3 potential ways to integrate fibre into an FDM printer. Prior to nozzle: the fibre is already integrated with the bulk material and acts as the feedstock as in standard FDM printing. Inside the nozzle: fibre and the matrix material are fed separately into the hot end where they are heated and combined. After the nozzle: two separate nozzles, one handles the matrix polymer, the other the fibre. The fibre material is laid by the first nozzle, the second coats it with the matrix material. [43]

- a) Prior to the nozzle: Fibre can be pre-loaded into the filament and deposited in the same manner as the matrix material. This implies 1 of 3 scenarios; either the print structure is produced entirely from the fibre reinforced material, that a separate deposition nozzle exists to lay the fibre encapsulating material or that filament changes occur to allow selective deposition of fibre or bulk material.
- b) Inside the nozzle: Fibre and matrix material are fed separately into the hot end where they are heated and combined. This can enable the addition of fibre at any stage in the printing process via the same nozzle as the bulk material. Requires a fibre cutting system.
- c) After the nozzle: 2 deposition nozzles work together, one to lay the fibre, the other to lay the encapsulating material. These can be mounted together and operate in tandem, or on separate motion systems as required. Fibre material can be selectively laid as required; a cutting system is required.

Ultimately the method of deposition is not the focus of this project but must be considered to produce robust samples which can then be tested and analysed in an equal manner.

3.2.3 Optical Fibre Integration in FDM

Two aspects of optical fibre integration are of particular interest: the methods used to embed the fibre during the AM process and the mechanical effects these fibres have.

3.2.3.1 Embedding Procedures

As previously discussed, the method of integration is not the project focus. However, prior research may show suitable methods for use with optical fibres.

Optical fibres, as opposed to continuous structural fibres, must be integrated within the printed component in a way that allows the fibre to exit the structure or enable interrogation of the fibre, such as concepts shown in the ECHOES report [31] (Section 3.1.4). Thus, optical fibres cannot be deposited in the same automated manner seen with reinforcing fibres where cutting of the fibre is required.

Archenti et al., Kantaros et al., Zelený et al., Zubel et al., Kousiatza et al., Pereira de Lima, Economidou et al., Leal-Junior et al. and Fauver et al. [44–52]. all achieved integration by pausing the printing process then manually laying and securing the fibre before resuming printing. Some opted to include grooves within the structure to align the fibre. The majority used separate structures to the test specimen to secure either end of the fibre, maintain alignment and apply tension. The common requirement being an interruption of the print process and manual intervention to lay the fibre.

Automation of optical fibre laying in additive manufacturing is another significant topic worthy of focused research. A concept is briefly described in the ECHOES report [31] (Section 3.1.2) but is beyond the scope of this project.

3.2.3.2 Mechanical Influence

The layer-by-layer nature of AM enables the integration of FBG sensors within the structure being manufactured to monitor internal thermal and strain properties during the manufacturing process itself. Kantaros et al. [45] embedded an FBG sensor into the midplane of an ABS specimen to measure residual strains caused by material solidification. The effects of layer thickness and deposition orientation were specifically investigated. Kousiatza et al. [48] display similar research with an embedded FBG in ABS to study residual strains and temperature profiles of the specimen. The printing parameters were maintained equal whilst the FBG sensors were integrated into different layers and either longitudinally or transversely to the specimen. Economidou et al. [50] also embed FBG sensors into ABS specimens to measure residual strain during fabrication with consideration of raster orientation. The suitability of FBG sensors for use in tensile testing was also investigated.

Critically, each of the mentioned articles does not consider the impact the embedded fibre may have on the values being measured.

Research during the project time frame resulted in the failure to discover clear information pertaining to the mechanical effects an embedded optical fibre may have on an FDM printed structure. This is significant in itself and may be due to one of, or multiple considered reasons:

a) There is no currently published work:

Research into the mechanical effects of an embedded optical fibre may currently be in progress or has simply not been carried out.

b) The mechanical impacts of an embedded optical fibre may be considered insignificant in relation to the benefits derived from an embedded sensor. Fauver et al. [52] states in the abstract “chosen because they can be embedded with minimal effect on the desired structure”. However, this statement is not explored further.

c) Research on the matter may have been conducted within an industrial setting and is unavailable.

A deeper investigation would be required to uncover specific research regarding the mechanical effects of embedded optical fibres in an FDM structure or as to why it is not discoverable.

3.3 Academic Research Summary

- There is wide interest in embedded fibres using many of the methods of additive manufacture.
- Existing literature shows that mechanical properties of 3D printed PLA widely varies, even with similar print parameters.
- A significant volume of research regarding reinforcing fibres in FDM exists, to the extent that commercial systems are available to automate the process. However, these systems are not suitable for use with optical fibres as they require cutting of the fibre or producing the entire structure with contained fibre.
- Different solutions for fibre embedding have been proposed. Similarly to the commercial solutions, they either require the whole component to include fibre or the fibre must be cut. Not suitable for fibre optics.
- Past work on using optical fibres use manual methods of integration by pausing the printing operation to lay the fibre.
- Embedded FBGs have been successfully used to measure internal strains and temperatures during sample fabrication, post-fabrication and to an extent during mechanical testing. The mechanical impact of the embedded fibre is not considered.
- Focussed research specifically on the mechanical impacts of an embedded optical fibre in FDM appears to be lacking.

3.4 Literature Review Conclusion

- AV Optics have demonstrated the breadth of opportunities for the integration of fibre optic technologies with additive manufacturing. Some have shown greater promise than others.
- The large amount of research on mechanical properties of FDM printed PLA demonstrates the need for further testing. Results based on the hardware, software, and material available for this project must be used to produce results capable of direct comparison with fibre embedded samples.
- Commercial FDM fibre systems are unsuitable for the requirements of optical fibres. A different method of fibre embedding must be used. Previous work indicates manual fibre embedding to be the best option currently.
- There appears to be no research specifically on the mechanical impacts of embedded fibre optics in an FMD 3D printed structure.

4 Methodology

The following chapter details the forms of testing selected, the design parameters of samples that were tested, how samples were manufactured and finally the methods and equipment used for each type of testing.

Due to little or no research currently existing on the mechanical impacts of embedded fibre optics in FDM, a range of testing and printing parameters were selected to give an initial broad insight into the topic.

FDM was selected as the method of AM for various reasons, the primary being the ease of process modification. For instance, FDM does not require atmospheric control or powder handling as PBF methods do. The process can be simply paused and restarted to allow user interaction at any stage of the print. Other factors resulting in the selection of FDM included hardware and material availability, user process familiarity, costs, and the numerous available slicing parameters.

Two standard forms of mechanical testing were chosen: tensile and flexural. Economidou et al. [50] investigated the suitability of embedded FBGs in tensile specimens for internal sensing purposes. They were found to be successful until the point of failure at the fibre-matrix interface. Once the bond between the fibre and structure was broken, measurements recorded by the fibre were no longer suitable. Therefore, fibre pull-out testing will also be conducted to determine how printing parameters impacted the bonding strength of the fibre with the matrix material.

Micro-CT imaging was used to visualise internal structures and see the effects of embedded optical fibre. Corresponding BS/ISO standard documents were used to guide tensile and flexural mechanical testing. No standard was available for retention testing of a fibre optic embedded within an FDM 3D printed structure.

4.1 Design Parameters

4.1.1 Plain Sample Types

To understand the impacts of embedded optical fibre, an array of plain samples omitting the fibre were first required. As shown in the Literature Review, nuances in the hardware, material and environment can lead to considerably different results, even for similar printing parameters.

Without explicit application, nor previous literature, any printing variable is open to testing. Two commonly adjusted variables were selected for plain samples: infill pattern and infill density. These parameters were selected as they are easily modified to change the mechanical characteristics of the printed part and are both visually distinct. Many other print variables are available, such as nozzle print temperature and layer height, but infill density and pattern were chosen due to being easily identifiable in micro-CT imaging.

Infill percentages were chosen to investigate low, medium, high, and maximum density specimens. Values were chosen ranging from 20% to 100% and infill patterns were selected from the available options within the slicer. Table 4.1.1-1 lists the selected infill percentages and patterns whilst Figure 4.1.1:1 shows them visually.

Table 4.1.1-1 Infill parameters for plain samples.

Density Percentage	Infill Pattern
20	Cubic
	Grid
	Triangles
40	Cubic
	Grid
	Triangles
80	Cubic
	Grid
	Triangles
	Concentric
100	Lines

Cubic – Cubic infill is a 3D type infill. Selected to explore if performance would be improved over 2D options.

Grid – A 2D simple infill, based on repeating squares.

Triangles – Similar to grid infill, based on triangular tessellation. A, perhaps, instinctively stronger option.

Concentric – Concentric infill creates raster lines parallel to the perimeters of the component. This was selected to investigate the impact of material deposition in the direction of tensile loading.

Lines - 100% infill was selected to showcase a theoretically fully dense component. (Full density achievement will be investigated).

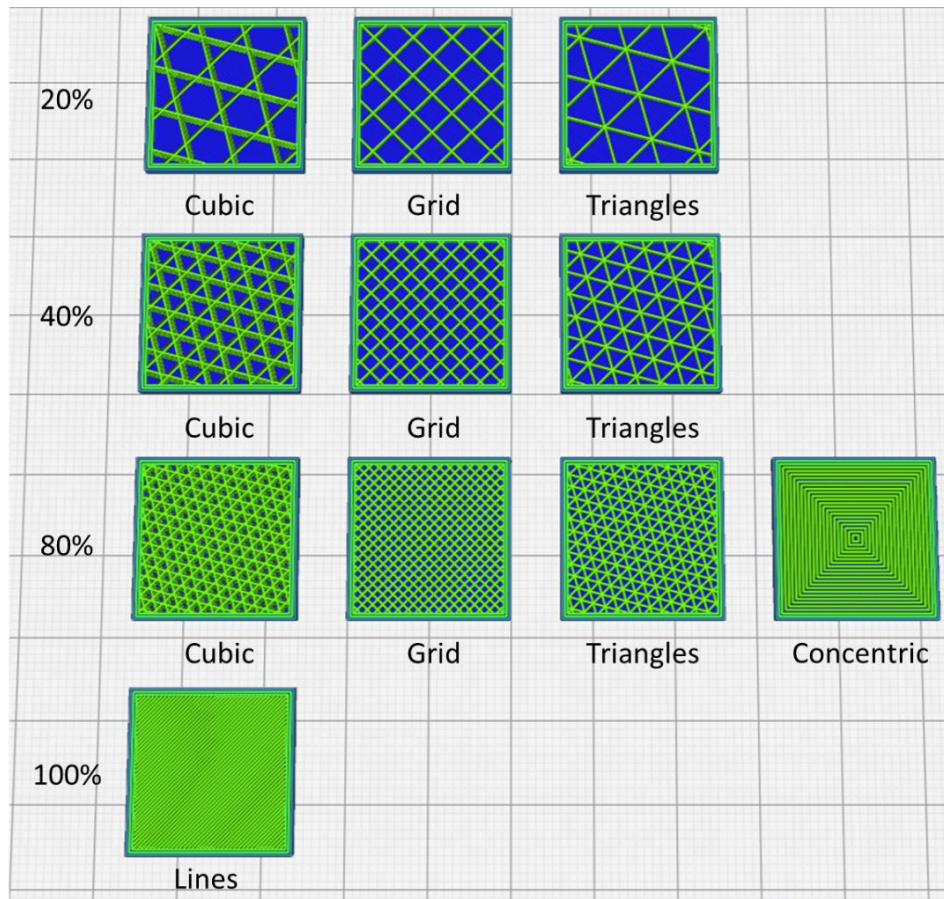


Figure 4.1.1:1 Infill patterns and varying densities are shown in slicer software. Green represents infill material and blue shows shell material. The top shell layers were removed to show the infill.

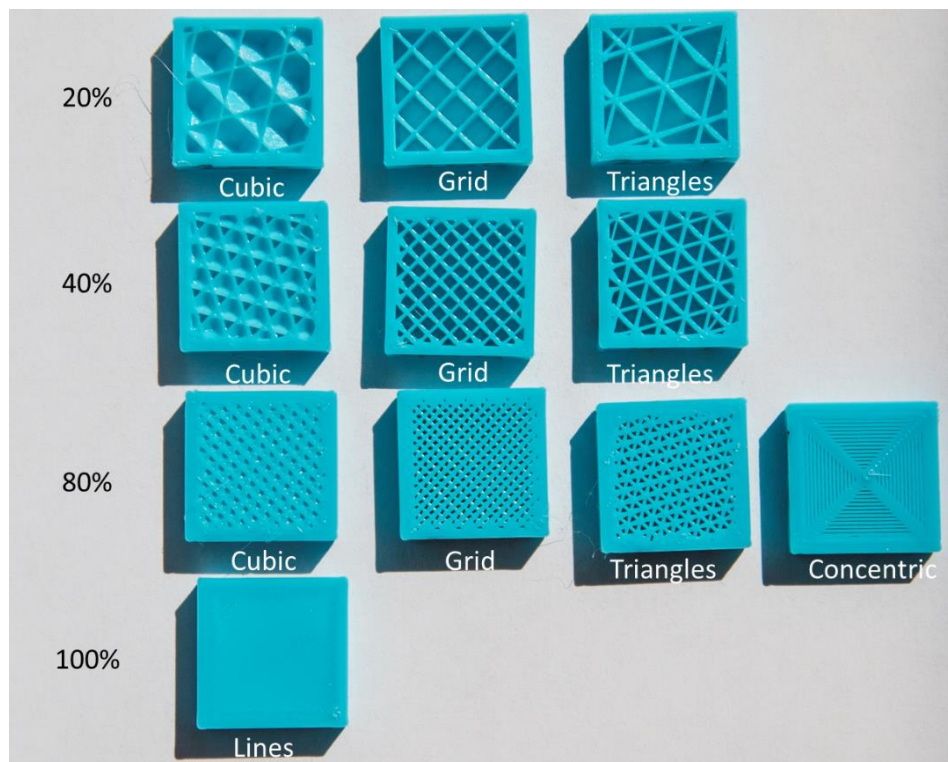


Figure 4.1.1:2 Printed infill examples. The top shell layers are removed to expose the infill. The bottom shell layers are also omitted to allow greater contrast and hence display of the infill.

4.1.2 Standard Fibre Infill

To simplify fibre sample fabrication a standard set of infill parameters were chosen for samples that do not require changes to infill density or pattern. Preliminary testing indicated the triangular pattern at 40% infill density struck a balance between fibre support (to prevent possible drooping) and production time. This has been abbreviated to 'SFI' for simplicity.

4.1.3 Fibre Sample Types

Fibre inclusive samples have intrinsically more potential print parameters (e.g., which layer to incorporate fibre, type of fibre, direction of fibre) which may alter both overall print quality and the effectiveness of the fibre embedding. The aim is to investigate the impact of embedded fibres when compared to a plain sample and to consider optimising the print process for optical fibre embedding.

To directly compare samples with and without fibre 2 types of infill parameters were selected. 40% triangle infill was chosen as a basic infill type and 80% concentric infill was chosen to investigate print raster lines being laid coaxially to the embedded fibre.

The remaining sample types focused on the quality of fibre embedding by altering various print and fibre parameters. The parameters to vary were selected during discussions with AV Optics.

- A. Standard fibre sample – No alteration to print parameters. For direct comparison with plain samples.
- B. Layers either side of fibre – SFI was used for the bulk of the structure. Extra material layers at 100% infill were added before and after fibre placement. This may aid in the installation by minimising drooping, improving encapsulation and fibre-matrix bonding whilst adding only minimal additional weight.
- C. Direction of raster lines over fibre – The direction of infill material deposition was changed from the default $\pm 45^\circ$ to 0° (parallel to fibre) and 90° (orthogonal to fibre) to investigate the impact on fibre-matrix bonding and hence the quality of embedding. A 100% infill was selected for the entire sample.
- D. Fibre direction – The fibre direction within the specimen was rotated between 0° , 45° and 90° . The infill parameters were set to SFI allowing direct comparison with plain samples.

E. Fibre buffer material – Polyimide buffer fibre was used in the majority of fibre samples. Acrylate and high-temp acrylate buffers were also embedded in SFI samples to see if an improved bond can be created with the PLA matrix.

Table 4.1.3-1 below shows a matrix of the chosen design variables and the testing methods applied to each type.

Table 4.1.3-1 Parameters and testing methods for fibre samples. Unique samples have been assigned a reference depending on their variable. The ‘Parameters’ column highlights the infill and specific details. Dots in the ‘Applicable Testing Methods’ column show which testing is applied to that specimen type. Highlighted boxes with different specimen references show those with equal parameters.

Sample		Parameters		Applicable Testing Methods			
Reference	Variable	Infill	Details	μCT	Tensile	Flexural	Pull-Out
A1	Equivalent Fibre Sample	SFI	-	•	•	•	•
A2		80% Concentric	-	•	•	•	•
B1	Layers either side of the fibre	SFI with 100% extra layers	1 layer	•	•	•	•
B2			2 layers	•	•	•	•
B3			5 layers	•	•	•	•
C1	Direction of raster lines over fibre	100%	0°	•			•
C2			45° alternating	•			•
C3			90°	•			•
D1	Fibre Direction	SFI	0°		A1	A1	
D2			45°		•	•	
D3			90°		•	•	
E1	Fibre buffer material	100%	Polyimide	C2			C2
E2			Acrylate	•			•
E3			HT Acrylate	•			•

Each sample has an associated reference for quick identification. The ‘Sample’ column describes the variable of interest. The ‘Infill’ and ‘Details’ columns provide information on the infill parameters and further sample properties. The 4 following columns indicate the methods of testing that specimen was subject to: CT imaging, tensile testing, flexural testing, and fibre pull-out. Samples with equal parameters are also noted.

4.2 Fibre Details

Optical fibre was supplied by AV Optics. Due to no specific fibre requirements, there were no constraints on the type of fibre used. Hence, AV Optics selected fibre that they commonly use and was readily available.

Table 4.1.3-1 summarises details of the types of fibre used in this project. The buffer material will be stated as a reference to the type of fibre used.

Table 4.1.3-1 Optical fibre details. The type of fibre used will be referenced via the buffer material. Appendix A – Optical Fibre Specifications shows the fibre manufacturer specification sheets.

Buffer Material	Manufacturer	Product Name/Number	Coating diameter (total outer diameter, μm)	Operating Temperature ($^{\circ}\text{C}$)
Polyimide	Fibercore	SM1250 (10.4/125)P	155 \pm 5	-55 to +300
Acrylate	Corning [®]	ClearCurve [®]	242 \pm 5	-60 to +85
High Temp Acrylate	Gore	FOA 1214	245 \pm 1	-60 to +135

Polyimide fibre was supplied as bare spooled fibre. Both acrylate and high-temperature acrylate fibres were supplied as multi-core cables. Individual fibres were extracted from the cables via mechanical methods.

4.3 Sample Fabrication

Sources of variability between samples are required to be kept to a minimum or clearly identified to enable a robust analysis and comparison. The following paragraphs outline the global parameters and test specific sample fabrication.

4.3.1 Global Parameters

Global parameters refer to the software, hardware, material, and post-processing options kept identical between all samples, both plain and fibre inclusive.

All samples were printed flat on the build platform in the XY plane. The printing orientation was kept equal for all sample sets and the fibre direction rotated where necessary.

4.3.1.1 Software

Solidworks by Dassault Systems was used to produce all CAD models to a respective BS ISO standard, outlined in the relevant sections below. No account for FDM manufacturing tolerances was applied.

CAD models were exported from Solidworks as .STL files and imported into slicing software Ultimaker Cura version 4.0.0. Updates became available during the manufacturing phase but were not installed.

Ultimaker Cura is an open-source slicer and can slice models for any printer accepting of G-code. As such there are a vast number of highly adjustable slicing parameters, each with a varying degree of effect on machine operation and final print quality. To minimize variables and to maintain regularity between different samples the default 0.2mm print profile was used to define slicing parameters. A minor profile alteration changed the number of top and bottom layers to 3, matching the number of perimeter walls.

A few key settings are highlighted below with full slicing profile details found in Appendix B – Cura 4.0.0 Fibre Printing Profile Settings.

- Layer height: 0.2 mm.
- Print temperature: 210 °C (Hot end), 60 °C (Bed).
- Print speed: 60 (infill), 40 (outer walls), 30 (initial layer), 30 (top/bottom) mm/s.

It should be noted here that infill described as 100% density was achieved by setting the slicer infill density option to 99% and using the lines infill pattern. This avoids Cura treating the infill as a bottom layer and ignoring requested settings pertaining to infill, as visualised in Figure 4.3.1:1 below^e.

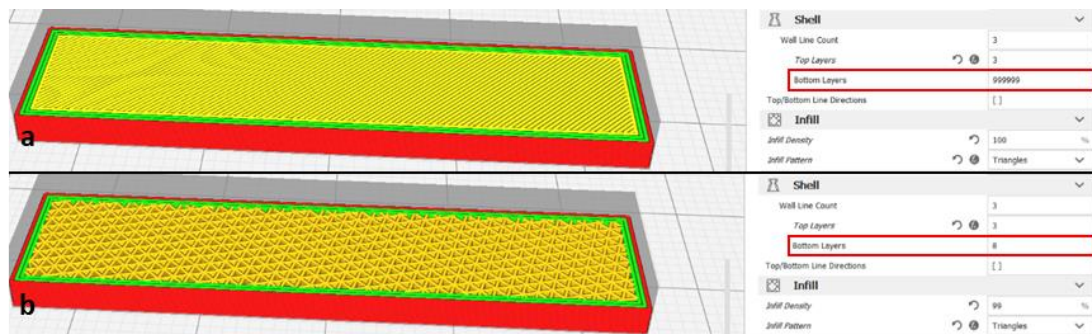


Figure 4.3.1:1 Cura infill adjustment. a) If left to default, the 'bottom layers' (red highlighted box) will be set to maximum so that every layer of the structure is considered a bottom layer when the infill density is requested as 100%. b) when the infill is requested as 99% or below the number of bottom layers is calculated using the first layer thickness, first layer height and infill density, then rounded up to an integer value.

4.3.1.2 Hardware

All samples were produced on Ultimaker 2+ systems with no hardware modifications. The build platform was glass with no extra bed adhesion material applied. Bed levelling was carried out before each print. Multiple machines were used to produce samples throughout the project allowing the fabrication stage to be completed in a timely manner.

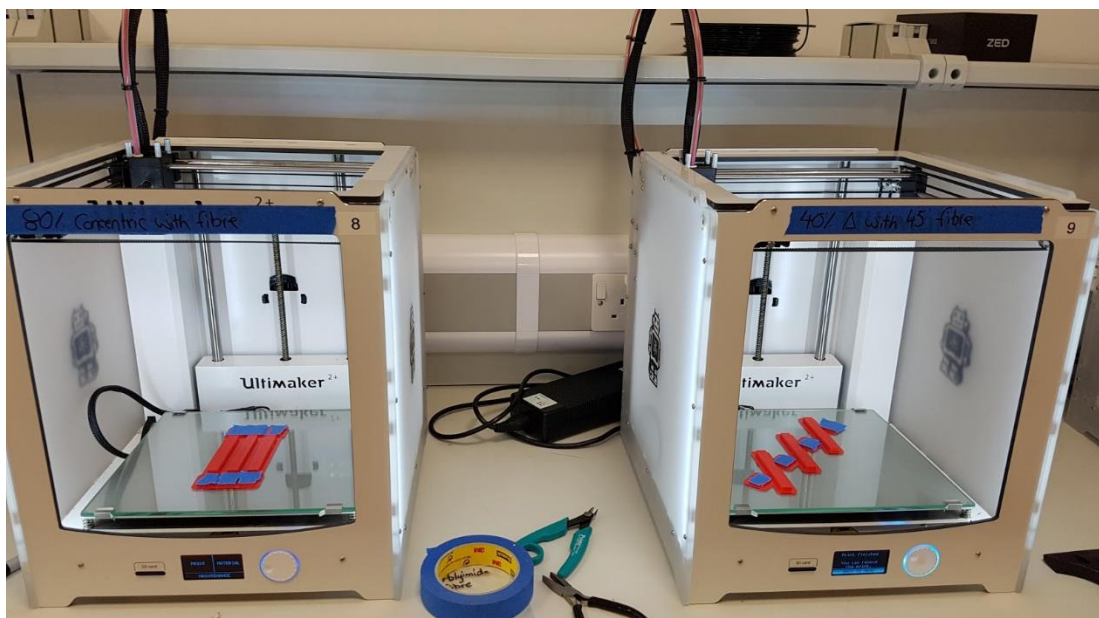


Figure 4.3.1:2 Ultimaker 2+ FDM printers with no hardware modifications. Flexural samples are shown completed on the bed.

^e It should be noted that the same can be achieved by manually setting the number of bottoms layers to 3.

4.3.1.3 Material

Project aims are to investigate the impact of embedded optical fibres regardless of the matrix material and without specific use cases, enabling free range in terms of material selection. PLA was selected as the print material for several key reasons:

- Ease of printing: PLA prints easily with little to no warping and without an enclosed build chamber. It does not produce fumes as with ABS.
- Easy to store: PLA is not hygroscopic, unlike nylon materials and does not require special storage conditions.
- Low cost and accessible: PLA is a common FDM print material and is readily available at low costs from numerous vendors. Project aims can be achieved without expenditure on more costly material.

Ultimaker 2+ systems accept 2.85mm diameter filament. PLA supplied by ICE Filaments was chosen and shown to print reliably on the Ultimaker systems. Appendix C – Filament Specification shows manufacturer details.

Preliminary testing showed significant differences in the properties of different material colours, even though the same data sheet is supplied for all colours of that material. The colour of PLA material has been shown to have a significant impact on mechanical properties [53]. A single colour, 'Romantic Red', was chosen to print all future mechanical samples. X-ray samples were printed in different colours of the same material.

Whilst storage requirements for PLA are minimal, given enough time in an unsuitable environment, such as direct sunlight or high humidity, it can begin to degrade and impact print quality. Print hardware was located in a climate-controlled room without any direct sunlight. The material was stored in the same space openly without fear of degradation over the period of the project.

4.3.1.4 Fibre Prep and Installation

Fibre lengths were prepared during the printing process for each sample set. Fibre was cut to a suitable length using side cutters and cleaned using paper towel and high percentage isopropyl alcohol to remove any debris or residue.

To allow installation, a post-processing script was applied in Cura to pause the printing process at the specimen mid-layer. Upon pausing the print, fibre was anchored to fibre blocks printed concurrently with the samples using blue painter's tape (Figure 4.3.1:3). The fibre

was held taught with pliers allowing it to be secured. Fibres were placed as centrally in the specimen as possible. Once secured printing was resumed manually.

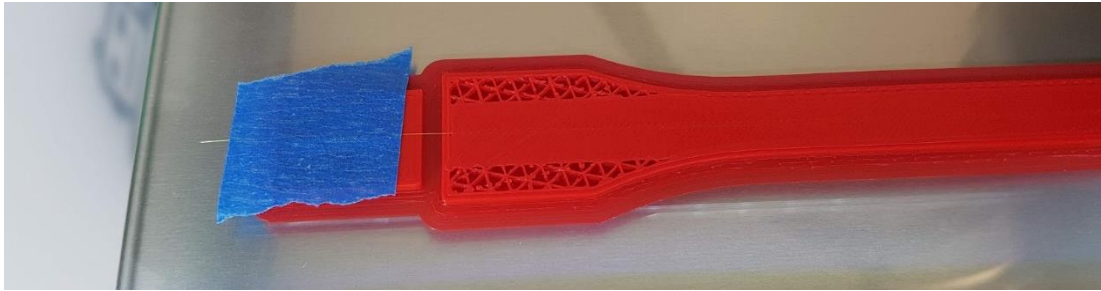


Figure 4.3.1:3 A tensile sample with affixed fibre just after print resume.

Priming blocks were printed along with samples to allow nozzle priming after the pause. During the pause, the nozzle is kept at print temperature leading to material oozing. To ensure desired material flow when overprinting the fibre, material was first deposited on the priming block upon resuming the print.

4.3.1.5 Post-processing

Upon indicated print completion, samples were removed using a razor scraper if they were not free of the glass bed. All samples were printed with a brim as per the default Cura slicer profile. This was removed by hand to the best possible degree. Tools were avoided to prevent possible sample damage. In some instances, it was not possible to remove the entirety of the brim material. This should have no impact on mechanical performance but was avoided when sample measurement was required.

Excessive fibre protruding from tensile and flexural samples was reduced to approximately 20 mm using flush cutters to avoid being snagged and causing premature fibre displacement. Fibre pull-out samples maintained the protruding fibre suitable for gripping during testing.

4.3.1.6 X-ray Samples

Samples of dimensions 10 x 10 x 20 mm were chosen for micro-CT scanning. Sample dimensions were not critical, but a balance between size to obtain a high scan resolution and speed of manufacture was necessary. Smaller samples become difficult to manufacture with manually embedded fibre.

4.3.2 Tensile Samples

Tensile samples were modelled to the dimensions of BS EN ISO 527-2:2012 [54,55], as shown in Figure 4.3.2:1. Each set of 6 samples were printed concurrently when possible. Samples D2 and D3 were printed in multiple batches due to limiting print space due to reorienting of the fibre blocks.

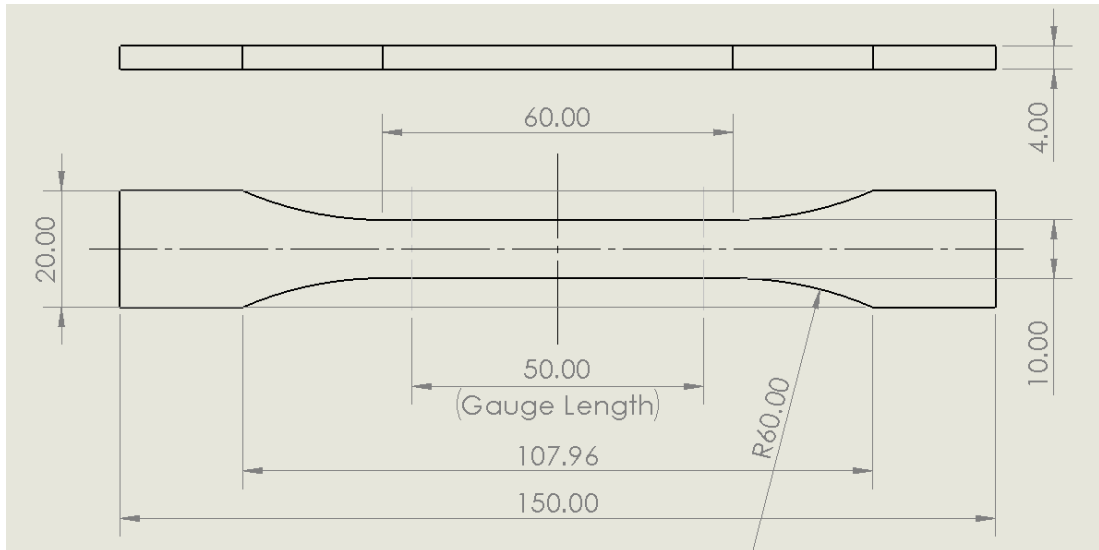


Figure 4.3.2:1 Tensile specimen dimensions(BS EN ISO 527-2:2012)

The fibres embedded in tensile samples (Figure 4.3.2:2) were of the polyimide variety with a diameter of 155 μm (0.155 mm), narrower than the 200 μm (0.2 mm) layer height.



Figure 4.3.2:2 Tensile specimen paused at the mid-layer for fibre insertion.

4.3.3 Flexural samples

Flexural samples were produced to BS EN ISO 178-2019 [56] dimensions (Figure 4.3.3:1). The sample dimensions were that of the preferred test specimen. Sample sets were printed in the same print run where permissible. Fibre samples included fibre blocks orientated to allow desired fibre placement.

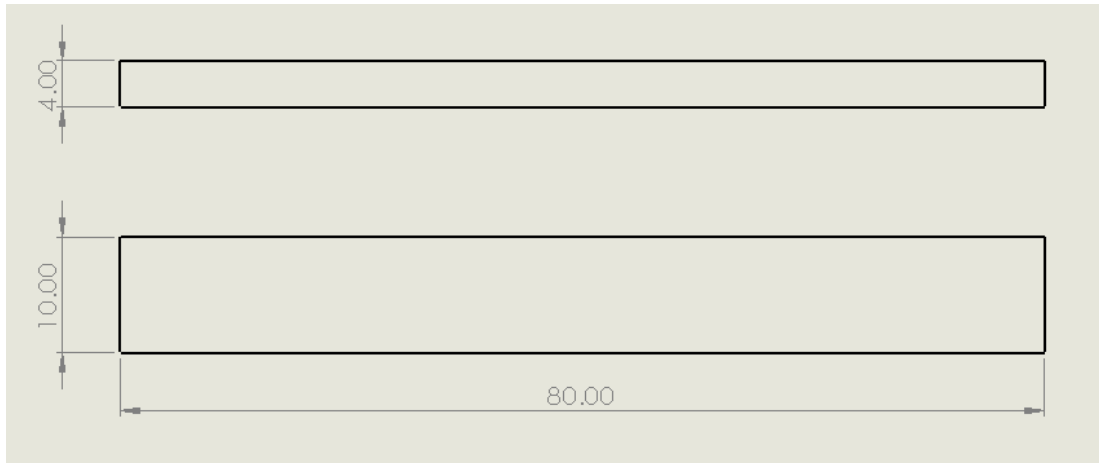


Figure 4.3.3:1 Flexural sample dimensions(BS EN ISO 178-2019).

No warping was observed. Flexural samples were considerably smaller than tensile ones allowing for printing to occur closer to the print bed centre (Figure 4.3.3:2), hence better bed adhesion.

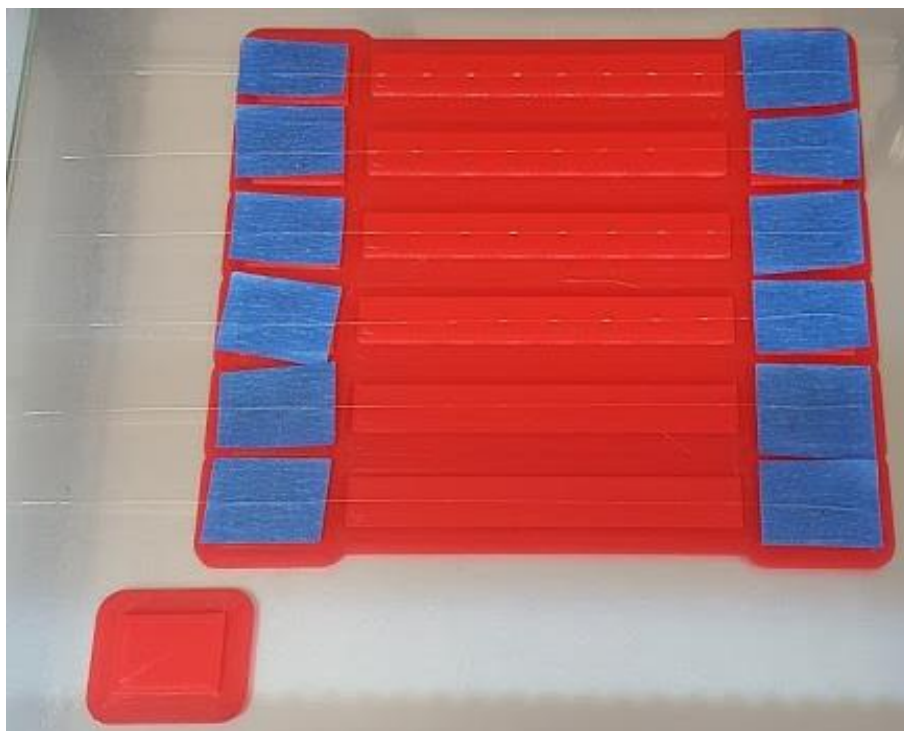


Figure 4.3.3:2 Flexural samples paused mid-print. The purge block is shown bottom left.

4.3.4 Fibre Pull-out

No suitable standard existed at the time for testing the pull-out load for optical fibres embedded in FDM 3D printed samples. Therefore, Samples of dimensions 5 x 12 x 50 mm were produced to allow for easy production and compatibility with the designed fixture jig outlined in Section 4.4.4.

As with previous types, samples of the same sort were printed together. Smaller dimensions of the fibre pull-out specimens allowed the printing of multiple types in the same print job.

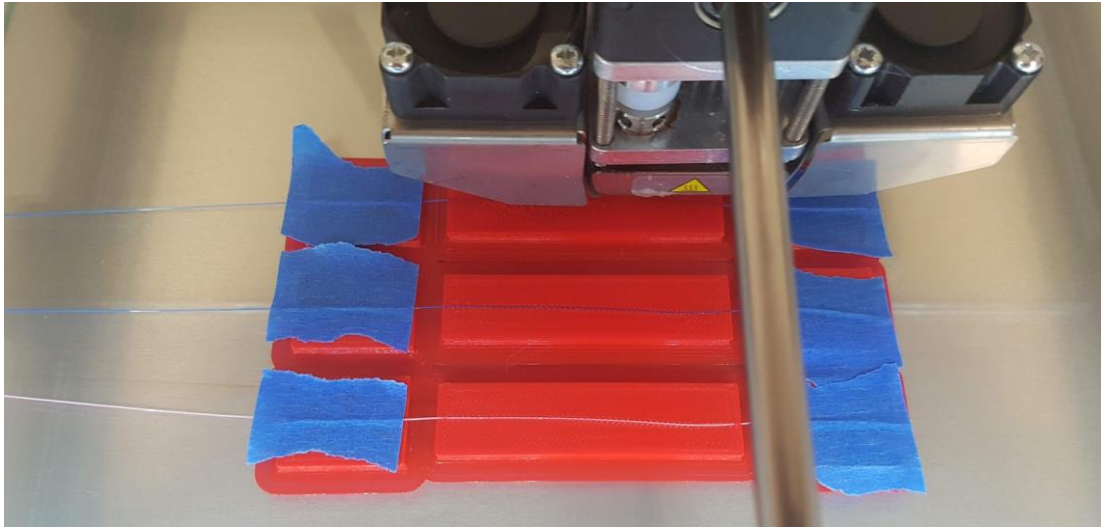


Figure 4.3.4:1 Fibre pull-out samples just after the print resume.

4.3.5 Issues Encountered

- In occasional instances, samples located closest to the edge of the print bed exhibited warping. These samples were discarded and re-printed.
- Due to the limited area around the build plate, it was difficult to keep the fibre perfectly straight and taught. Once printing recommenced the nozzle occasionally caused the fibre to move out of position. Resulting in a non-straight fibre path through the specimen. This appeared more likely to occur when raster lines were perpendicular to the fibre.
- Inclusion of acrylate and high temp. acrylate fibres were not ideal as the fibre diameter was greater than the individual layer height. This resulted in the nozzle contacting the fibre and, in some instances moving it slightly. One resolution would be to increase the height of the layer preceding the fibre.

4.4 Testing

4.4.1 Micro-CT X-ray Imaging

4.4.1.1 Imaging

Images were obtained using a Nikon XT H 225 system utilising a tungsten target, alongside a Varian 2520 detector with a resolution of 1900 x 1500 and 127 μm pixel size. No filter was used. Samples were mounted in a vice-like jaw system with the minimal feasible amount of sample clamped, as the portion of material within the jaws could not be imaged.

Preliminary scans showed power values of 100 kV and 120 μA were suitable and used for all subsequent samples. The 'optimise projections' option was selected resulting in 3015 projections with 4 frames per projection.

Figures Figure 4.4.1:1 and Figure 4.4.1:2 show the specimen chamber of the Nikon μCT machine, highlighting key components and the coordinate system used.

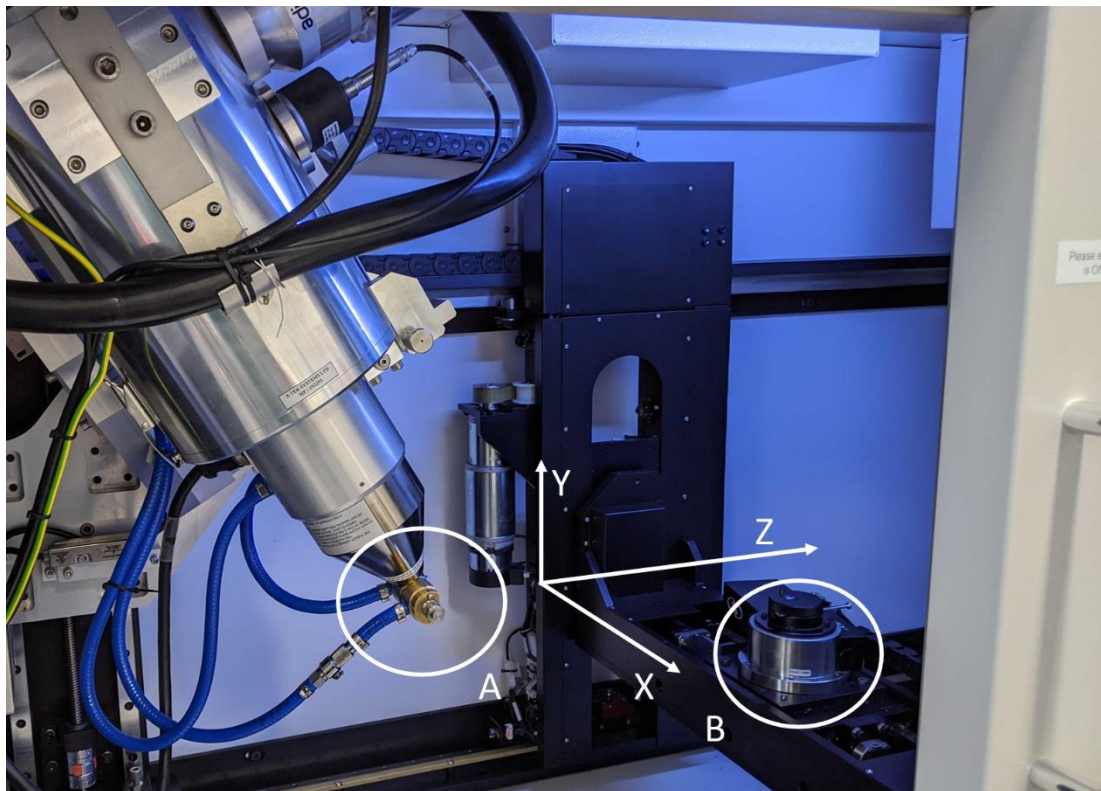


Figure 4.4.1:1 Chamber of the Nikon XT H 225. A) The 'gun' where X-rays emerge in a cone-shape towards the detector. B) Rotary stage onto which the specimen is mounted, capable of 360° movement. X, Y and Z-axis directions are also highlighted.

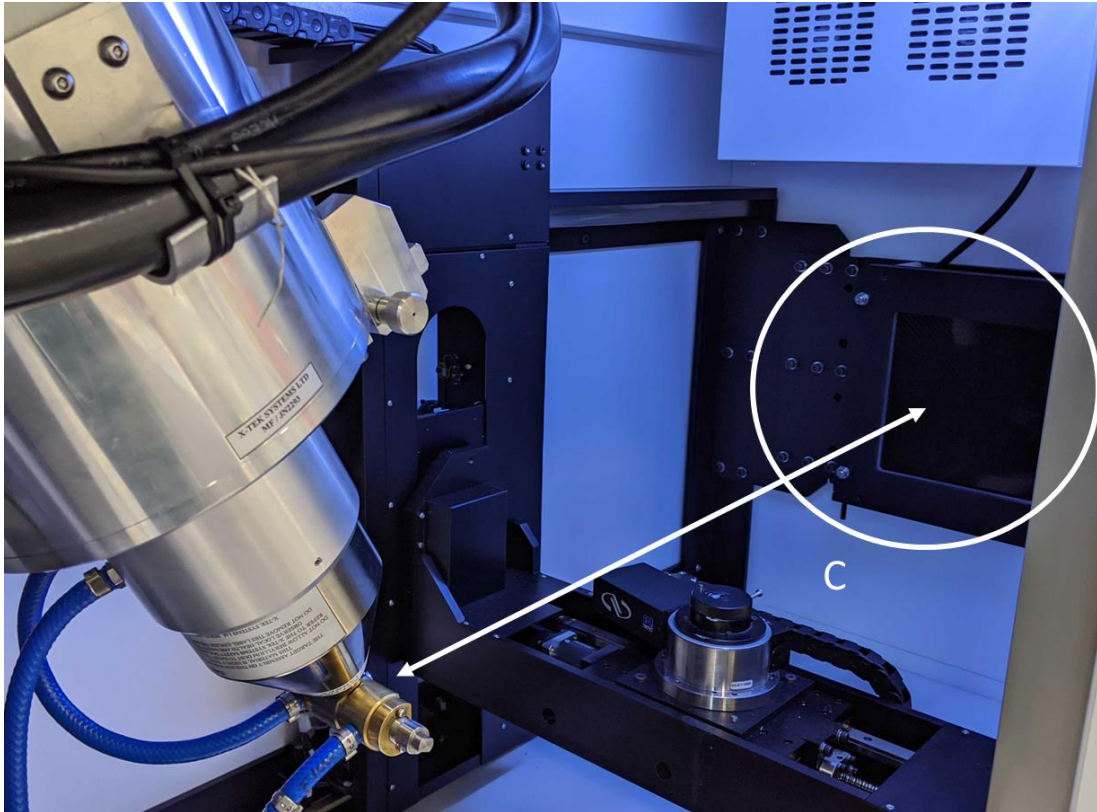


Figure 4.4.1:2 Nikon XT H 225 gun, and detector. Circle C highlights the detector plate. The arrow (Z direction) is used to control the level of zoom on the specimen.

4.4.1.2 Reconstruction & Image Manipulation

Upon scan completion output files were transferred from the machine for reconstruction using Nikon's CT Pro 3D software. The software consists of several tabs to check scan quality, adjust output parameters, and reduce artefacts and noise.

Initially, object alignment is checked by the user by comparing sequential images to ensure the object did not move during scanning. Failure at this phase requires rescanning of the sample. Next, the centre of object rotation is found automatically, considering any axial misalignment caused by an imperfect scan setup. Beam hardening and noise artefacts can then be mitigated algorithmically, the optimal solution is selected visually by the user. Output volume size is manually minimised by removing dead space around the specimen. This helps reduce output file size. Once parameters are finalised the file is set for reconstruction to produce a .raw and .vol file.

The files were then imported into ORS Dragonfly for image manipulation and view selection. Firstly, the window levelling histogram was adjusted by dynamically altering the brightness and contrast to produce a clear image of the specimen.

A 4-scene view was used to orient the image to give clear views of the structure laminations, infill pattern and embedded fibre. Three primary views in each plane, XZ (plan), YZ (side elevation) and XY (front elevation), along with a secondary selected view were used to display each specimen. The model was aligned along the centre plane of the fibre in the plan and side elevation views. Theoretically, this should also be the centre plane of the first raster layer after fibre insertion. In specimens where the fibre had been displaced, the best visually average plane intersecting the centre of the fibre was chosen to display as much of the fibre as possible. The front elevation view of the sample was aligned with the bottom printed edge of the sample.

4.4.2 Tensile

As per sample fabrication, BS EN ISO 527:2012 [54,55] was used to provide guidelines for sample tensile testing. A Hounsfield H25KS tensile machine and associated 25 KN load cell were utilized. Table 4.4.2-1 shows a summary of the parameters used for tensile testing.

Table 4.4.2-1 Summary of tensile testing parameters.

Standard	BS EN ISO 527:2012
Test speed (mm/min)	1.0
Gauge Length (mm)	50.00
Initial Grip Distance (mm)	115 ±1
Number of specimens	6

Digital Vernier callipers were used for sample measurement, making sure to avoid any left-over brim material. BS EN ISO 16012-2015 [57] was used as guidance. Average values for gauge width and thickness were recorded by taking measurements at the centre and either end of the gauge section. The calliper zero setting was checked between each specimen. Dimensional conformance to the standard was checked but no specimens were discarded. Further details are discussed in Section 5.2.1.

After measuring, each sample was loaded into the tensile rig and secured using mechanical wedge grip jaws. The initial grip distance was 115 ±1 mm. Grip distance was set by moving the jaws together until touching, zeroing grip distance readout, then moving them apart 115 mm as per machine readout. The distance was confirmed using a rule. Specimen position and grip force were both done manually with care taken to maintain consistency between tests.

Once secured, an axial extensometer (Epsilon Model 3542) with gauge length 50 mm, was attached and visually centred on the gauge section of the specimen. The pin remained in until test initialisation. The extensometer was connected via the Hounsfield computer system.

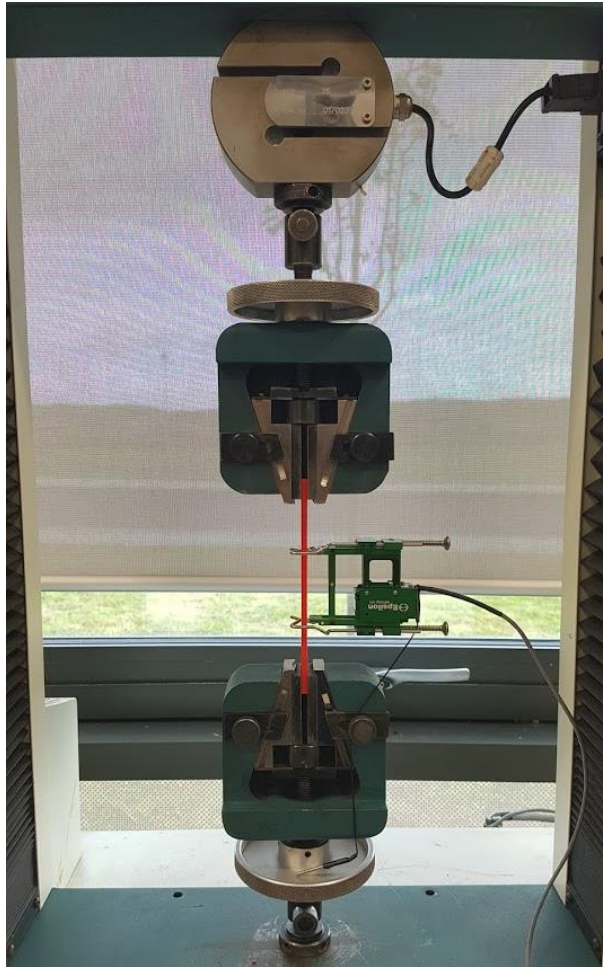


Figure 4.4.2:1 Tensile test setup.

All readouts were zeroed via the connected PC and confirmed on the test equipment readout screen. Testing was then initialised at 1 mm/s with strain, extension and force data points being logged every 0.5 seconds.

Neither the tensile rig nor the load cell used was recently calibrated prior to testing. This did not pose a restriction as results were wanted to provide a relative comparison between plain and fibre samples. Absolute values were not a target of this project.

4.4.3 Flexural

Flexural testing was completed using a 3-point bending test on the same Hounsfield H25KS test machine and accompanying 1 kN load cell. General guidelines were derived from BS EN ISO 178-2019 [56], with Table 4.4.3-1 summarising key testing parameters used.

Table 4.4.3-1 Summary of flexural testing parameters.

Standard	BS EN ISO 178-2019 [56]
Test speed (mm/min)	2 (plain), 5 (fibre)
Span Distance (mm)	64
Number of specimens	6

Samples were firstly visually checked and then measured using digital Vernier callipers, avoiding remaining brim material, as per tensile specimens. The width and thickness of each sample were measured at the centre point and the cross-sectional area calculated. Average width and thickness values across each sample set were calculated to check for non-conformities. No specimen was discarded with further discussion in results Section 5.3.1.

Samples were individually loaded onto the 3-point bending test apparatus. The distance (span) between supports was set to 64 mm using a rule and measuring from the centre of the radiused supports. The 64 mm span distance is for the preferred test specimen used and defined in Equation 1 from the ISO standard.

$$L = (16 \pm 1)h \quad \text{Equation 1}$$

Where: L = Span (mm), h = Specimen height (mm).

Each specimen was positioned centrally on the test rig so that the applied load acted on the midspan of the specimen and was determined visually.

A small amount of preload was applied by gradually lowering the crosshead until a small amount of resistance was felt by hand when moving the sample within the test rig. Readouts were zeroed via the connected PC and confirmed on the machine display.

A test speed of 2 mm/min was used for the plain samples as defined by Equation 2.

$$v = \frac{rL^2}{600h} \quad \text{Equation 2}$$

Where: v = Test speed (mm/min), r = Strain rate (%/min), L = Span (mm), h = Specimen height (mm).

Testing speed was increased to 5 mm/min for fibre samples to reduce testing time. This still complies with BS EN ISO 178 and results in an approximate strain rate of 3 %/min, opposed to the ideal 1 %/min.

Samples were tested until a displacement of 10 mm. This was found to be beyond the required 5 % strain criterion, but as the standard is not targeted towards 3D printed specimens it was opted to test to a point of guaranteed failure.



Figure 4.4.3:1 Flexural testing underway. The image shows preliminary testing underway with a 50KN load cell. A 1KN load cell was used to gather results.

4.4.4 Fibre Pull-out

No ISO standard was available for testing the required pull-out force of optical fibres from FDM 3D printed components. Therefore, a method and apparatus were devised to secure specimens for fibre pull-out testing within a tensile test machine.

Samples were required to be tested without application of clamping force. Added clamping force without precise measurement and consistency would, in turn, apply an extra compressive force to the embedded fibre. A retention plate with a slot for the fibre was manufactured to allow the specimen to be secured whilst tension is applied to the embedded fibre without clamping. Figure 4.4.4:1 and Figure 4.4.4:2 show the retention mechanism and a specimen installed. The 2 side bolts are to hold the specimen in place whilst the free fibre end was secured. These were fully released before testing.



Figure 4.4.4:1 Retention apparatus for fibre pull-out.

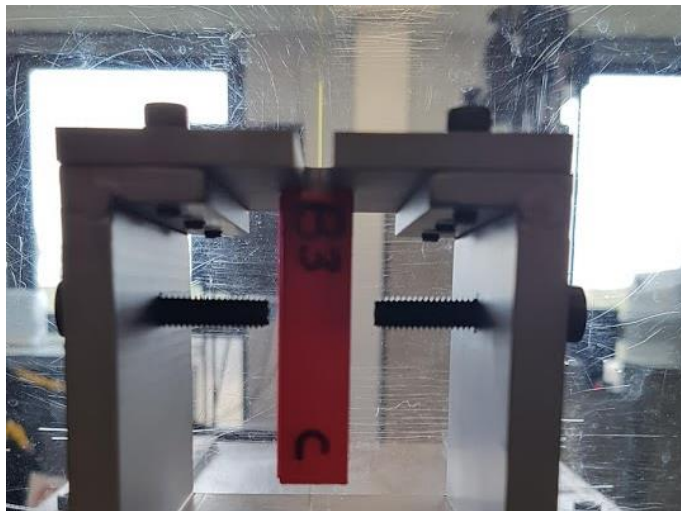


Figure 4.4.4:2 Specimen in fibre pull-out test rig.

40 mm of the free end of the fibre was sandwiched between a length of cardboard and adhered to using PVC hot glue. This enabled secure clamping of the free end in jaws to allow the application of tension without slippage. Preliminary testing showed no slipping either between the optical fibre and cardboard or between the cardboard and the clamp. Figure 4.4.4:3 shows a sample secured within the testing rig. Slack in the fibre was taken up by manually raising the crosshead until the specimen just contacted the underside of the retention plate.



Figure 4.4.4:3 Fibre pull out sample fully secured in the test rig.

Preliminary testing found required forces to dislodge the fibre were low, hence the smallest available load cell of 1KN was selected. Table 4.4.4-1 gives a summary of testing parameters.

Table 4.4.4-1 Summary of fibre pull-out testing parameters.

Standard	N/A
Test speed (mm/min)	2
Number of specimens	3

A test speed of 2 mm/min was chosen so as to be similar to tensile and flexural testing. Testing was halted at a crosshead displacement of 5 mm. This was shown to be sufficient for fibre displacement.

5 Results and Discussions

Results are split by the form of testing: Micro-CT, Tensile, Flexural, Fibre pull-out, and a final summary. Tensile and flexural results have been separated into several parts. Firstly, specimen dimension results are discussed, mean results with standard deviation values are tabulated and displayed for plain and fibre specimens. Sub-sections are divided by the type of modifications made to the fibre samples.

5.1 Micro-CT X-Ray Images

Details of each specimen type are summarized in tabulated form. Images for sample groups are under a single heading to aid in comparison and avoid repetition of details.

Finally, a summary of the CT images is provided to state common themes and details present in the scan images.

Figure 4.4.4:1 below depicts and defines the orientation of view planes of each sample.

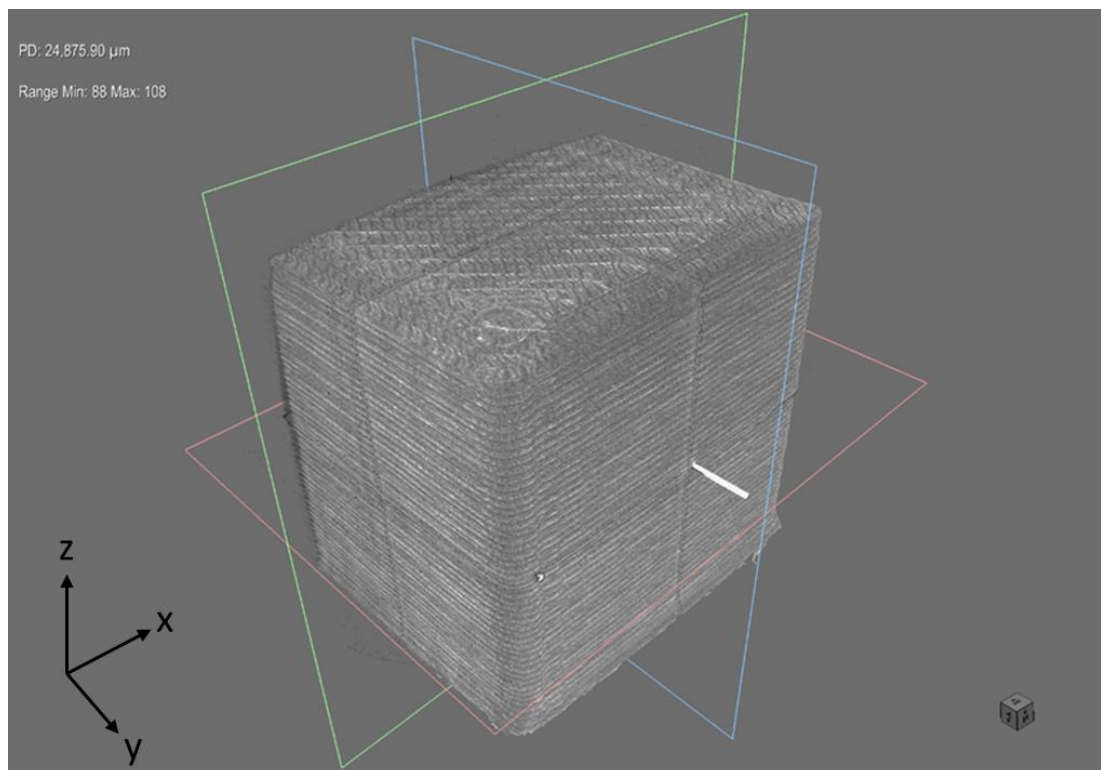


Figure 4.4.4:1 Axis planes in ORS Dragonfly in 3D model view. The red plane is orientated in the XY plane, plan views are in this plane. The blue plane is in the YZ plane and provides side elevation views. The green plane is in the XZ orientation, front elevation views are in this plane. This coordinate system does not match that of the Nikon X-ray machine.

The red bounding box defines the XY plane, this shows top-down or plan views of the structure. The blue plane defines the YZ plane, images taken here are side elevation views.

Finally, the green plane shows the XZ plane, this represents front elevation views of the sample. The fibre embedded optical fibre is displayed in white.

5.1.1 A1

Table 5.1.1-1 Sample A1 μ CT details.

Infill Parameters	SFI
Fibre Type	Polyimide
Variable	No altered print parameters. Embedded fibre for direct comparison to plain sample.

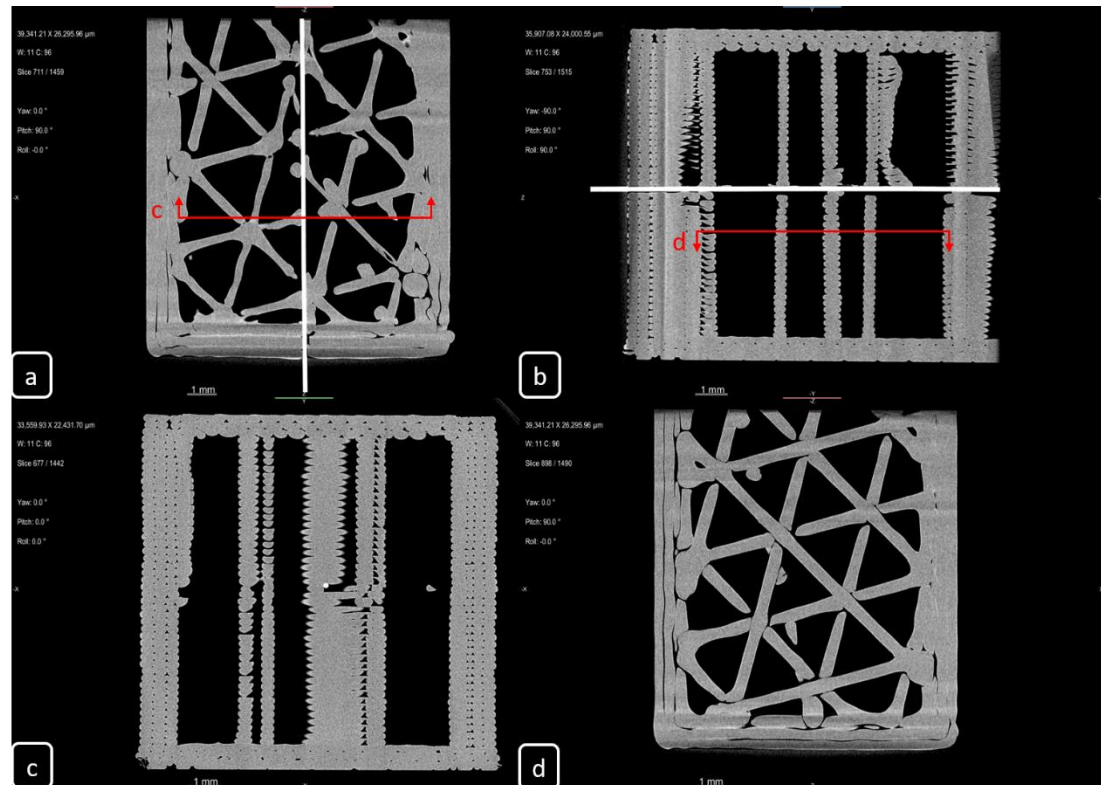


Figure 5.1.1:1 Sample A1 CT slices. a) Plan view, slice intersects the mid-point of the fibre. The fibre is shown to have not been disturbed by the nozzle. b) Side elevation view, slice intersects the mid-point of the fibre and shows the fibre has remained taught and not drooped into any cavities. c) Front elevation view in the middle of the specimen. d) Secondary plan view showing a layer prior to fibre insertion, the slice intersects the middle of the layer. Views 'c' and 'd' slice locations are shown in 'a' and 'b', respectively.

Figure 5.1.1:1 shows slice images for sample A1. Plan view 'a' shows that the fibre position has not been disturbed by material deposition and remains straight. Print direction for each raster line crossing the fibre can be suggested by looking at material voids on either side of the fibre. The side with material right up to the fibre can be stated as the incoming direction while the side with no material next to the fibre the trailing direction as the fibre momentarily alters material flow.

The side elevation view in 'b' shows the points at which the infill intersects with the fibre. Notably, the fibre has not slumped into the infill voids and has remained taught.

View 'c' shows a front elevation view where an infill raster intersects the fibre and displays the material gap left after the fibre. Similarly, to view 'a', a void is seen directly to the right of the fibre indicating that material flow is interrupted as the nozzle passes over the fibre.

Plan view 'd' shows a mid-layer image before the fibre is embedded. This depicts a layer indicative of a plain sample, enabling comparison between a plain and fibre inclusive sample without scanning an individual plain sample.

Material flow and deposition appear to be more reliable in the layer without fibre (d), with wider and more consistent infill raster lines. Similar to the fibre inclusive layer, breaks in the material are still present where the nozzle has crossed previously deposited rasters, but these gaps are considerably smaller than with the fibre present as in image 'a'.

5.1.2 A2

Table 5.1.2-1 Sample A2 μ CT details.

Infill Parameters	80% Concentric
Fibre Type	Polyimide
Variable	No altered print parameters. Embedded fibre for direct comparison to plain sample.

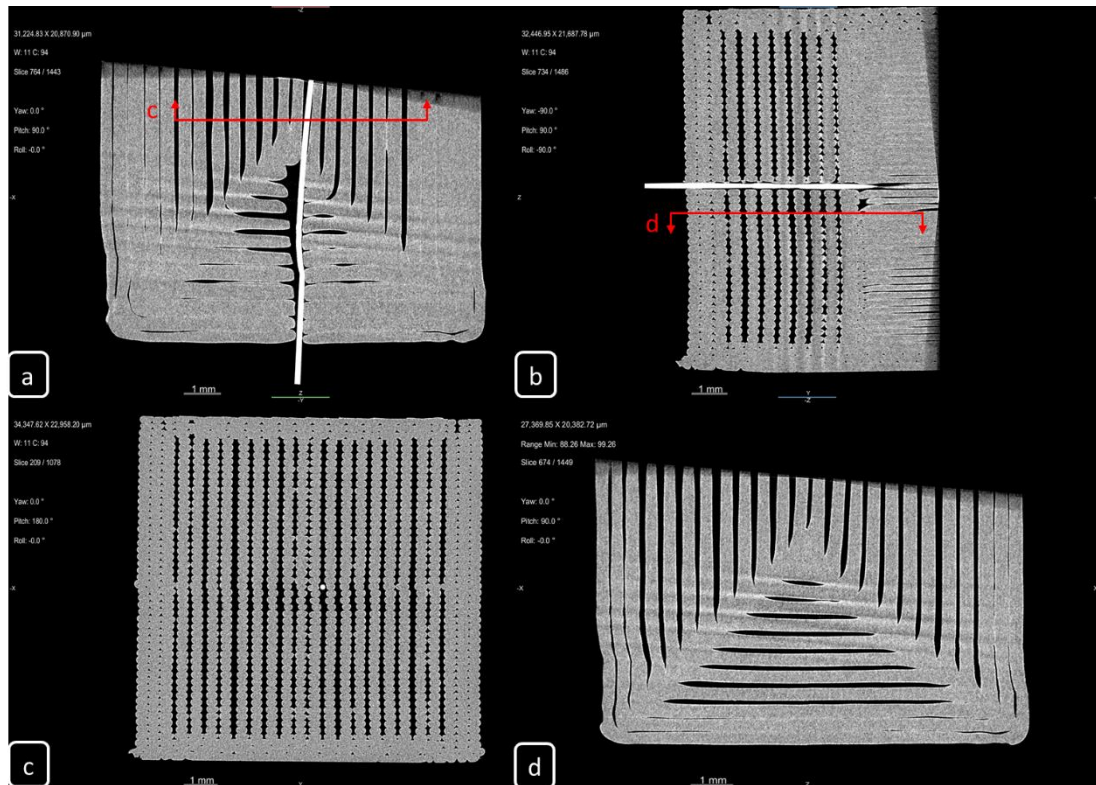


Figure 5.1.2:1 Sample A2 CT slices. a) Plan view, slice intersects the mid-point of the fibre. The fibre has been moved off the central axis, likely by the central raster ring. Voids are seen on the left side of the fibre suggesting a clockwise print direction. b) Side elevation view, slice intersects the mid-point of the fibre. The fibre is not seen on the right side of the slice as it has moved out of the plane. c) Front elevation view at the centre. This view shows gaps in the infill to achieve 80% density vs. the shell walls. d) Secondary plan view showing a layer prior to fibre insertion, slice intersects the middle of the layer. Raster lines and voids appear to be more uniform compared to slice 'a' with the fibre present. Corners show increased material deposition where the flow has not been reduced enough as the print head slows before changing direction. Views 'c' and 'd' slice locations are shown in 'a' and 'b' respectively.

Figure 5.1.2:1 shows slice images for sample A2. The plan view, image 'a', shows that the fibre is not centrally aligned along the XY plane, likely having been displaced by the print nozzle towards the central concentric raster. This can be expected to occur using concentric infill if the combination of specimen size, infill parameters and fibre diameter leads to the central void being smaller than the fibre diameter. Print direction can be established as right to left or clockwise, shown by gaps in material deposition on the left-hand side of the fibre in image 'a'. Fibre movement could be mitigated by printing from the outside to the inside causing the outer rasters to possibly hold the fibre in place as the centre rings are printed.

The plan view in image 'a' shows the 3 perimeter walls are deposited in an equal manner to the concentric infill but without gaps between to give the requested 80% infill density. Voids found between concentric rings of the infill are non-uniform in size or distribution. Voids adjacent to the fibre increase in volume towards the central concentric ring.

Image 'b' displays the perpendicular and axial infill lines in a side elevation view. The fibre is not visible throughout the entire image due to the displacement. The raster layer directly

above the fibre is seen to have extra material in between lines, likely from the previous layer material being pushed up over the fibre.

Image 'c' is a mid-sample plane showing all concentric infill rasters to be running axially with the fibre. The image reveals raster lines around the fibre may have been marginally displaced or compressed horizontally to accommodate the fibre. However, it is difficult to say for certain as many of the infill raster lines vary in shape and size.

Image 'd' depicts a raster layer prior to fibre integration. This, as in sample A1, is indicative of a plain sample. In comparison with the fibre containing layer in 'a', it shows a more uniform structure with consistent void locations. However, the corners of each ring show more material has been deposited than the straight edges. This may be due to the slicer not altering material flow correctly to compensate for the deceleration of the print head as it changes direction.

5.1.3 B1, B2, B3

Table 5.1.3-1 Samples B1, B2 and B3 μ CT details.

Infill Parameters	SFI with 100% layers
Fibre Type	Polyimide
Variable	Number of extra layers surrounding the fibre. B1 - 1 layer either side. B2 - 2 layers either side. B3 - 5 layers either side.

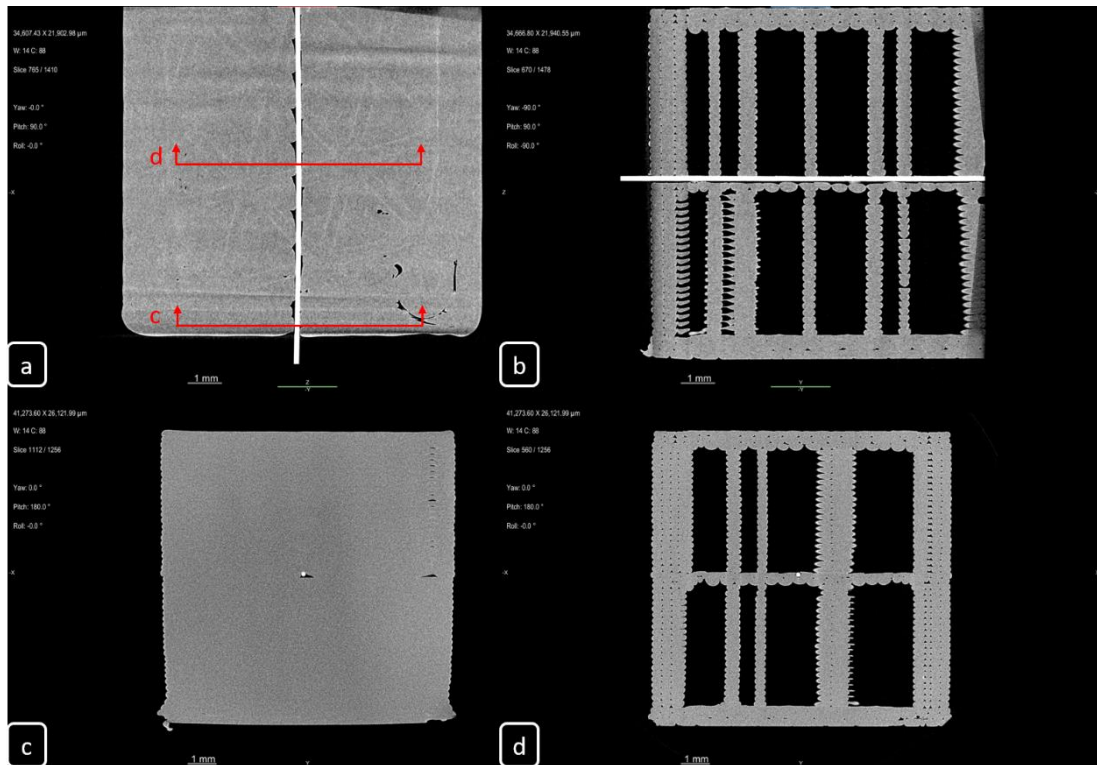


Figure 5.1.3:1 Sample B1 CT slices. a) Plan view, slice intersects the mid-point of the fibre. The triangular infill pattern is still visible. The fibre has remained straight and there are small repeating voids adjacent to the fibre. b) Side elevation view, slice intersects the mid-point of the fibre. The fibre is shown to sit above the first solid layer which has not slumped into the voids. The 45° angle and crossing of infill raster lines is what causes some to look wider than others. c) Front elevation view, slice location is cutting through the middle of raster line of the shell. A void is present to the lower right of the fibre where material was unable to flow. d) Secondary front elevation view, slice location is in the centre of the sample. This view shows the fibre sitting on top of the first solid layer and surrounded by the second. Views 'c' and 'd' slice locations are shown in 'a'.

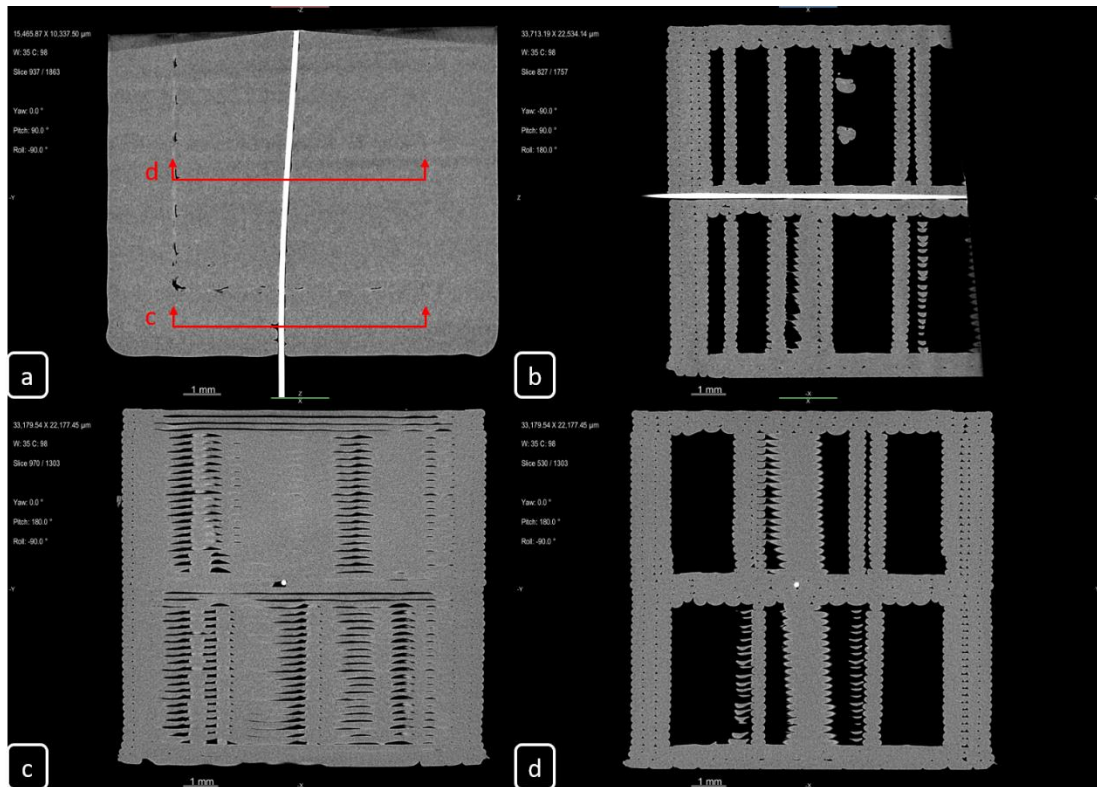


Figure 5.1.3:2 Sample B2 CT slices. a) Plan view, slice intersects the mid-point of the fibre. Unlike sample B1 the fibre is not straight. However, there are almost no voids on either side of the fibre within the infill. Small voids are visible at the shell walls. b) Side elevation view, slice intersects the mid-point of the fibre. Small void areas are visible below the fibre. c) Front elevation view, slice location is in between shell raster lines. Many voids are shown in between, this may be due to the cylindrically shaped fronts not packing together perfectly. A void pocket is also present to the bottom left of the fibre. d) Secondary front elevation view, slice location is in the middle of the sample. Views 'c' and 'd' slice locations are shown in 'a'.

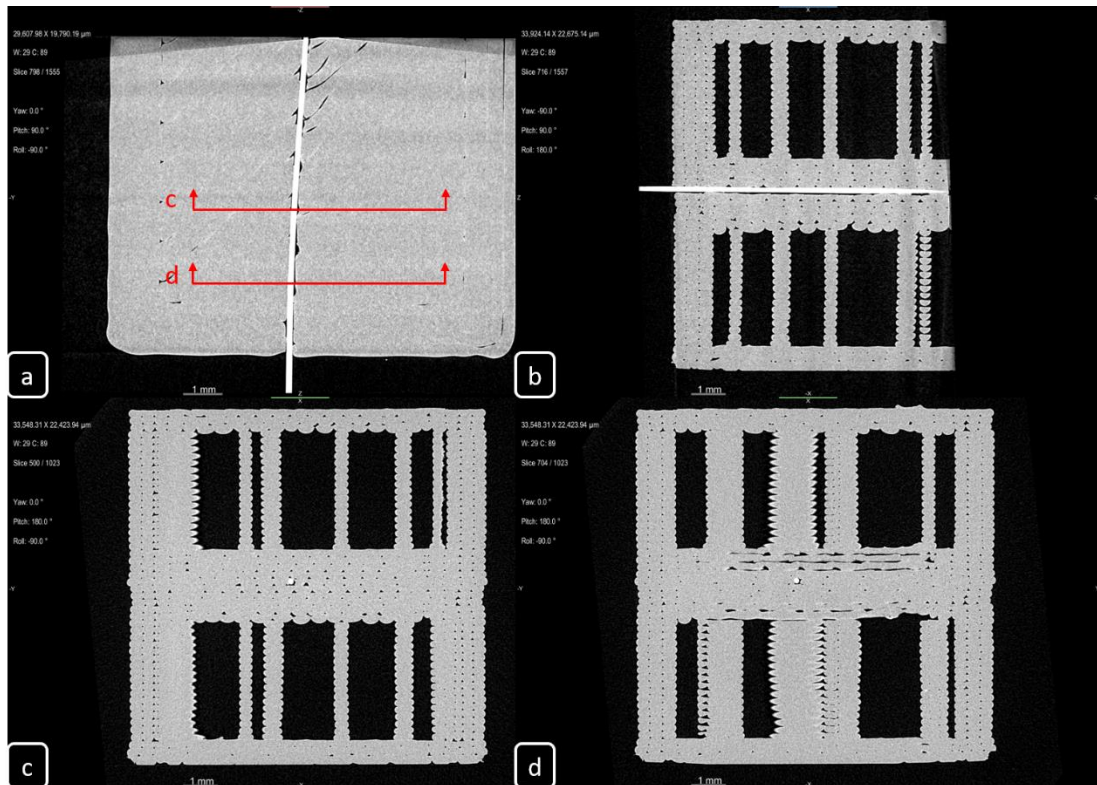


Figure 5.1.3:3 Sample B3 CT slices. a) Plan view, slice intersects the mid-point of the fibre. The fibre is shown to be slightly off-axis, possibly caused by the manual method of embedding. Voids exist around the fibre at all points. b) Side elevation view, slice intersects the mid-point of the fibre. Once more a void is shown below the length of the fibre. c) Front elevation view, slice location is in between shell raster lines. d) Secondary front elevation view, slice location is in the middle of the sample. Views 'c' and 'd' slice locations are shown in 'a'.

Figure 5.1.3:1, Figure 5.1.3:2 and Figure 5.1.3:3 show slice images for samples B1-3, respectively. Samples B1, B2 and B3 have the same makeup but differ in the number of solid layers surrounding the fibre, with 1, 2 and 5 layers, respectively. Image 'b' in Figure 5.1.3:1 shows the fibre as part of the second layer as opposed to being covered by a solid layer. Image 'a' in the same figure shows an impression of the triangular infill onto which the first solid layer is deposited.

Voids exist in all 3 samples underneath the fibre. This is most pronounced in sample B1 where the single layer prior to the fibre has sagged into the previous infill regions. The extra solid layers in sample B2 and B3 have mitigated this before the fibre inlay, but it is still present. This may be caused by multiple factors: a slightly rough surface onto which the fibre is placed, the fibre blocks external to the sample used during fabrication may be fractionally higher, layers having to fill gaps where the previous one has sagged into the infill void or a combination.

Samples B2 and B3 exhibit some degree of fibre displacement from the specified linear path. This is a smooth curve, suggesting a slight misalignment in the manual manufacturing stage rather than a sudden direction change caused by a nozzle collision, e.g. Sample A2 image 'a'.

5.1.4 C1, C2, C3

Table 5.1.4-1 Samples C1, C2 and C3 μ CT details.

Infill Parameters	100% lines
Fibre Type	Polyimide
Variable	Number of extra layers surrounding the fibre. C1 - 0° raster angle. Axial to fibre. C2 - 45°, 135° raster angle. Default option. C3 - 90° raster angle. Perpendicular to fibre.

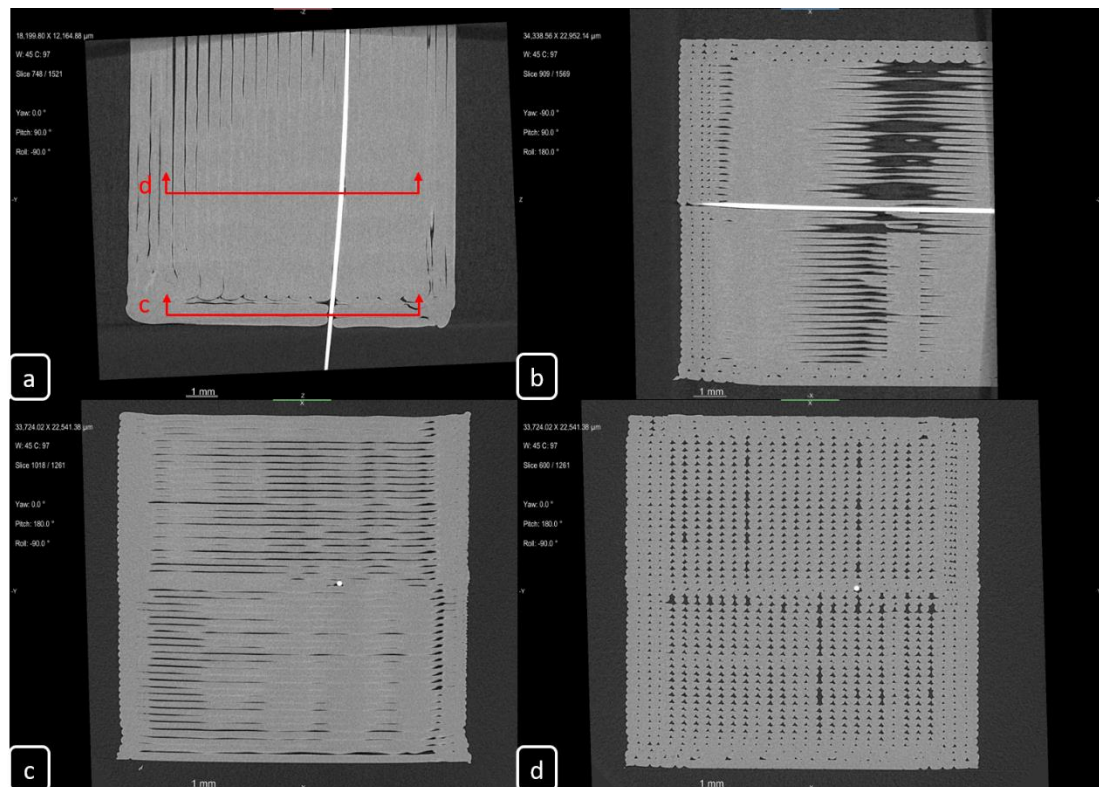


Figure 5.1.4:1 Sample C1 CT slices. a) Plan view 'a' shows the extent of fibre displacement, likely due to the infill direction pushing the fibre, from left to right, rather than printing over to secure it. b) Side elevation. Voids are shown due to the model being rotated in the Z-axis to keep most of the fibre within the image. This makes it difficult to analyse the quality of the fibre embedding. c) Front elevation in between two shell raster lines. The fibre is significantly off centre due to the form of infill. d) Front elevation at a mid-point showing the infill, shell walls and top and bottom surfaces. This displays a clear difference between the 3-layer shell structure and the infill. Even with 100% infill density requested the infill shows larger voids between rasters than the shell.

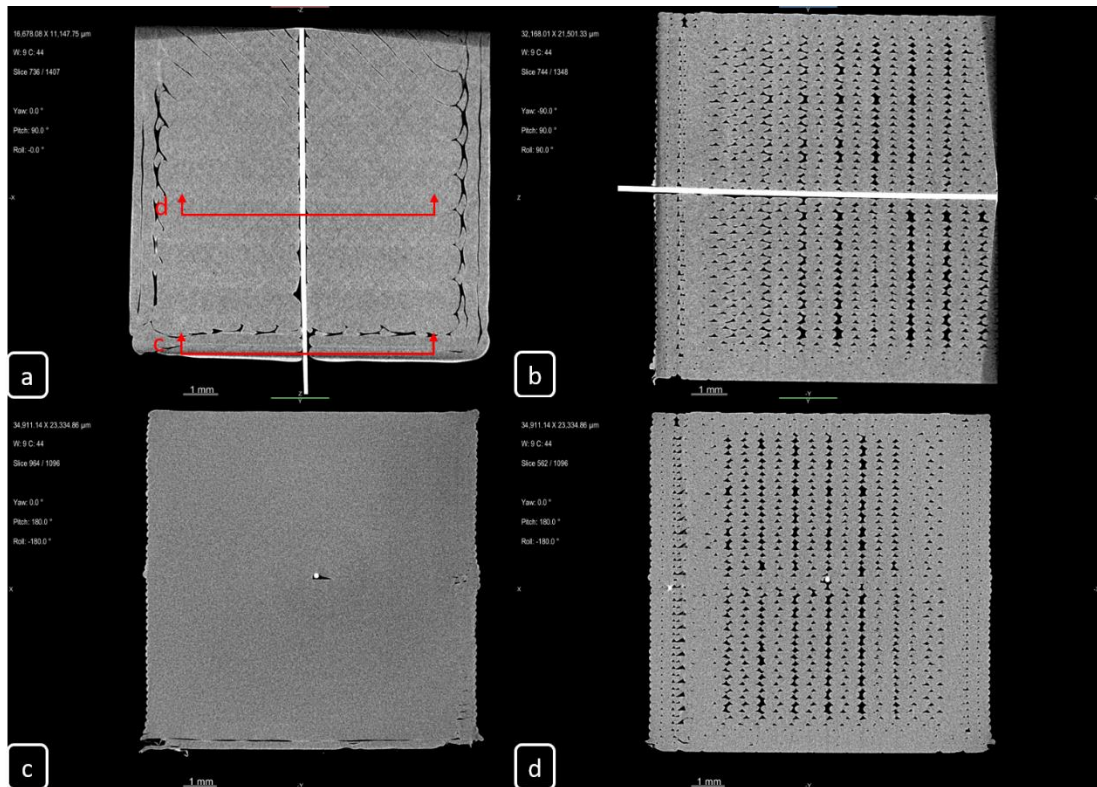


Figure 5.1.4:2 Sample C2 CT slices. a) Plan view shows the fibre is far straighter than in sample C1. The 45° back a fourth print direction keeps the fibre from displacing too far as well as working from one end to the other helping to secure the fibre. Similar voids are seen here as in samples B1-3. However, larger gaps are seen between the infill and shell walls than in the B samples. b) Side elevation shows the fibre is fully supported. 100% infill density is not achieved. The bottom 3 layers show less almost no voids, showing that Cura treats bottom layers differently than infill even though it would be expected to be the same with 100% infill.

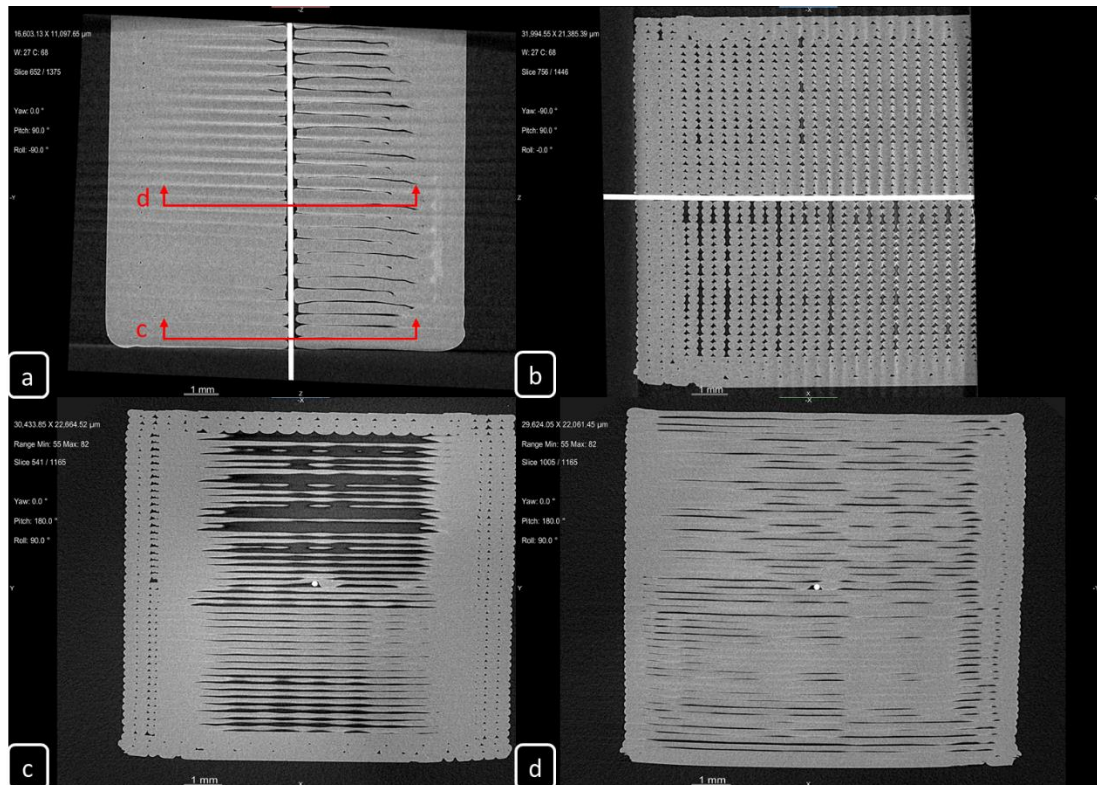


Figure 5.1.4:3 Sample C3 CT slices. a) Plan view. Much like C2, the fibre has not been displaced as in samples C1. The perpendicular infill direction is clearly visible. The infill on the right side of the fibre is significantly different to the left and contains many voids. This is unexpected as material is laid in both directions.

Figure 5.1.4:1, Figure 5.1.4:2 and Figure 5.1.4:3 show slice images for samples C1-3, respectively. The infill raster line direction is clear from the plan view of each sample.

Sample C1 shows a large deviation of the fibre from its intended central path. The order of infill direction can be stated as left to right, causing the fibre to be pushed to the right-hand side. This can happen as the entire fibre portion within the interior of the sample is covered by deposited material in a single raster line. Little to no fibre deviation is visible in samples C2 and C3. Both C2 and C3 infill patterns are completed in an alternating left to right pattern from one end of the sample, and hence fibre, to the other. The first raster lines over the fibre help secure it in place, helping prevent further movement from nozzle interference.

Voids around the fibre, shown in the plan view 'a', appear to be least in C1, and maximum in C3. Fibre encasement in C1 is consistent along the portion of fibre length surrounded by infill with voids existing at the point of intersection with the shell walls. Sample C3 shows large, left-right alternating voids as material is deposited from left to right and back across the fibre. This occurs along the entire fibre length as both the infill and shell material are perpendicular to the fibre.

Sample C2 shows a good combination of minimal fibre displacement and voids surrounding the fibre.

Void areas above and below the fibre in all samples appear relatively equal, particularly when compared to samples B1-B3.

5.1.5 E1, E2, E3

Table 5.1.5-1 Samples E1, E2 and E3 μ CT details.

Infill Parameters	100% lines
Fibre Type	Various
Variable	Fibre buffer E1 – Polyimide E2 – Acrylate E3 – High-Temperature Acrylate

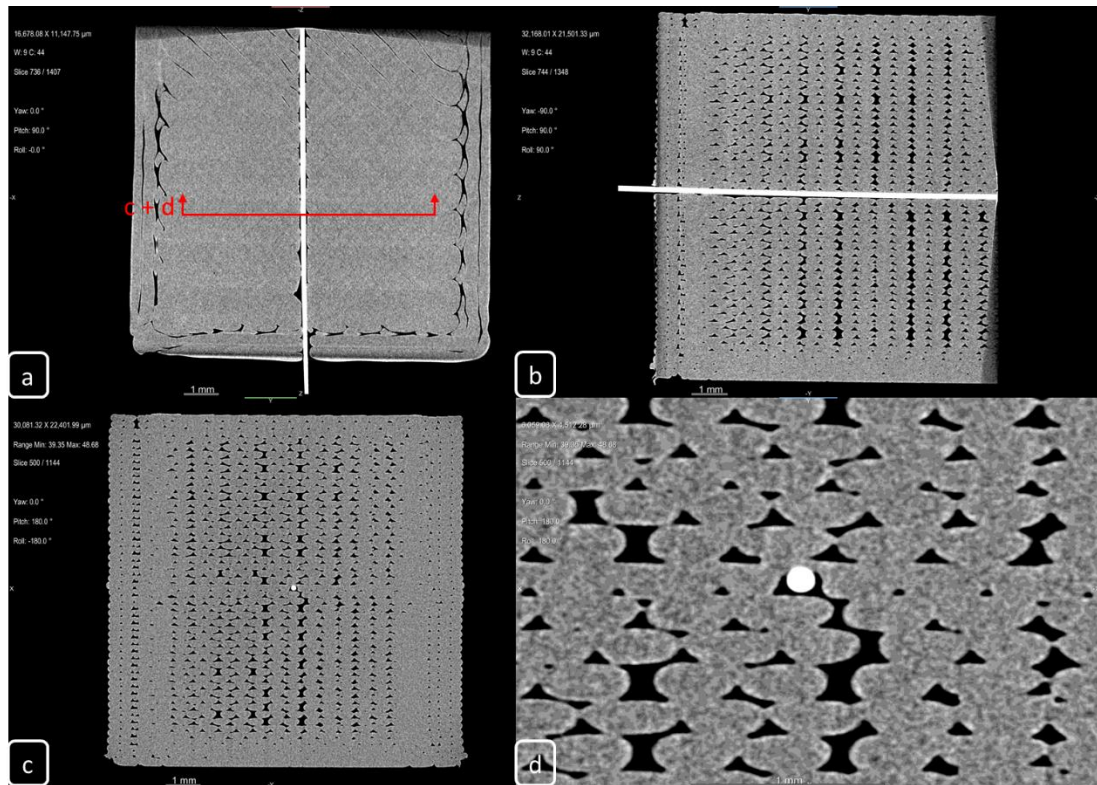


Figure 5.1.5:1 Sample E1 CT slices. Has equal parameters to sample C2 but different slice images are displayed. a) The polyimide fibre is undisturbed as it has a smaller diameter than the layer height (155 vs 200 μ m). b) Side elevation. c) Full front elevation. d) Zoomed section of the same front elevation as in 'c'. It is clear that the fibre diameter is smaller than the requested layer height. Voids either side of the fibre are no larger than those elsewhere in the structure. The polyimide buffer material is not visible but likely to be intact as it has an advertised max. operating temperature of 300 $^{\circ}$ C where the print temperature was 210 $^{\circ}$ C.

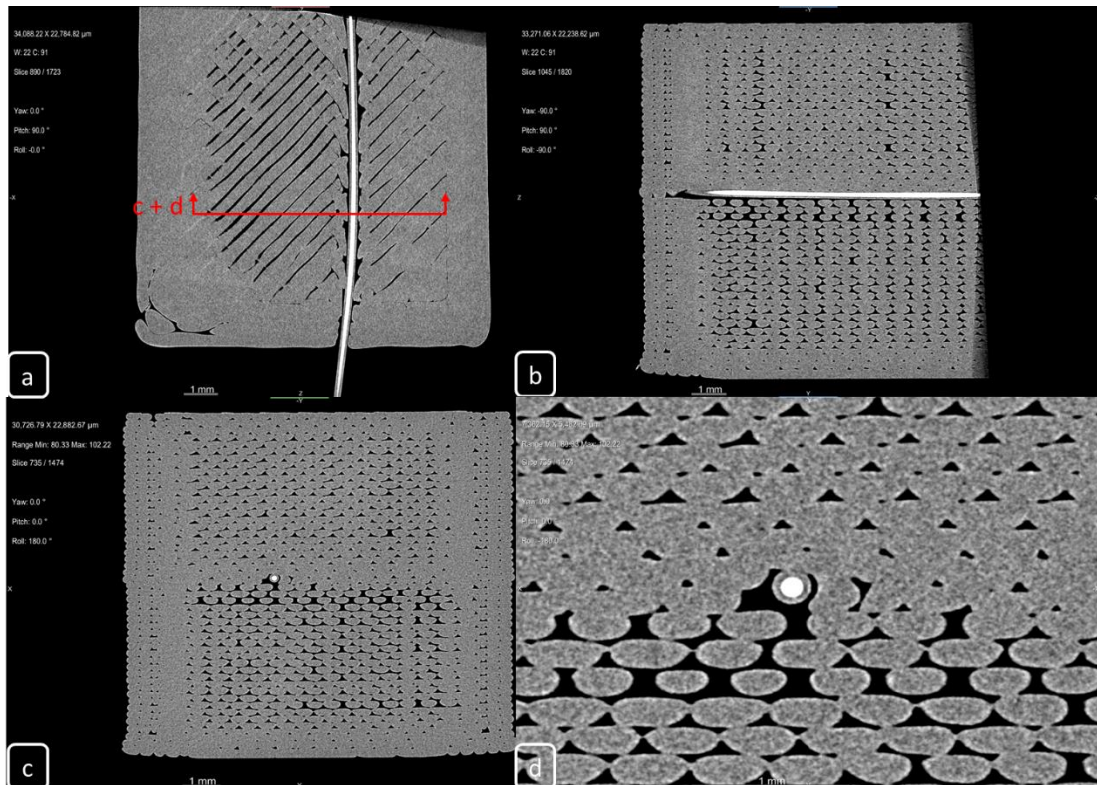


Figure 5.1.5:2 Sample E2 CT slices. a) The acrylate buffer fibre has been displaced due to the diameter of $242\ \mu\text{m}$ being larger than the $200\ \mu\text{m}$ layer height, causing the nozzle to strike it as it passes over. b) Side elevation shows material more densely packed for 3 or 4 layers directly above the fibre. c) Front elevation view shows a similar increased raster density to 'b'. However, it occurs across the width of the specimen indicating that either the fibre has affected the whole width of the specimen or that the increased density is not caused by the fibre. d) Zoomed front elevation view shows the visible fibre buffer. The difference in raster density before and after the fibre is also clear. The buffer material is left intact throughout the length of the fibre even though the reported max. operating temp. is $85\ ^\circ\text{C}$.

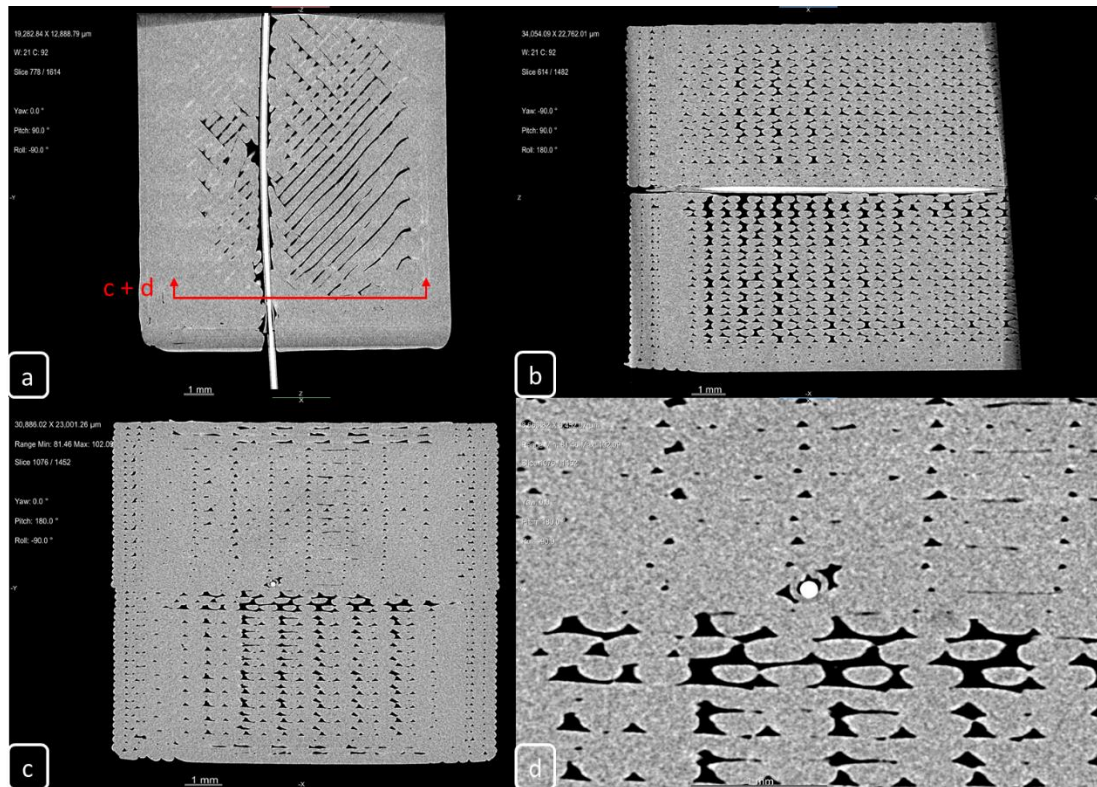


Figure 5.1.5:3 Sample E3 CT slices. a) Plan view. A similar situation to sample E2, the total fibre diameter is greater than the print layer height, at $245\mu\text{m}$ leading to fibre displacement as the nozzle attempts to pass over. b) Side elevation. As in E2, the material density above the fibre is increased over the material below the fibre. c) Front elevation shows the difference in material density above and below the fibre is the same for the width of the sample. d) Zoomed front elevation. Most notably is the 'high-temperature acrylate' buffer has been partially removed from the fibre. This is likely due to the fibre's max operating temperature of 135°C and possibly mechanical action of the nozzle passing over.

Figure 5.1.5:1, Figure 5.1.5:2 and Figure 5.1.5:3 show slice images for samples E1-3, respectively. Fibre displacement is minimal in sample E1 where the fibre diameter is less than that of the layer height. Samples E2 and E3 with fibre diameters larger than the layer height have been displaced a significant amount. Material deposition is also less consistent in samples E2 and E3 compared to E1.

Plan view 'a' depicts many void areas at the infill shell interface and a few around the fibre for sample E1. This is different to E2 and E3 where far fewer voids are presented between the infill and shell, but there are many throughout the infill and around the fibre.

The fibre buffer is visible in all views for E2 and E3. View 'd' in sample E3 shows an instance where the buffer layer has been stripped from the fibre. This is likely caused by the combination of the nozzle temperature (210°C) being greater than the manufacturers stated operating temperature (135°C , Table 4.1.3-1) and the mechanical interaction of the nozzle across the fibre. The nozzle temperature softens the buffer material, then as the nozzle scrapes over the fibre, due to the difference in layer height and fibre diameter, the buffer material is separated.

5.1.6 CT Images Summary

- The infill shape has a significant impact on the quality of the fibre embedding. Infills with raster lines running axially to the fibre cause the fibre to be displaced. i.e. concentric and 0° infill (samples A2 and C1).
- In all instances, some degree of voids exists at the fibre matrix interface. Likely caused by the fibre interrupting material flow. This could possibly be mitigated by increasing the print temperature to encourage improved material flow around the fibre. Equally the cooling fan speed could be reduced to slow material freezing around the fibre.
- Even in samples with 100% density requested, voids still exist. However, the side shell and bottom layers appear to have a higher density than the infill. This could be improved by investigating slicer settings.
- As per Section 4.3.1.1, where 100% density is stated an actual infill density of 99% is requested in Cura. This may be the cause of voids seen in the infill of 100% dense samples. Further comparison and imaging would be required.
- The lowest infill density of 40% does not result in fibre slumping into voids. Further investigation into the lowest permissible infill density would be interesting. Or if the amount of material deposited over the fibre can be made to cause it to slump, e.g. increasing layer height or flow rate.
- Where the fibre diameter is greater than the embedding layer height, the fibre is displaced a large amount, likely due to nozzle interaction. This could be prevented by increasing the layer height for the single layer covering the fibre.
- Fibre with a buffer material with a maximum operating temperature below the print temperature is likely unsuitable for embedding as the buffer may be removed from the fibre. However, it is not clear if this is caused solely by temperature or by temperature and nozzle interaction. As above, could potentially be solved by increasing the layer height of the fibre encapsulating layer.
- Slice images were selected as per Section 4.4.1.2 to prioritise showing the fibre. In instances where the fibre was displaced a large amount, the side elevation view may show raster lines from multiple planes.
- Corners in the XY plane are rounded due to Cura not sufficiently adjusting material flow to compensate for the deceleration of the hot end. Most pronounced in A2 image 'd'.

5.2 Tensile Results

5.2.1 Dimension Results

Specimens with dimensions outside of the specified tolerances have been included as the ISO document followed for tensile testing is not specific to AM. The percentage of samples not within tolerance, along with the maximum dimensional deviation is stated in Table 5.2.1-1.

Table 5.2.1-1 Tensile specimen dimensional conformity.

Specimen type	Dimension	Specified dimension & tolerance (mm)	Percentage non-conforming	Maximum deviation from designed dimension (mm)
Plain	Width	10 ±0.2	6	0.23
	Thickness	4 ±0.2	5	0.27
Fibre	Width	10 ±0.2	19	0.26
	Thickness	4 ±0.2	0	0.16

5.2.2 Tensile Modulus Calculation Correction

Tensile modulus is calculated using the SLOPE function in excel between tensile strain values of 0.05 and 0.0025%. However, this assumes the stress-strain curve is linear within this region. In some instances, this portion of the curve was found to not be linear. For plots with non-linear sections, the SLOPE function range was moved to avoid the anomaly whilst maintaining an equal number of data points and remaining on the linear portion of the curve. Appendix D – Tensile Modulus Correction shows a table of specimens with adjusted modulus values and their modulus values before the adjustment. This modification was only required for plain samples.

These anomalies were likely caused by the physical contact type extensometer slipping during testing. The use of a non-contact type extensometer, such as video or laser-based, would rectify this issue.

Figure 5.2.2:1 shows the stress-strain plot for a plain 20% grid tensile sample (image a), with the requested calculation range (image b), a closer zoom of the anomaly (image c) and the adjusted modulus calculation segment (image d). The region of calculation has been moved past this anomaly into a linear region whilst remaining within the elastic portion of the curve. The vertical dashed lines show the ISO specified region for the modulus calculation (0.0005 – 0.0025 strain).

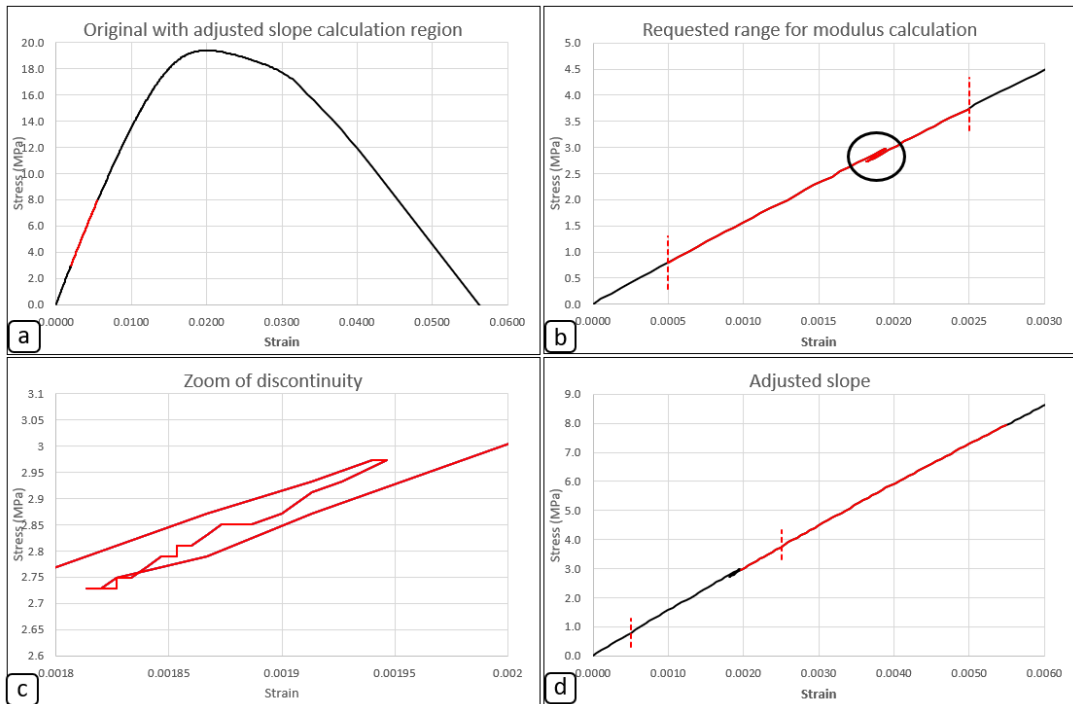


Figure 5.2.2:1 5.2.2 Tensile modulus calculation correction. a) Entire tensile stress-strain plot. The red segment represents the adjusted slope calculation segment still within the linear region of the curve. b) Zoomed section showing requested slope calculation boundaries as per the ISO, this encompasses an anomaly that gives a false slope calculation. c) A further zoomed section to show the anomaly d) The adjusted slope calculation range avoiding the blip. Vertical red dashed lines represent the ISO specified modulus calculation region, as in image b.

5.2.3 Tabulated Mean Values

Table 5.2.3-1 shows tensile test results for plain samples. Table 5.2.3-2 displays the results for fibre inclusive samples. All values are calculated means from the 6 repeats of each sample type.

Table 5.2.3-1 Mean values for plain samples tensile results.

Plain Samples														
Infill Percentage	Infill Pattern	Mass (g)	Ultimate Tensile Load (N)	Std. Dev. (N)	Ultimate Tensile Strength (MPa)	Std. Dev. (MPa)	Tensile Modulus (MPa)	Std. Dev. (MPa)	Ultimate Strain	Std. Dev.	0.2% Proof Stress (MPa)	Std. Dev	Strain at proof stress	Std. Dev.
20	Cubic	5.55	836	30.3	20.18	1.05	1543	54.3	0.016	0.0066	17.56	0.70	0.01317	0.00022
	Grid	5.62	663	296.9	19.41	7.24	1490	55.4	0.019	0.0007	17.35	0.55	0.01358	0.00056
	Triangles	5.67	800	22.6	19.48	0.58	1550	25.5	0.015	0.0066	17.57	0.59	0.01330	0.00044
40	Cubic	6.75	976	48.5	23.38	1.35	1738	89.9	0.020	0.00024	19.84	1.16	0.01339	0.00023
	Grid	6.85	838	21.9	20.33	0.58	1662	41.8	0.019	0.00087	17.45	0.41	0.01248	0.00034
	Triangles	6.77	827	53.8	19.84	1.38	1689	86.3	0.018	0.00023	17.09	1.27	0.01210	0.00050
80	Cubic	8.57	1268	18.3	31.01	0.42	2198	43.9	0.021	0.00039	27.59	0.43	0.01454	0.00039
	Grid	9.33	1130	17.1	26.64	0.40	2212	45.0	0.018	0.00042	23.36	0.35	0.01259	0.00026
	Triangles	9.18	1110	18.6	26.12	0.42	2340	39.7	0.016	0.00076	23.41	0.25	0.01203	0.00023
	Concentric	9.25	1809	13.8	44.05	0.45	2902	161.2	0.021	0.00030	39.06	2.05	0.01559	0.00146
100	Lines	9.77	1517	52.9	37.18	1.18	2720	59.5	0.021	0.00036	31.97	1.39	0.01379	0.00047

Table 5.2.3-2 Mean values for fibre samples tensile results.

Fibre Samples													
Sample	Mass (g)	Ultimate Tensile Load (N)	Std. Dev. (N)	Ultimate Tensile Strength (MPa)	Std. Dev. (MPa)	Tensile Modulus (MPa)	Std. Dev. (MPa)	Ultimate Strain	Std. Dev.	0.2% Proof Stress (MPa)	Std. Dev	Strain at proof stress	Std. Dev.
A1	6.85	968	19.2	23.3	0.35	1759	42.1	0.018	0.00094	21.47	0.49	0.01412	0.00043
A2	9.4	1796	22.7	43.4	0.53	2832	85.5	0.019	0.00023	40.42	1.13	0.01627	0.00070
B1	7.78	1025	46.8	24.6	1.15	2039	44.1	0.017	0.00062	22.62	0.89	0.01309	0.00038
B2	7.9	1135	31.0	27.2	0.77	2148	48.9	0.018	0.00076	25.08	0.55	0.01370	0.00035
B3	9.17	1553	41.2	37.1	0.97	2769	70.7	0.019	0.00025	33.90	0.47	0.01427	0.00028
D1	6.85	968	19.2	23.3	0.35	1759	42.1	0.018	0.00094	21.47	0.49	0.01412	0.00043
D2	6.87	869	58.8	20.9	1.44	1763	42.7	0.017	0.00109	18.92	1.12	0.01273	0.00071
D3	6.92	935	30.8	22.3	0.74	1766	43.3	0.018	0.00069	20.16	0.41	0.01344	0.00037

5.2.4 Plain Samples

5.2.4.1 Tensile Modulus

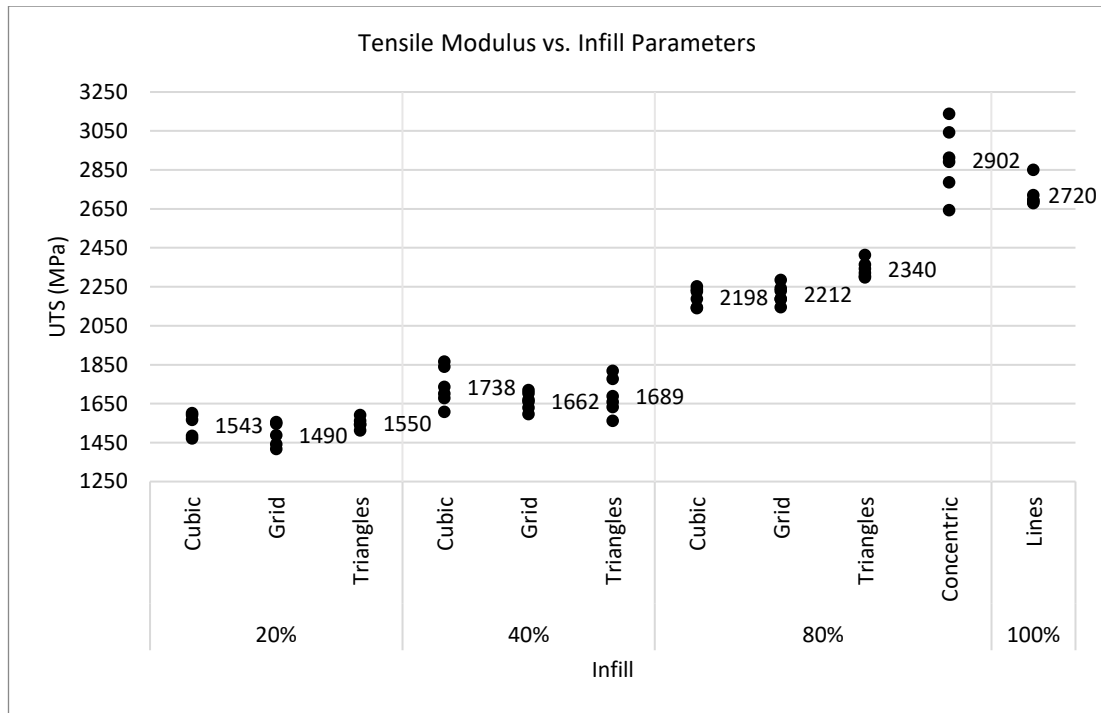


Figure 5.2.4:1 Tensile modulus vs. infill parameters for all plain samples with the mean modulus value displayed. An expected trend of increasing modulus values is seen with increasing infill density. Between cubic, grid and triangle infill, relative values between the 3 remain similar as density increases. Concentric samples show greater values than the other 80% infill patterns but exhibit a greater spread. 100% line infill values show a closer grouping than 80% concentric but are within the lower range of concentric results.

Figure 5.2.4:1 shows tensile modulus values for all plain samples. Expectedly as infill density increases, so too do modulus values. Values are similar between the cubic, grid and triangle infill patterns at each infill density. At 80% density triangle infill exhibits greater modulus values. The concentric infill has a greater tensile modulus value, for all repeats, than the other 80% infill patterns but displays a greater scatter range with a standard deviation of 2.05 MPa. 100% dense sample values are within the lower range of the 80% concentric results but retain a much tighter scatter with 1.39 MPa std. dev. Average modulus values of 80% concentric and 100% infill are 2876 and 2717 MPa, respectively.

Concentric infill in the direction of tensile loading shows the greatest mean value due to loading being applied along the raster length as opposed to at an angle. This leads to stiffness being derived more so from the material properties, as opposed to relying on the bonding quality between layers of the print.

For tensile modulus, it appears that the infill choice between cubic, grid and triangles is less significant than the selected infill density. With higher density resulting in greater values. However, the highest value is derived from concentric infill.

5.2.4.2 UTS

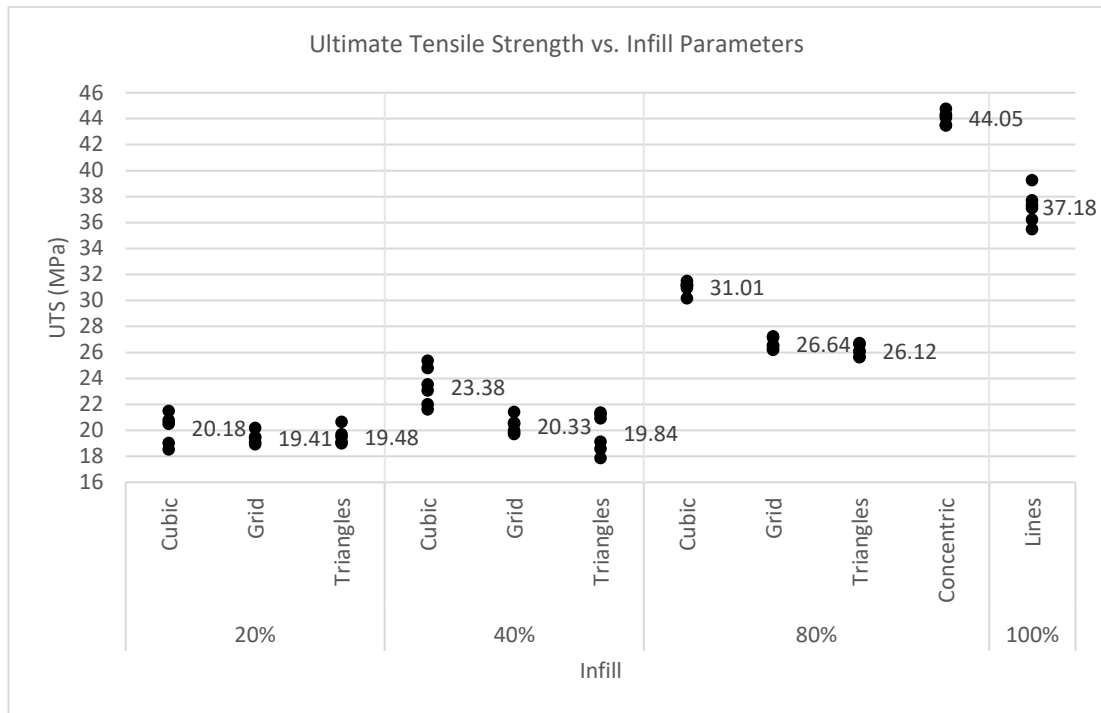


Figure 5.2.4:2 UTS vs. infill parameters for all plain samples with mean values displayed. At 20% infill differences between the 3 infills are small. As infill density increases to 40 and 80%, cubic infill shows a higher value. 80% concentric infill displays a greater UTS than 100% infill density.

Figure 5.2.4:2 shows UTS values for all plain samples. The UTS results show a different trend to modulus. At 20% infill, similar values are observed for all basic patterns. As density is increased to 40 and 80% the cubic pattern displays a higher UTS value than grid or triangles. When comparing grid and triangle patterns at 20, 40 and 80% density there is minor difference in UTS values.

80% concentric displays the greatest values with a mean UTS of 44.0 MPa, above that of 100% infill at 37.2 MPa. Unlike modulus, concentric infill shows a low variance with a std. dev. value of 0.45 MPa vs. the 100% infill std. dev. value of 1.18 MPa.

5.2.4.3 Proof Stress

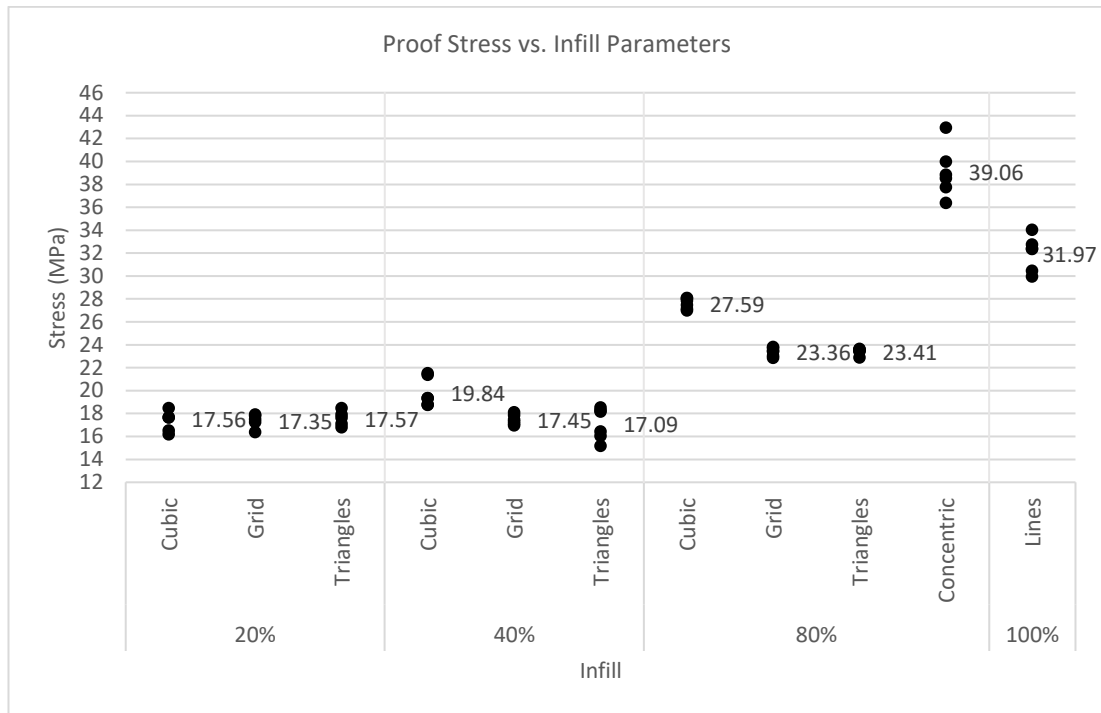


Figure 5.2.4:3 0.2% Proof Stress vs. infill parameters for all plain values with mean values displayed.

Figure 5.2.4:3 displays proof stress value for all plain samples. Proof stress values at 20% infill are similar for the 3 infill patterns. At 40% infill cubic values begin to rise above the grid and triangle infill. At 80% the cubic values are significantly greater than the grid or triangular patterns, which show similar values. Once again concentric infill at 80% shows greater values than 100% infill. However, the scatter of concentric results is greater than others with a standard deviation of 2.05 MPa.

5.2.5 Plain vs. Fibre Samples Direct Comparison

Comparison of samples with no modification other than embedded fibre (samples A1 and A2) vs. plain specimen counterparts (40% triangular infill and 80% concentric infill).

5.2.5.1 Tensile Modulus

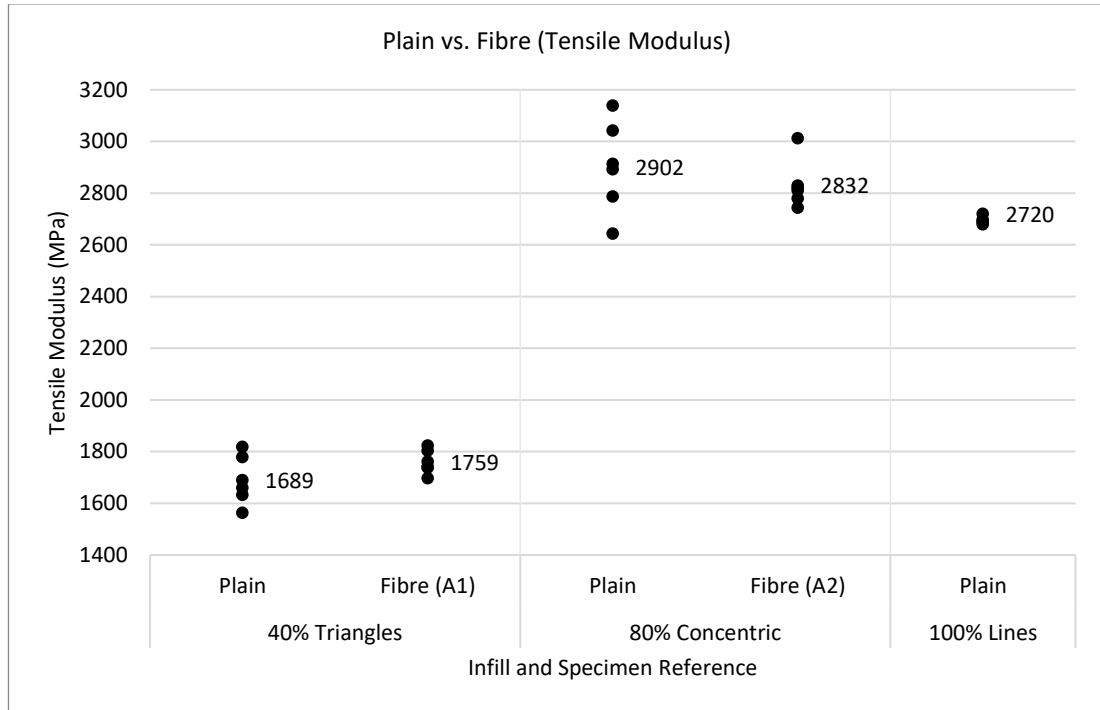


Figure 5.2.5:1 Tensile modulus comparison between plain and fibre samples. Plain 100% density results are included as a reference. The inclusion of an embedded fibre greatly reduces the variation at 40 and 80% infill. However, the plain 100% infill has the lowest std. dev. value of 52.9 MPa.

Figure 5.2.5:1 shows tensile modulus values for fibre samples A1 and A2 compared to their plain counterparts, along with 100% infill. With 40% triangular infill the addition of optical fibre shows to increase the tensile modulus, from 1689 to 1759 MPa (~4%). The scatter range has been closed by increasing of minimum values; the standard deviation value dropped from 86.28 to 42.09 MPa from plain to fibre inclusive, respectively.

At 80% concentric infill the modulus value has decreased by 64 MPa (~-2.4%) with fibre inclusion. Similarly, to 40% infill, the fibre samples have a reduced std. dev. of 85.5 from 153.8 MPa. Both the decrease in modulus value and the observed outlier may be due to the concentric infill pattern displacing the optical fibre as seen in Figure 5.1.2:1.

The 100% infill samples show the smallest scatter range with a std. dev. value of 59.5 MPa. Both the plain and fibre specimens with 80% concentric infill display higher modulus values than the 100% dense plain sample.

5.2.5.2 UTS

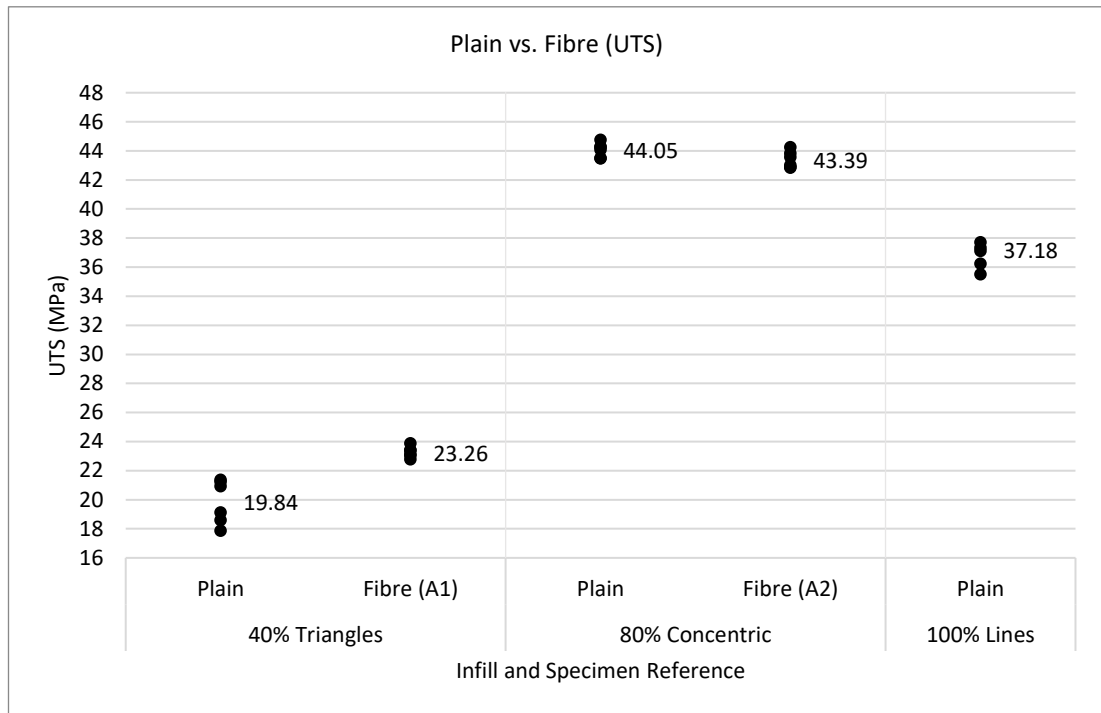


Figure 5.2.5:2 UTS comparison between plain and fibre samples. Mean values are displayed, 100% plain sample set included for reference. Fibre inclusion at 40% triangular infill increases the UTS whereas fibre inclusion with 80% concentric infill reduces UTS by a small margin. Both fibre and plain samples at 80% concentric infill exhibit higher values than 100% plain infill.

Figure 5.2.5:2 shows UTS values for fibre samples A1 and A2 compared to their plain counterparts, as well as 100% infill. The fibre inclusive variation at 40% triangular infill shows both advantageous UTS values and less variation, with a UTS value of 23.3 vs. 19.8 MPa and std. dev. values 0.35 vs. 1.38 MPa for the plain type.

80% concentric infill shows a different outcome, similar to modulus. Both 80% plain and fibre samples show lower std. dev. values than the other specimen types at 0.45 MPa for plain samples and 0.53 MPa for fibre samples. The UTS value drops by a small margin with the addition of fibre, but both 80% samples show significantly higher values than the 100% plain sample set.

5.2.5.3 Proof Stress

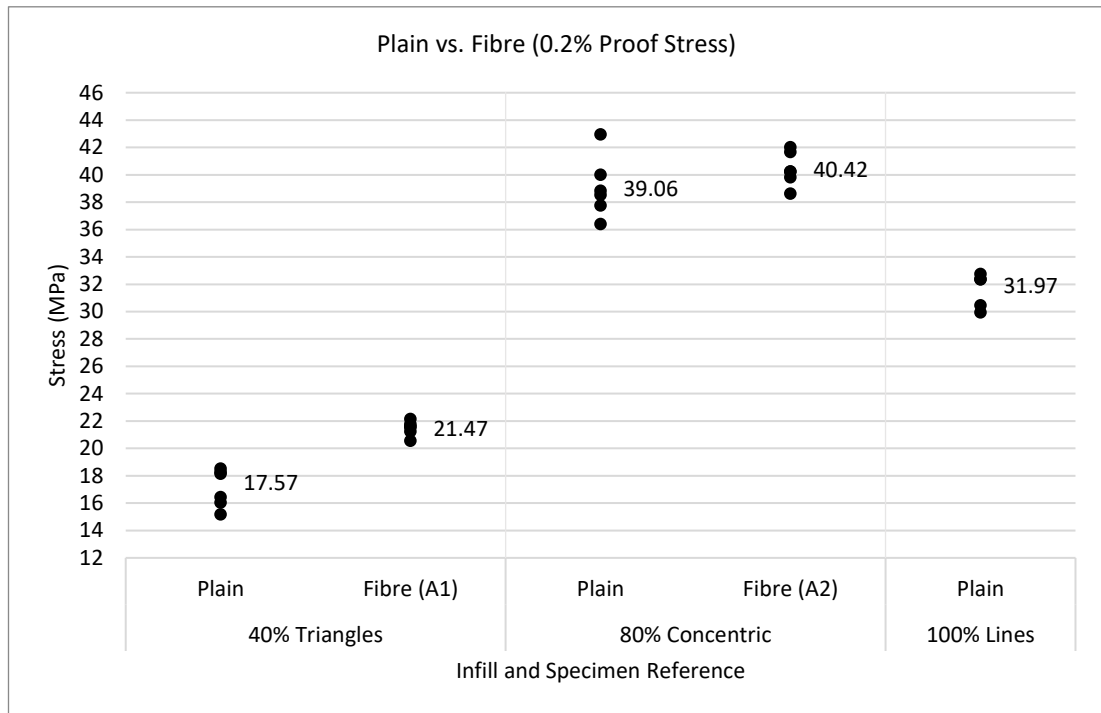


Figure 5.2.5:3 0.2% proof stress direct comparison between plain and fibre samples with mean values. At 40% infill, a similar pattern to UTS is seen. At 80% infill fibre sample A2 shows the reverse to UTS at has slightly greater proof stress than the plain equivalent.

Figure 5.2.5:3 compares proof stress values for fibre samples A1 and A2, their plain counterparts and 100% infill. At 40% triangles infill, the fibre samples show a closer scatter and higher values to the equivalent plain samples, indicating embedded fibre improves variance once more.

At 80% concentric infill the scatter is reduced with the inclusion of fibre, the proof stress value is also increased over the plain sample. Variance is also improved in the fibre sample, but to a lesser degree than at 40% infill.

100% infill shows lower values than plain and fibre samples with 80% concentric infill. The scatter range is small.

5.2.6 Extra Layers

Comparison of 40% plain sample, the fibre equivalent (A1) and samples with additional layers surrounding the fibre.

5.2.6.1 Tensile Modulus

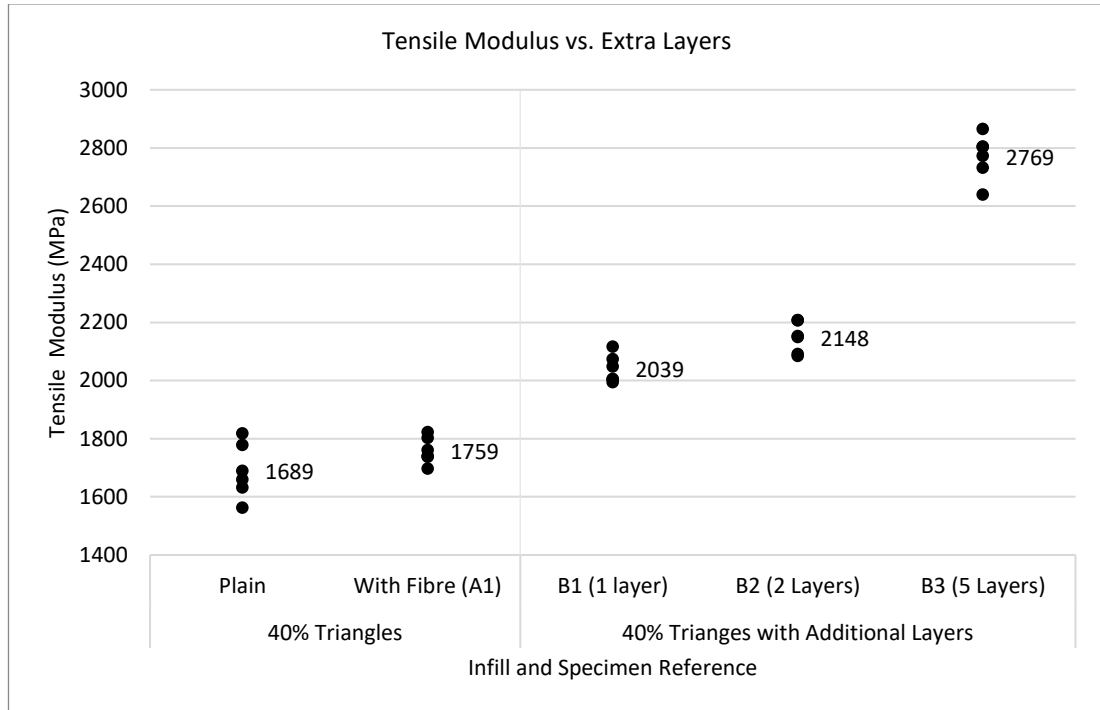


Figure 5.2.6:1 Tensile modulus vs. extra layers. Layers added in B1-3 increase overall specimen density. The addition of a single layer either side of the fibre significantly increases tensile modulus by 15.9%. Doubling the number of additional layers either side of the fibre increases modulus again but by a lesser margin of 5.3%. Increasing the number of layers to 5 either side bumps the modulus by a further 28.9%. At this point, there are only 4 layers of SFI within the specimen.

Figure 5.2.6:1 displays tensile modulus values for fibre samples B1-3 with additional material layers surrounding the fibre. As might be anticipated, adding extra material layers within the sample has increased the tensile modulus of the structure. Adding a single layer of 100% dense lines either side of the fibre (B1) increases the tensile modulus from 1759 to 2039 MPa or by ~16%. 2 layers either side (B2) increases the value by ~22% to 2148 MPa, and 3 layers (B3) by ~57% to 2769 MPa compared to sample A1 with just embedded fibre. Not tested were plain sample equivalents of samples B1-3, therefore, it is difficult to conclude if the modulus increase is purely from additional material or the fibre as well.

However, the variance increases as the number of additional layers do. Fibre inclusion is shown to suggest improvements to variance values. Therefore, it indicates that the fibre contributes to increases in modulus less in the sample B3 than in B2 or B1.

These value increase does not take sample mass or print time into account which can both be critical design factors. Mass and modulus values are considered further in Section 5.2.8.

5.2.6.2 UTS

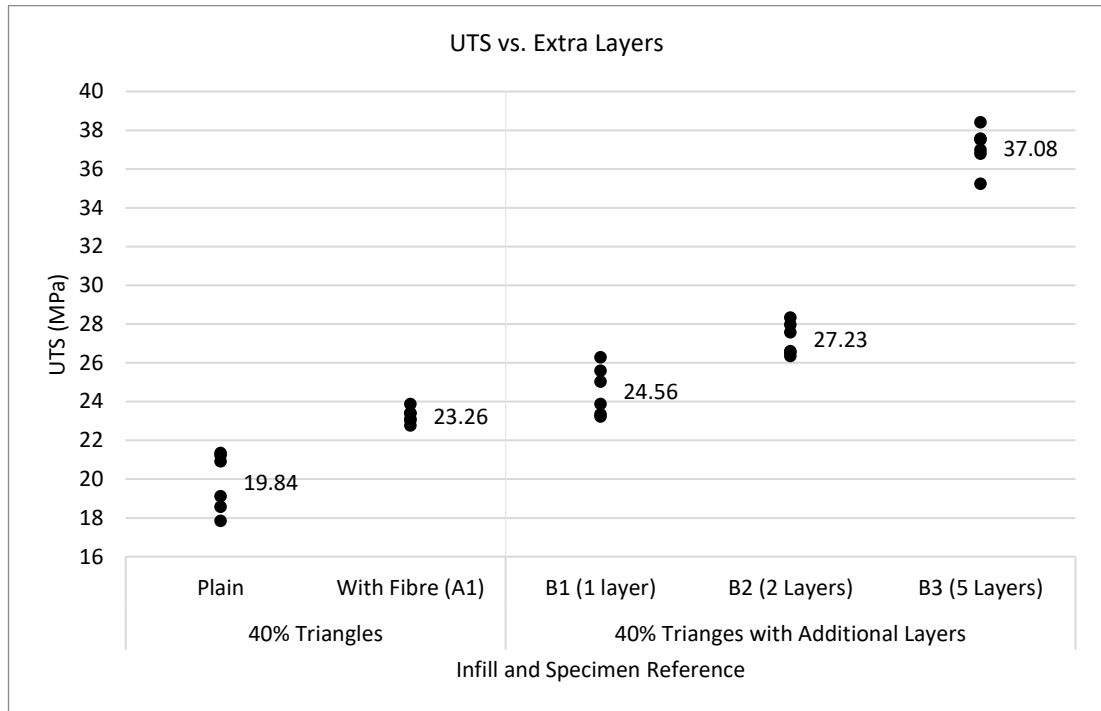


Figure 5.2.6:2 Comparison of UTS when extra solid layers are introduced surrounding the fibre. This does not consider the associated mass or print time gain. The plain sample is present as a reference, it is difficult to directly compare with samples B1-3, which have both extra layers and embedded fibre.

Figure 5.2.6:2 depicts samples B1-3 UTS values, along with sample A1 and its plain equivalent. The UTS rises as the number of fibre surrounding solid layers increases, similarly to the tensile modulus. A single 100% density layer either side of the fibre (B1) increases the UTS by ~6% over the SFI fibre sample (A1), but the std. dev. value decreases to 1.15 from 0.35 MPa. Doubling the number of layers either side of the fibre to 2 increases the mean UTS by ~16%. Increasing the layers to 5 (10 total full density layers) increases it by ~59% vs. sample A1.

5.2.6.3 Proof Stress

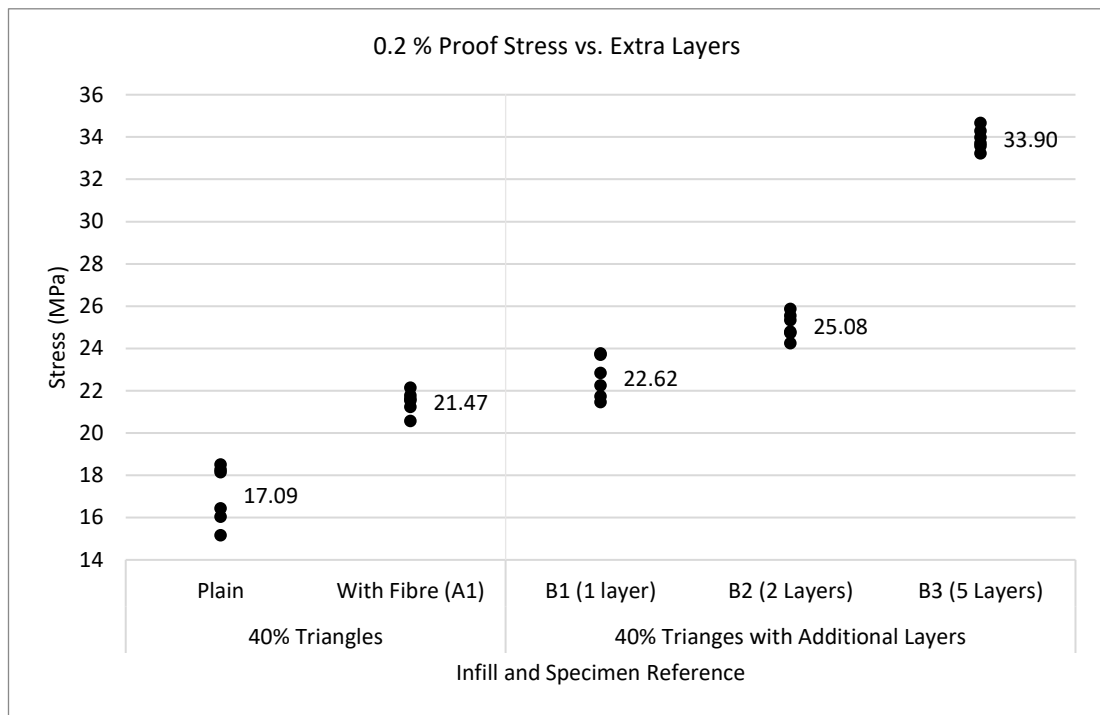


Figure 5.2.6:3 Proof stress vs. extra layers. As the number of extra layers increases so too does the proof stress.

Proof stress values for samples B1-3 with sample A1 and 40% triangles infill samples shown in Figure 5.2.6:3. As with UTS, the proof stress increases as additional layers are added. The addition of fibre alone increases the proof stress by ~25% over the plain sample. 1 extra layer either side of the fibre by ~32%, 2 layers by ~47% and 5 layers by ~98%.

Increased mass is also associated with further added layers. However, the addition of just the fibre has a 25% proof increase with ~1% mass increase.

Sample mass properties are further considered in Section 5.2.8.

5.2.6.4 Tensile Modulus, B1-3 vs. concentric and 100% infill

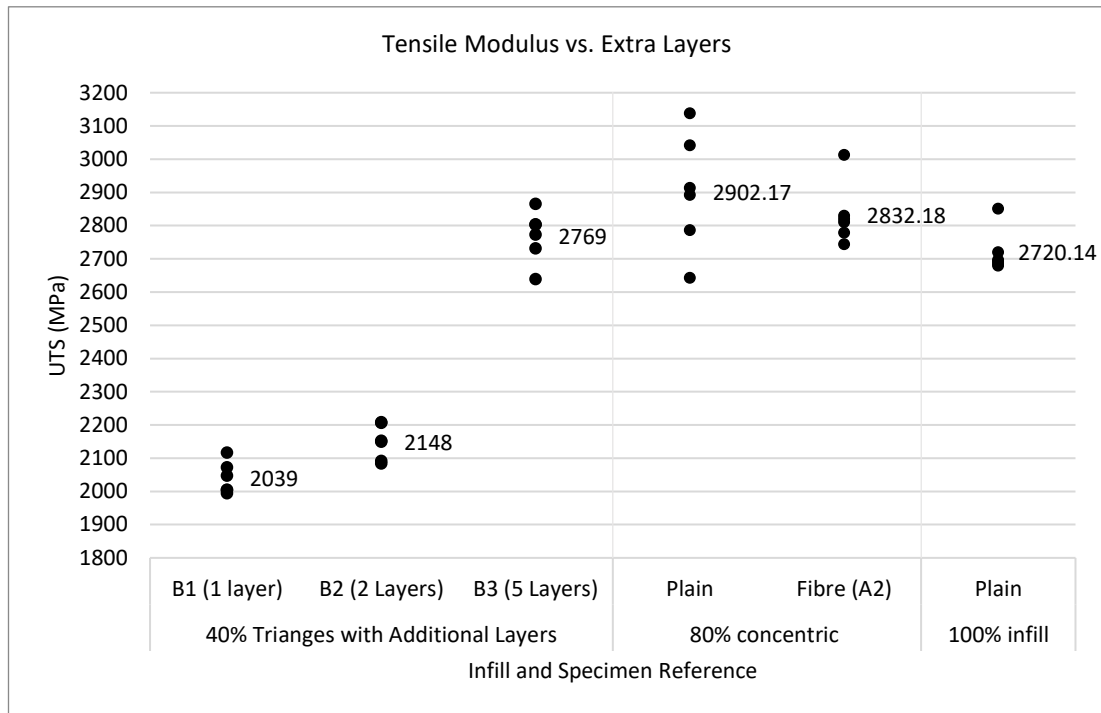


Figure 5.2.6:4 Comparison of tensile modulus values of samples with additional layers (B1-3), plain and fibre samples with 80% concentric infill and plain samples at 100% infill. Mean values are shown. Both plain and fibre samples with 80% concentric infill have higher modulus values than B3. However, B3's modulus is greater than the plain 100% infill sample.

Figure 5.2.6:4 shows modulus values of samples B1-3 compared to those of 80% concentric infill samples with and without fibre, and to 100% infill. 10 additional layers within the structure of B3 brings modulus values close to those of 80% concentric infill, but notably exceeds that of 100% infill density. However, it must be remembered that tensile samples are made up of 20, 0.2mm layers with 3 top and bottom layers resulting in only 4 layers within the structure being SFI.

5.2.7 Fibre Direction

5.2.7.1 Modulus

Figure 5.2.7:1 shows tensile modulus values as a function of fibre direction within the sample and compared to the plain sample type.

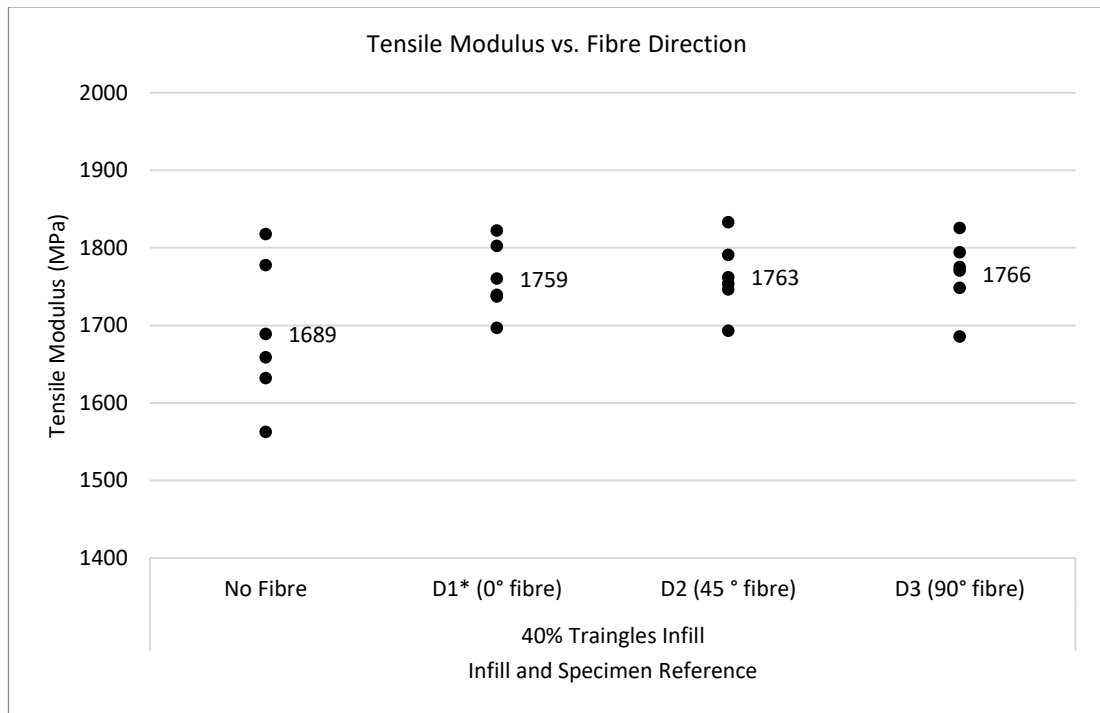


Figure 5.2.7:1 Comparison of tensile modulus values with fibre rotation in increments of 45°. The direction of the fibre is shown to have little to no impact on the modulus. However, the inclusion of fibre in all samples reduces the variance compared to plain samples.

The direction of the fibre within the sample appears to have minimal impact on tensile modulus values. Each fibre specimen has similar values and ranges. Std. Dev. values for D1-3 are 42.1, 42.7 and 43.3 MPa, respectively.

All 3 fibre samples have greater modulus values than the plain sample and reduced variance, std. dev. of 86.3 MPa for the plain sample. This indicates that the addition of an optical fibre at any orientation in a single plane within a structure has no detrimental impact on tensile modulus and improves variance.

5.2.7.2 UTS

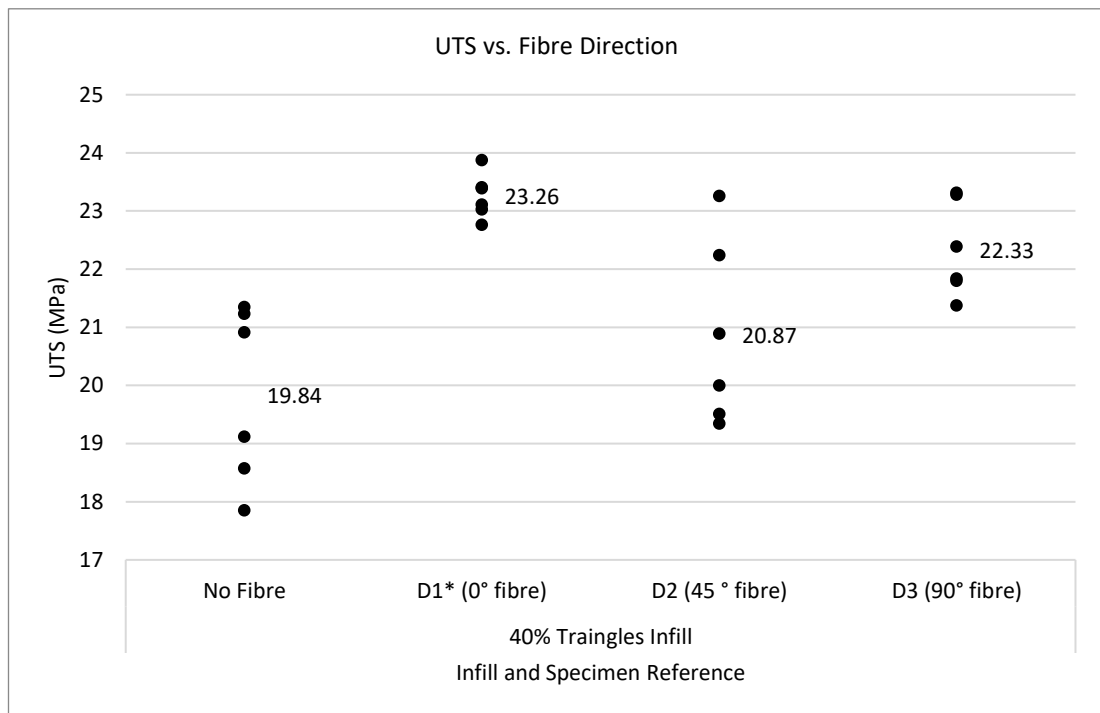


Figure 5.2.7:2 UTS vs. fibre direction. Each of the fibre sample types has larger UTS values than the plain samples. The fibre at 0° (in line with tension) shows the greatest value and smallest variance.

UTS values show as a function of fibre direction show (Figure 5.2.7:2) a different trend. All fibre samples have greater mean values at 23.3, 20.9 and 22.3 MPa, for D1, D2 and D3, respectively, compared to 19.8 MPa for the plain sample. However, sample D1 with the fibre axial with the tensile load shows the highest values and smallest std. dev.

The sample with fibre at 45° to the tensile load shows the greatest variability and lowest mean UTS of the fibre samples. This may be due to the embedding and overprinting process when using a triangular infill with some of the raster lines at 45°. i.e. some of the raster lines are axial to the fibre possibly leading to the nozzle moving the fibre to a greater extent as seen in the micro-CT images for concentric and 0° infill (Figure 5.1.2:1 and Figure 5.1.4:1).

5.2.7.3 Proof Stress

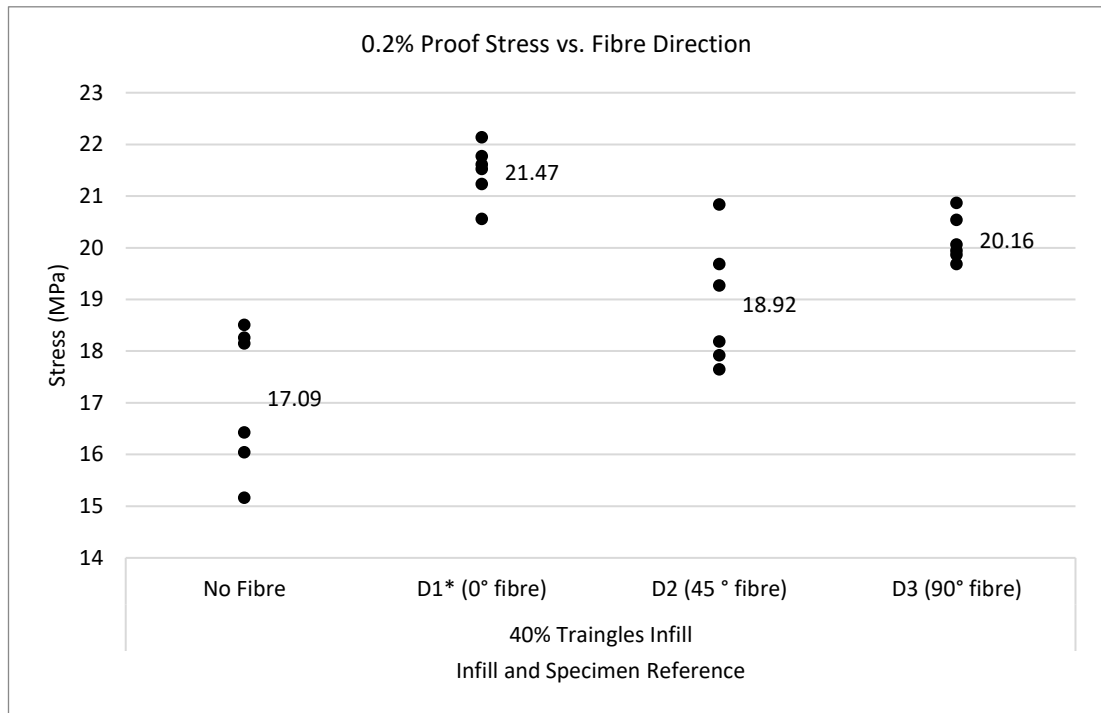


Figure 5.2.7:3 0.2% proof stress vs. embedded fibre direction. 0° represents fibre axial to the tensile load and 90° being perpendicular to tensile loading. All fibre samples have greater proof stress values than the plain sample with D1 having the greatest value. Surprisingly the 45° fibre shows a lower proof stress value than the fibre perpendicular fibre.

Proof stress values as a function of fibre direction are shown in Figure 5.2.7:3. The plain sample exhibits the lowest proof stress value of 17.09 MPa. Each of the fibre inclusive samples (D1-3) have values of 21.47, 18.92 and 20.16 MPa, respectively. Sample D1 with the fibre running parallel to the tensile load direction shows the greatest value, ~26% greater than the plain sample. Surprisingly the 45° fibre results in a lower proof stress value than the fibre at 90° to the load. The 45° fibre also shows the greatest std. dev. at 1.12 MPa. However, this is exceeded by the plain sample at 1.27 MPa suggesting the inclusion of fibre in any orientation increases the proof stress and reduces variance.

Further research could investigate if the lower values are associated with a 45° fibre purely due to the fibre angle, or if there is a relation between the fibre angle and the raster angles of the chosen infill pattern.

5.2.8 Tensile Mass Modulus Ratios

Increased infill of samples expectedly leads to a rise in tensile modulus. However, the mass also increases with infill density. The Tensile Mass-Modulus ratio (MMR_T) is an attempt to consider the modulus value as a function of mass. The MMR_T has been calculated by dividing the tensile modulus (MPa) by the mean sample mass (g). This value indicates the material efficiency in terms of tensile modulus, with higher values being favourable. Table 5.2.8-1 shows values of the mass modulus ratio for all samples. These values are displayed graphically in Figure 5.2.8:1.

Table 5.2.8-1 Tensile mass modulus ratio values for plain and fibre samples.

Infill Parameters		Mass (g)	Tensile modulus (MPa)	Tensile Mass Modulus Ratio (MPa/g)	
Plain	20%	Cubic	5.55	1550	279
		Grid	5.62	1522	271
		Triangles	5.67	1581	279
	40%	Cubic	6.75	1750	259
		Grid	6.85	1680	245
		Triangles	6.77	1696	251
	80%	Cubic	8.57	2194	256
		Grid	9.33	2212	237
		Triangles	9.18	2337	254
		Concentric	9.25	2876	311
100%	Lines	9.77	2717	278	
Fibre	40% Triangles	A1	6.85	1759	257
	80% Concentric	A2	9.40	2832	301
	Extra Layers	B1	7.78	2039	262
		B2	7.90	2148	272
		B3	9.17	2769	302
	Fibre Direction	D1	6.85	1759	257
		D2	6.87	1763	257
		D3	6.92	1766	255

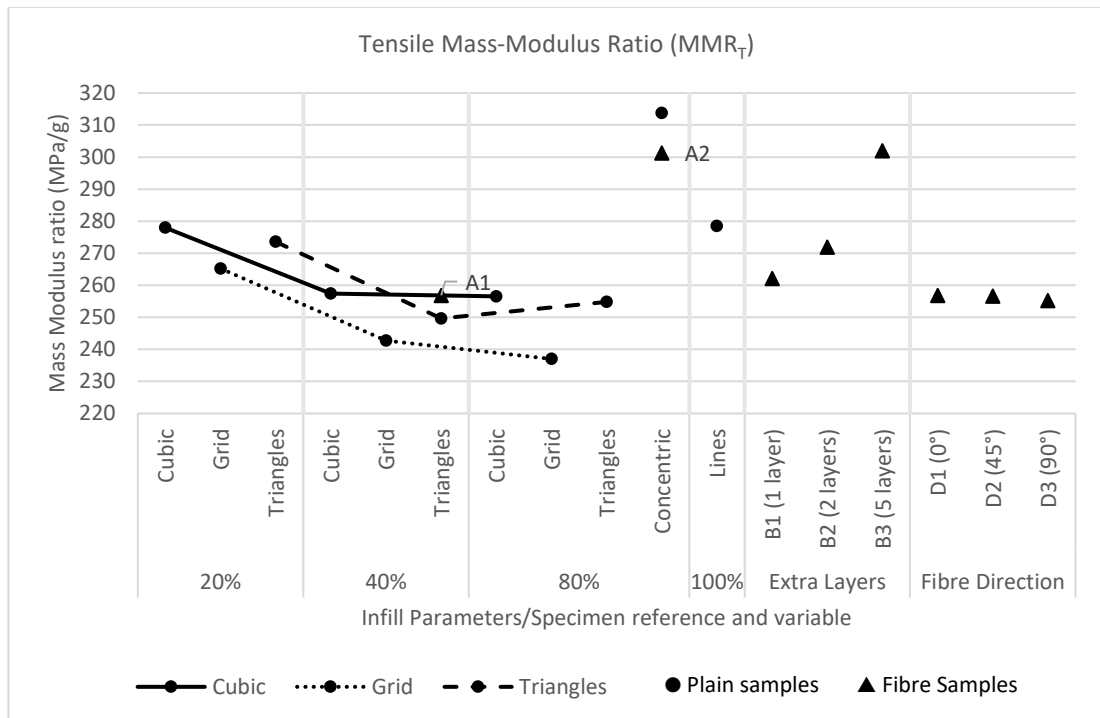


Figure 5.2.8:1 Tensile mass modulus ratios for plain and fibre samples. This gives an indication of material efficiency in terms of tensile modulus. Circles represent plain samples, while triangles show fibre samples. Samples A1 and A2 are plotted and labelled in their plain sample counterpart column. Lines connect plain samples of equal infill pattern to visualise the ratio change with an increase in infill density.

Circles represent plain samples, whilst triangles represent fibre samples. Samples A1 and A2 (labelled) are positioned in the columns of their corresponding non-fibre equivalents. Lines connect plain samples with the same infill pattern to better visualise trends as the infill density increases.

Plain samples with cubic, grid and triangular infill show a general downward trend in MMR_T as infill density increases. The exception to this is the 80% triangular infill, with MMR_T increasing from 250 to 255 MPa/g from 40 to 80% density. Cubic infill offers the most effective and grid the least effective use of material at 20, 40 and 80% density when comparing the cubic, grid and triangle infill patterns.

100% infill offers a similar material efficiency as 20% dense cubic and triangular infill. The most efficient plain infill is 80% concentric, even when considering fibre samples.

Comparison of samples A1 and A2 to their plain counterparts show mixed results. In the instance of 40% triangular infill (A1), the MMR_T is improved by ~4% with the addition of fibre but at 80% concentric (A2) the value is decreased by 2% with fibre addition. In both instances, the fibre contributes to a small increase in mass: 1.18% and 1.62% for A1 and A2, respectively, over their plain counterparts.

Samples B1, B2 and B3 with 2, 4 and 10 extra material layers, respectively, show a rising increase in MMR_T values. Indicating a combination of low- and high-density regions may be a mass efficient way to improve the tensile strength of a structure. The direction of fibre within the sample appears to have little to no impact on the MMR_T value, as shown by samples D1-3 with values like that of the plain 40% triangle sample.

5.2.9 Tensile Summary

- Several plain samples tensile modulus calculations were modified to avoid non-linear portions of the stress-strain curve. The cause for this was not investigated but it did not occur in any fibre samples. Further investigation may reveal if this was mitigated by the inclusion of fibre or is simply a coincidence.
- An 80% dense concentric infill shows better tensile properties than 100% infill. This is likely true at other infill densities but was not tested.
- The inclusion of fibre at 40% infill improves all presented tensile properties and reduces variance. Fibre addition at 80% reduces modulus and UTS values by a small margin and increases proof stress, also by a small amount. Variance is improved except with UTS values.
- Addition of material surrounding the fibre expectedly improves tensile properties. The extent of the improvement due to the fibre or the added material cannot be determined as plain equivalent samples for B1-3 were not tested.
- Additional material increased variance in all instances but one (proof stress, B3) when compared to sample A1.
- Sample B3 with 10 total additional layers displayed a greater tensile modulus than 100% plain infill.
- Fibre direction has no detrimental impact on tensile modulus. The inclusion of fibre in any direction reduces variability and increases modulus.
- Fibre direction was more critical when considering UTS and proof stress. 45° fibre still increased values but to a lesser extent than 0° and 90°. Fibre at 0° (axial to tensile loading) showed the greatest improvement. There may be a relation between fibre direction and infill pattern, but this was not explored further.
- In terms of material efficiency and tensile modulus, cubic infill is the most effective and grid the least. Increasing the infill density from 20% to 40% causes a drop in efficiency, increasing from 40% to 80% results in similar values.
- At 40%, fibre addition improves material efficiency, at 80% reduces it.
- Increasing additional material layers drastically improves material efficiency.

5.3 Flexural Results

5.3.1 Dimension Results

All plain and fibre inclusive samples were within the required tolerances.

5.3.2 Manufacturing Discrepancies

Flexural samples A1, A2 and D1-3 were fabricated in two sets of 3^f. However, these were done a significant time apart. This has resulted in two distinct groups of results, with the second set displaying improved properties. This is likely due to improved familiarity with the manual fibre embedding procedure. These separate sets lead to difficulty in comparing results in some instances and have been mentioned. This highlights the importance of having a robust fabrication process and the impacts of the quality of the fibre embedding.

5.3.3 Flexural Modulus Calculation Correction

Calculation of the flexural modulus within the requested bounds was not possible for all samples due to inconsistencies. Flexural strain values of 0.0005 and 0.0025 are specified by ISO 178. For samples showing nonlinear portions within this range, the modulus calculation region was moved. Similarly, to the method outlined for tensile modulus calculation, the SLOPE function bounds were moved just beyond the anomaly, maintaining the same range size, and remaining within the linear portion of the curve. Figure 5.3.3:1 below shows a stress-strain plot for a plain 40% triangle infill sample. Vertical dashed lines represent the requested modulus calculation range which encompasses an anomaly. Appendix E – Flexural Modulus Correction lists the samples with modification, along with modulus values before and after the adjustment. This modification was only required for plain samples, indicating that fibre inclusion may prevent this stress dip from occurring.

^f Samples A1 and D1 are equal.

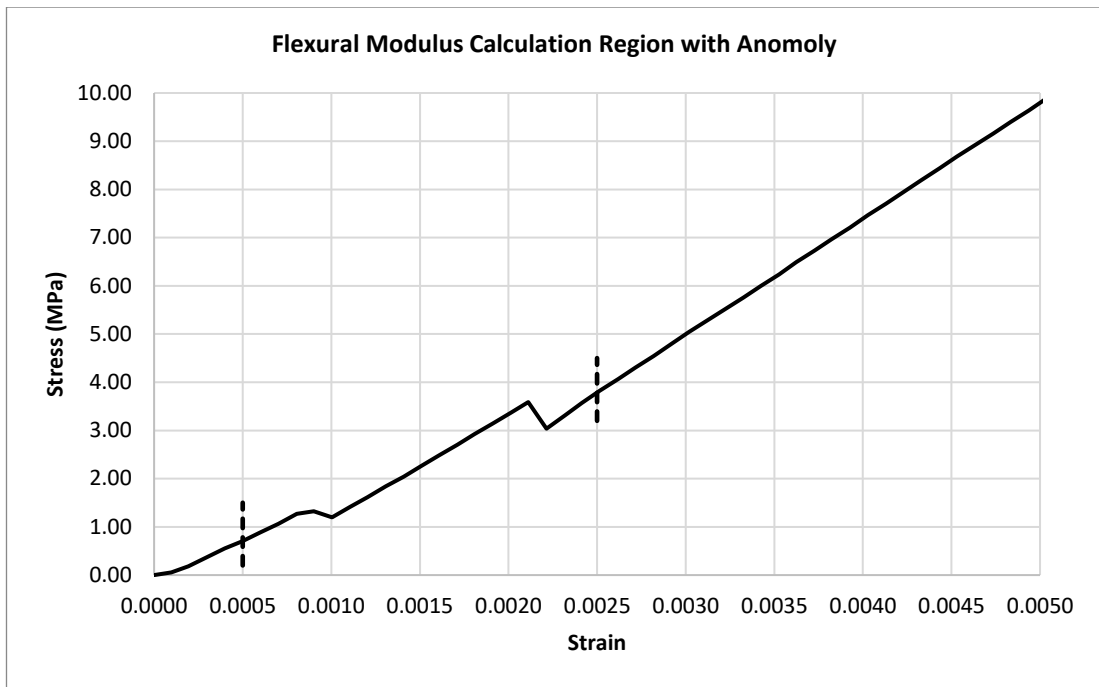


Figure 5.3.3:1 Stress-strain plot for a plain 40% triangle flexural specimen. The vertical dashed lines mark the requested flexural modulus calculation region between 0.0005 and 0.0025 strain. However, this portion is non-linear and would lead to flawed results. This calculation region is therefore moved to avoid the anomaly whilst maintaining the same range size.

5.3.4 Tabulated Values

Mean calculated values for flexural sample types are displayed in the following tables, **Error! Reference source not found.** for plain and Table 5.3.4-2 for fibre samples.

Table 5.3.4-1 Flexural results for plain samples

Plain Samples								
Infill Percentage	Infill pattern	Mass (g)	Flexural Modulus (MPa)	Std. Dev (MPa)	Flexural Strength (MPa)	Std.Dev (MPa)	Flexural Strain at Max Stress	Std.Dev
20	Cubic	2.17	2176	25.76	51.00	0.27	0.02981	0.00039
	Grid	2.17	2259	30.60	53.83	0.45	0.03246	0.00042
	Triangles	2.30	2130	54.68	52.23	1.11	0.02887	0.00052
40	Cubic	2.80	2329	55.15	59.10	1.19	0.03442	0.00078
	Grid	2.77	2305	70.91	57.13	0.69	0.03526	0.00066
	Triangles	2.77	2305	154.72	59.91	0.98	0.03509	0.00045
80	Cubic	3.60	2580	47.87	65.90	0.84	0.03656	0.00053
	Grid	3.55	2538	52.75	57.83	1.53	0.03471	0.00097
	Triangles	3.58	2481	51.49	62.45	1.01	0.03464	0.00057
	Concentric	3.63	2768	119.74	80.86	0.39	0.04154	0.00041
100	Lines	4.00	2774	50.11	81.79	1.91	0.03977	0.00068

Table 5.3.4-2 Flexural results for fibre samples.

Fibre Samples							
Sample	Mass (g)	Flexural Modulus (MPa)	Std. Dev.	Flexural Strength (MPa)	Std. Dev.	Flexural Strain at Max Stress	Std. Dev
A1	2.70	2353	164.27	57	4.80	0.03568	0.00354
A2	3.48	2937	133.40	84	1.59	0.04186	0.00075
B1	3.15	2532	17.27	64	0.37	0.03333	0.00039
B2	3.30	2318	20.87	60	0.50	0.03555	0.00059
B3	3.77	2774	25.88	76	1.31	0.03949	0.00040
D2	2.67	2281	47.34	58	2.07	0.03395	0.00213
D3	2.68	2387	103.13	60	1.54	0.03349	0.00081

5.3.5 Plain Samples

Samples excluding fibres are compared in the following segment. Figure 5.3.5:1 shows flexural modulus values for each sample type. Individual sample results are plotted, and the mean is displayed.

5.3.5.1 Flexural modulus

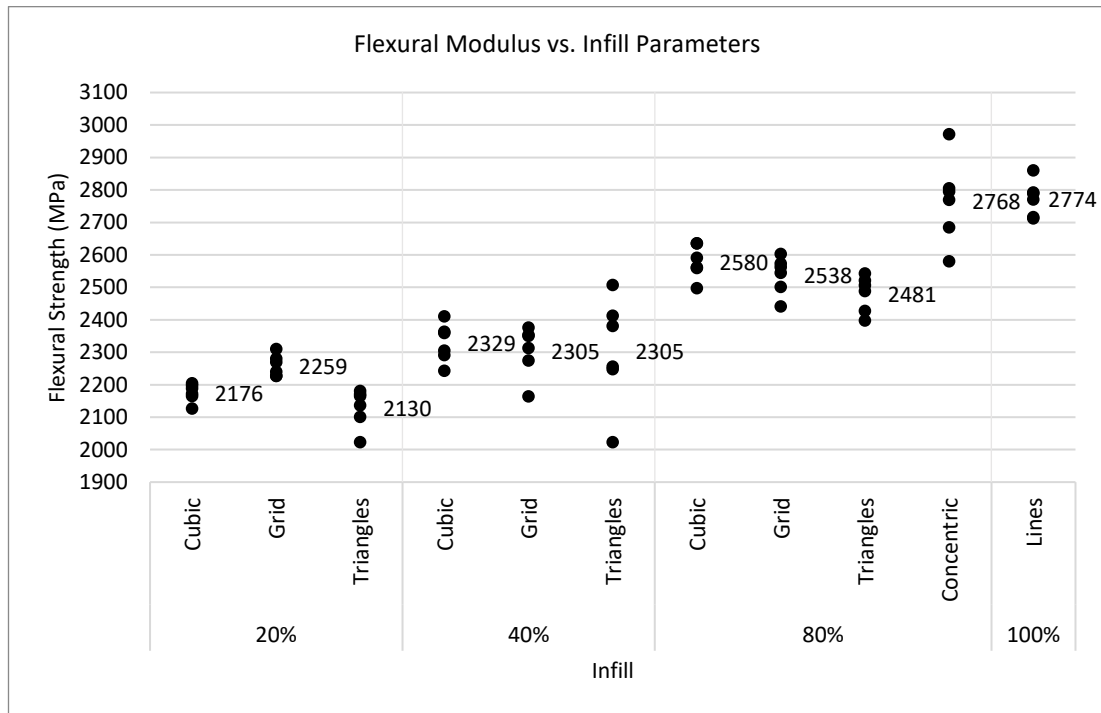


Figure 5.3.5:1 Flexural modulus of all plain samples. As infill density so too does modulus values with the highest exhibited by 100% infill. At 20% grid has the highest value, for 40 and 80% cubic has the largest flexural modulus, not considering concentric. 80% concentric infill has a modulus 6 MPa lower than the fully dense specimen.

Figure 5.3.5:1 shows a trend of increasing flexural modulus with increasing infill density. At 20% density grid infill exhibits a greater value over cubic and triangle infills, with triangles showing the lowest value. Increasing infill density to 40%, cubic infill shows the highest modulus and lowest variance. Both grid and triangle infill have equal mean values, however, grid displays a std. dev. of 70.91 MPa where triangles have a std. dev value of 154.72 MPa. At 80% infill cubic once again has the highest modulus value and lowest variance, with triangles having the lowest modulus.

80% concentric infill has ~7% greater modulus value over 80% cubic infill but has a std. dev. value 150% larger than cubic at 119.74 MPa. Comparison of 80% concentric with 100% density shows similar modulus values, with full density having a lower std. dev of 50.11 MPa.

5.3.5.2 Flexural strength

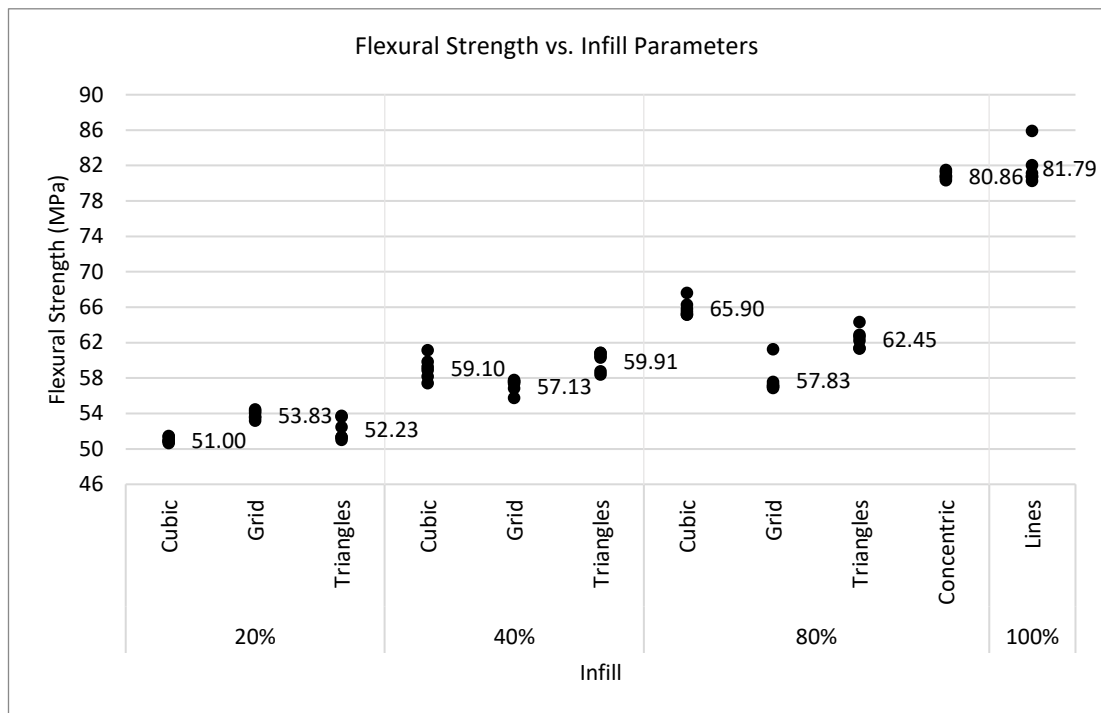


Figure 5.3.5:2 Flexural strength values for plain samples. Grid shows the highest flexural strength at 20% infill density but the lowest at 40% and 80% density. At 80% grid infill displays a value only 0.7 MPa greater than the same pattern at 40% density and below that of cubic or triangle infill at 40%. Concentric infill at 80% density shows a strength value almost equal to the 100% infill sample.

Figure 5.3.5:2 Flexural strength values for plain samples how flexural strength values for all plain samples. At 20% infill value grid displays the highest strength and cubic the lowest. At 40% infill this is almost reversed, with grid exhibiting the lowest strength and triangles the greatest by 0.81 MPa. Cubic infill at 80% has the highest strength and grid the lowest once more. Cubic also has the lowest variance and grid the greatest. Notably, 80% grid infill's mean strength value is less than that of 40% cubic and triangle infill and is only ~1% greater than the half as dense 40% grid samples.

80% concentric infill has a strength value of nearly 15 MPa greater than cubic infill of the same density. It also has the second-lowest deviation with a std. dev. value of 0.39 MPa, beaten only by 20% cubic with a std. dev. of 0.27 MPa.

100% infill density has the highest flexural strength value, larger than concentric by ~1%, but has a higher deviation, with std. dev. value of 1.91 MPa vs. 0.39 MPa of concentric infill.

5.3.6 Plain vs. Fibre Samples

Fibre samples A1 and A2 are compared to their plain counterparts. 100% infill is also included for comparison. Figure 5.3.6:1 Flexural modulus comparison of equal samples with and without fibre shows flexural modulus values and Figure 5.3.6:2 displays flexural strength values.

5.3.6.1 Flexural Modulus

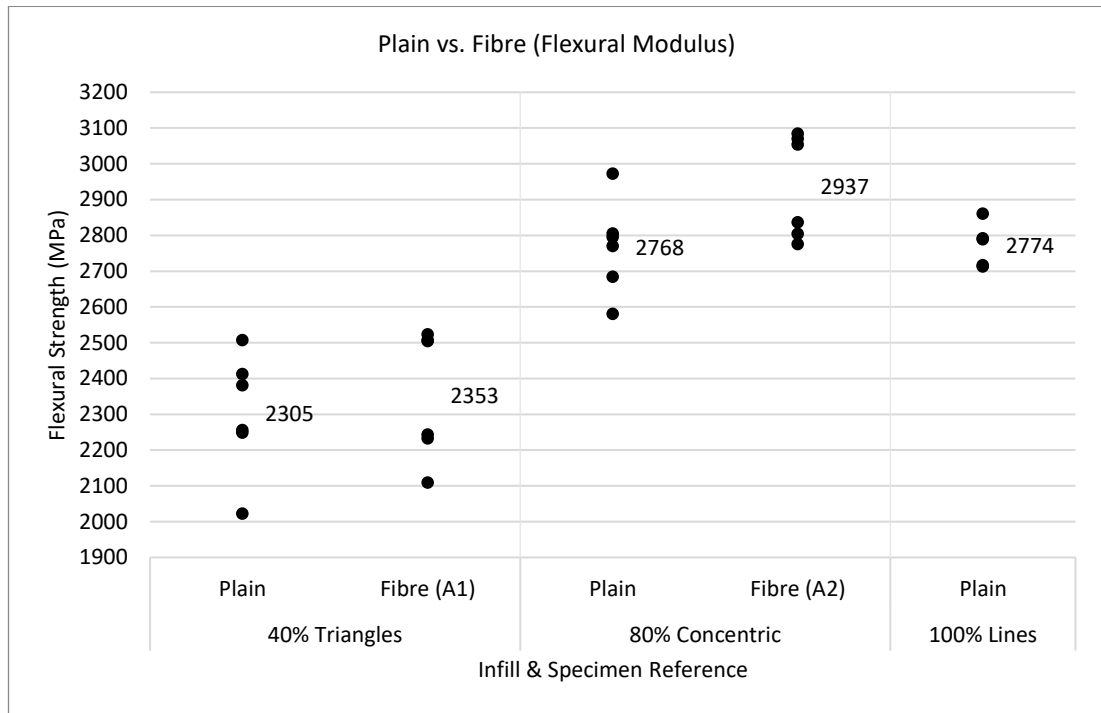


Figure 5.3.6:1 Flexural modulus comparison of equal samples with and without fibre. 100% density is also included. The difference in results of the first and second set of fibre samples is distinct, with the second set showing the higher values.

40% infill shows a similar modulus value for the plain and fibre sample. However, the second set of fibre specimens show values at and above the highest plain sample values indicating the importance and impact of the fibre laying technique. The same split is seen at 80% infill between plain and fibre samples, with the second fibre set having a 6% modulus improvement over plain.

100% plain infill shows modulus values below that of A2 and shows the lowest standard deviation value of 50.11 MPa, again likely due to the 2 separately manufactured fibre sets.

5.3.6.2 Flexural Strength

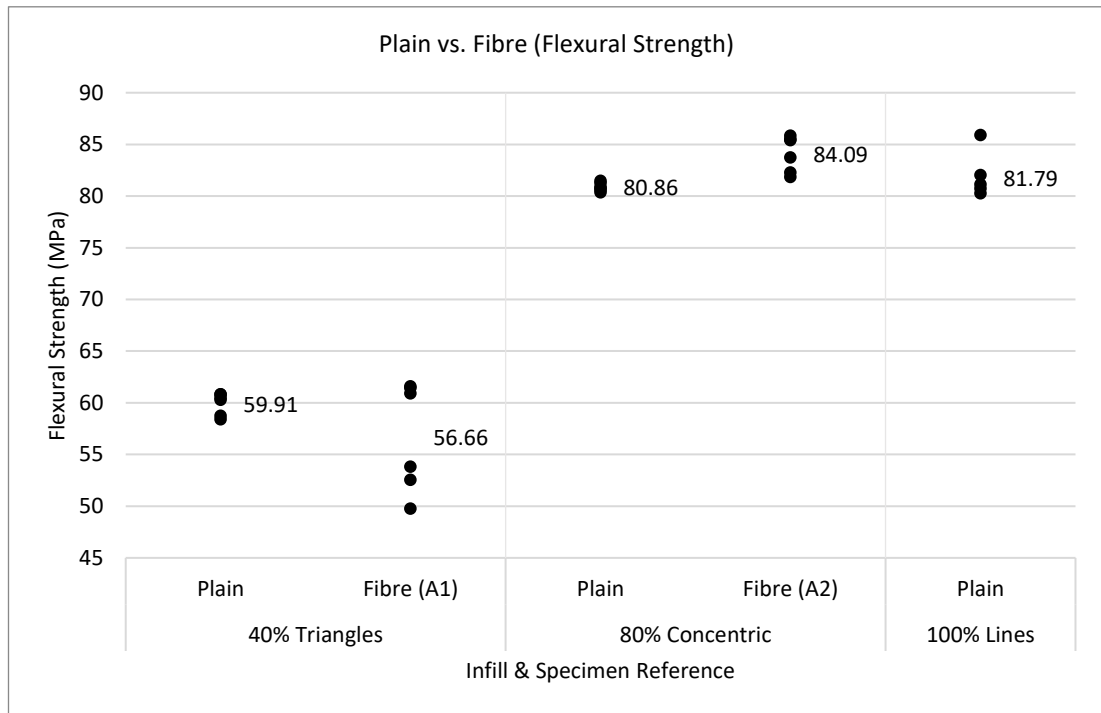


Figure 5.3.6:2 Flexural strength values of plain and fibre equivalent samples. 100% infill is also included.

At 40% infill, plain shows 5.4% higher flexural strength than the fibre equivalent. The split between the fibre sample set shows that poorly embedded fibre may be detrimental to the flexural strength, whereas the second set of 3 fibre samples show strength values around the top end of the 40% plain set.

Moving to 80% infill the fibre sample shows a 3.23 MPa increase in flexural strength. The split between the two fibre sets is less defined, this is highlighted as it has a lower std. dev. value of 1.59 MPa than 100% infill std. dev. value of 1.91 MPa. This indicates that, at a higher infill percentage, fibre placement becomes a less critical factor when considering flexural strength.

100% infill density displays strength values in between the plain and fibre containing 80% concentric samples.

5.3.7 Extra Layers

Flexural modulus (Figure 5.3.7:1) and flexural strength (Figure 5.3.7:2) are compared for samples with additional layers surrounding the fibre.

5.3.7.1 Flexural Modulus

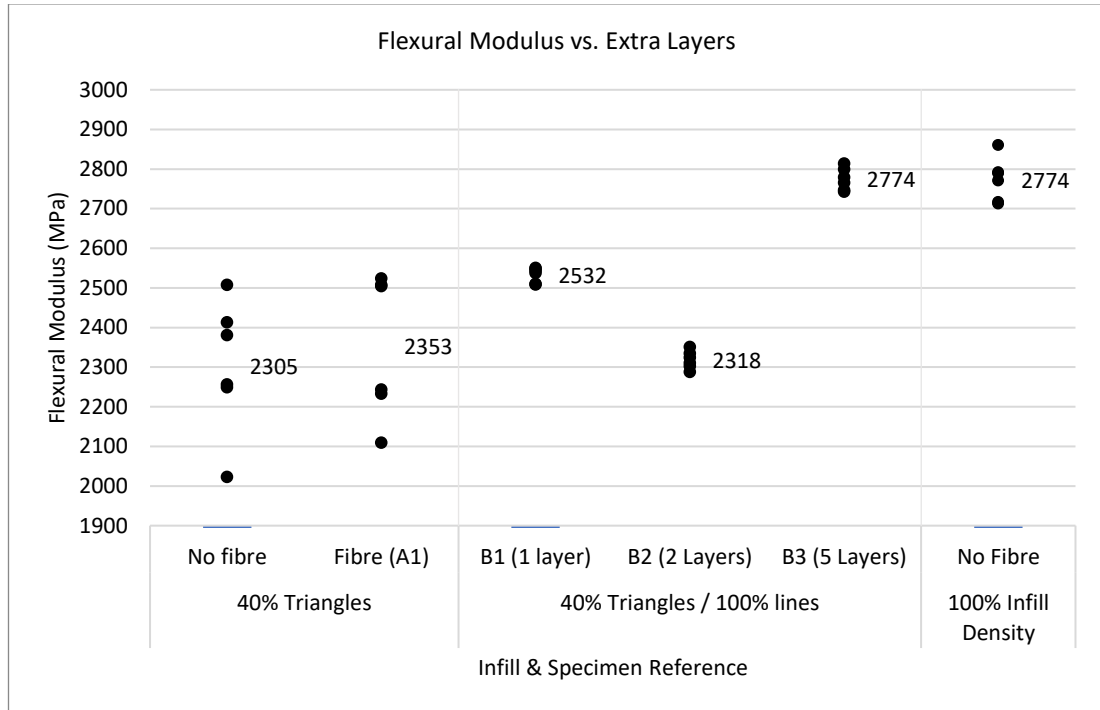


Figure 5.3.7:1 Flexural modulus vs. additional layers. Samples B1-3 were manufactured as a single set of 6. Surprisingly sample B2 shows a lower flexural modulus than sample B1.

Samples B1-3 were manufactured as a single set of 6. The addition of a layer either side of the fibre (B1) shows an expected improvement in flexural modulus vs. sample A1. However, the second set of A1 samples show values similar to that of B1. Unexpectedly sample B2 with 2 additional layers either side of the fibre has an 8% lower flexural modulus than B1. This may offer cause to suggest a manufacturing error for B2 samples. Sample B3 has a more anticipated, and higher, modulus value.

When 10 total extra layers surround the fibre modulus values match that of the 100% plain sample type. The deviation of sample B3 is lower at 1.31 MPa vs. 1.91 MPa of the 100% sample. This indicates that increasing sample density reaches a point where extra material may not increase flexural modulus any further. Or that the fibre has increased the value up to that of a full density sample. Another option suggested is that the fibre has no impact on the modulus value but Improves the variance.

Either way, the impact of the fibre in sample B3 cannot be fully judged as no plain equivalent was tested, nor was a sample with 100% density and embedded fibre.

5.3.7.2 Flexural Strength

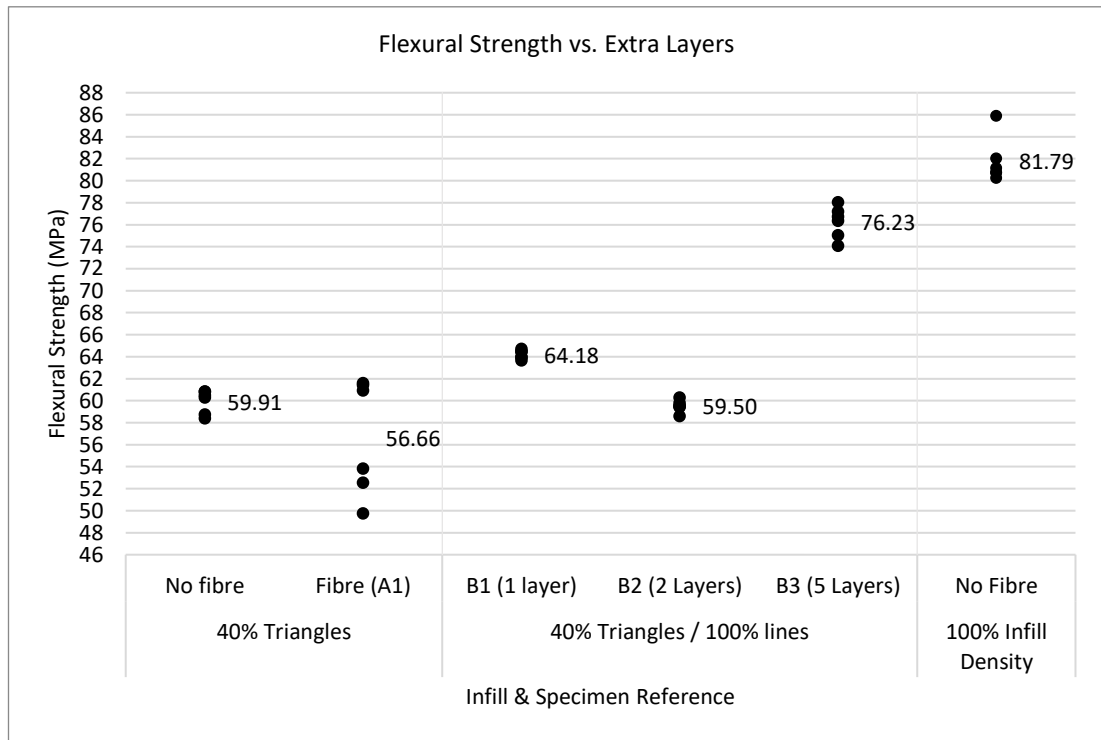


Figure 5.3.7:2 Flexural strength vs. additional 100% infill layers either side of the encapsulated fibre. Strength values for sample B2 with 4 total additional layers are similar to that of the 40% infill plain sample and less than that of sample B1 with 2 additional layers. 5 additional layers either side of the fibre (B3) do not match values displayed by plain 100% infill.

Sample B1 shows the addition of a 100% infill layer either side of the fibre increases the flexural strength over A1 by ~13%. As with modulus, increasing this to 2 layers unintuitively reduces the strength to similar values found in the plain 40% infill sample. This does not coincide with expected behaviour as the samples B1-3 in tensile samples represented increasing values for all properties. B3 returns to the expected trend with a 34.5% larger flexural strength over sample A1.

100% infill plain samples exhibit the highest strength values at 81.79 MPa. Even though sample B3 only has 4 layers of 40% triangular infill with the remaining being 100% density, the flexural strength is ~5 MPa less. The flexural strength of B3 is less close to that of 100% infill than for modulus where it matches the 100% infill value.

5.3.8 Fibre Direction

Flexural modulus and flexural strength are compared between samples D1-3 in Figures Figure 5.3.8:1 and Figure 5.3.8:2, respectively.

5.3.8.1 Flexural Modulus

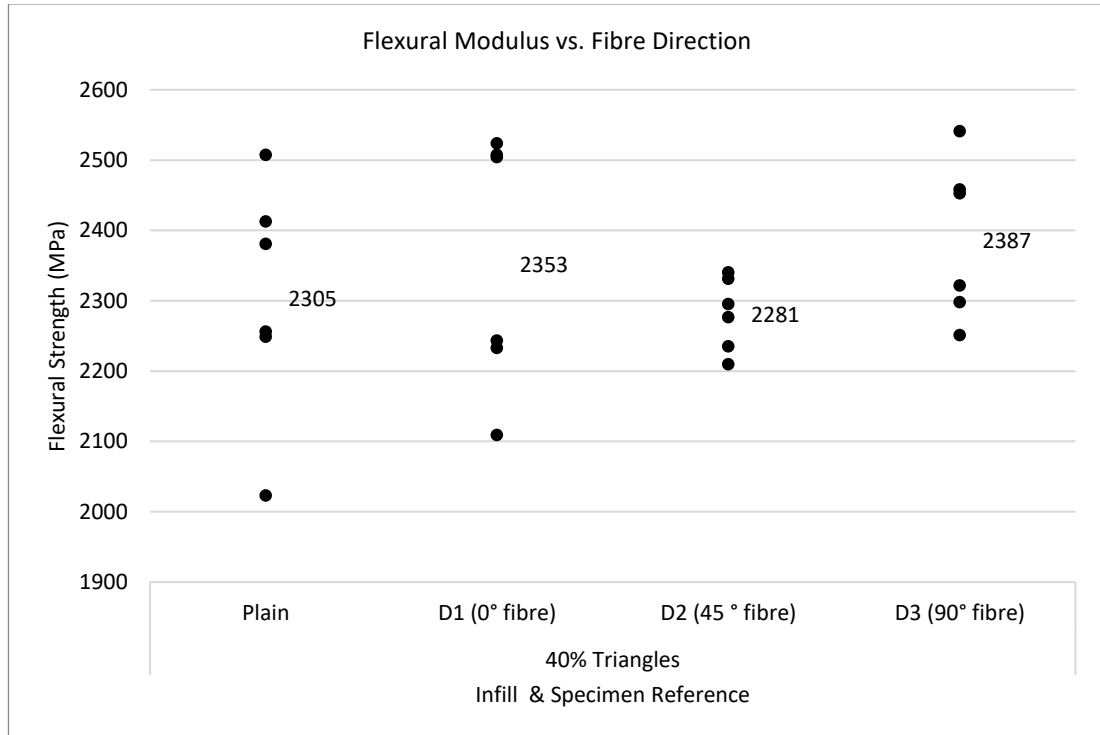


Figure 5.3.8:1 Change in flexural modulus with fibre direction within the structure. Fibre direction seems to have little impact or, in the case of the fibre at 45°, is detrimental to flexural modulus, although it is difficult to do a full comparison with the splits.

The direction of the embedded fibre is shown to have a mixed impact on flexural modulus, with the greatest difference between the plain sample and 90° fibre with a 3.6% increase. Both sample sets D1 and D3 show the split between the 2 sets of samples.

D2 does not display this split and has the smallest variance at 47.34 MPa indicating that the fibre embedding method for a 45° fibre is less critical. However, D2 also shows a lower flexural modulus than the plain sample by 24 MPa implying an embedded fibre at 45° to the structure is detrimental to the flexural modulus. The cause of this may be due to the fibre being aligned with the triangular infill raster lines. Figure 5.3.8:2 shows a μ CT slice of a fibre at 0° to the structure and an infill example with lines indicating how a fibre may lay when embedded at 45° to the structure. The solid line shows a fibre aligned with a raster line which may result in the fibre being displaced by the print nozzle, as seen with the concentric and 0° infill shown in Figure 5.1.2:1 and Figure 5.1.4:1. The dashed line shows a -45° fibre which bisects the triangular infill and is less prone to being displaced.

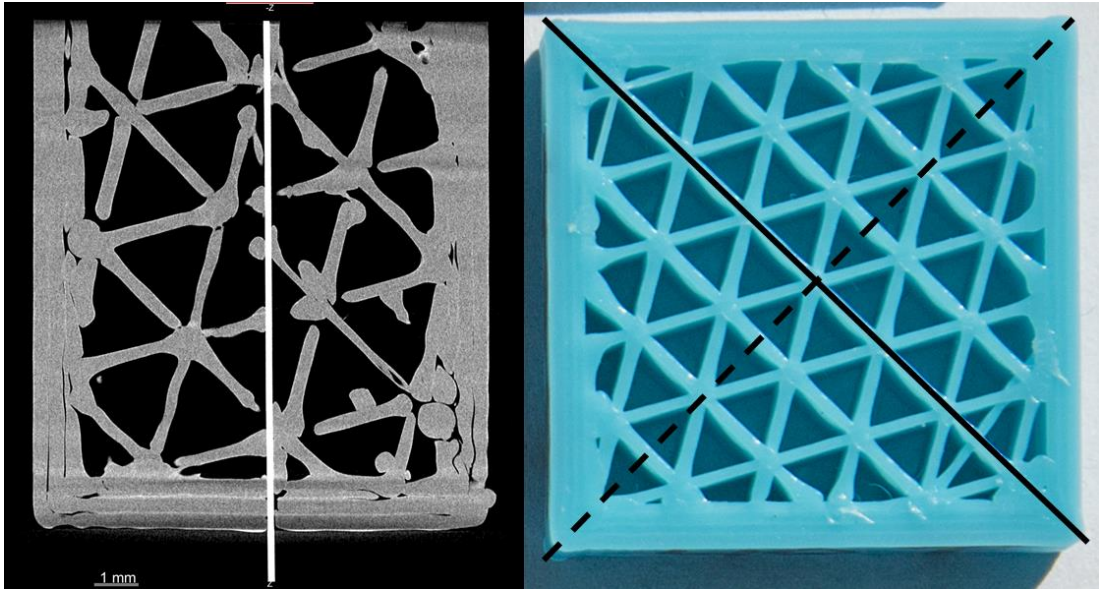


Figure 5.3.8:2 45° fibre options with triangular infill. (Left) CT image showing embedded fibre at 0° through the centre of the sample has not been displaced. (Right) The solid line shows a fibre at 45° and matches one of the raster angles possibly causing the nozzle to displace the fibre. The dashed line is at -45° and bisects the triangular infill possibly prevent the fibre from being affected by the nozzle.

5.3.8.2 Flexural Strength

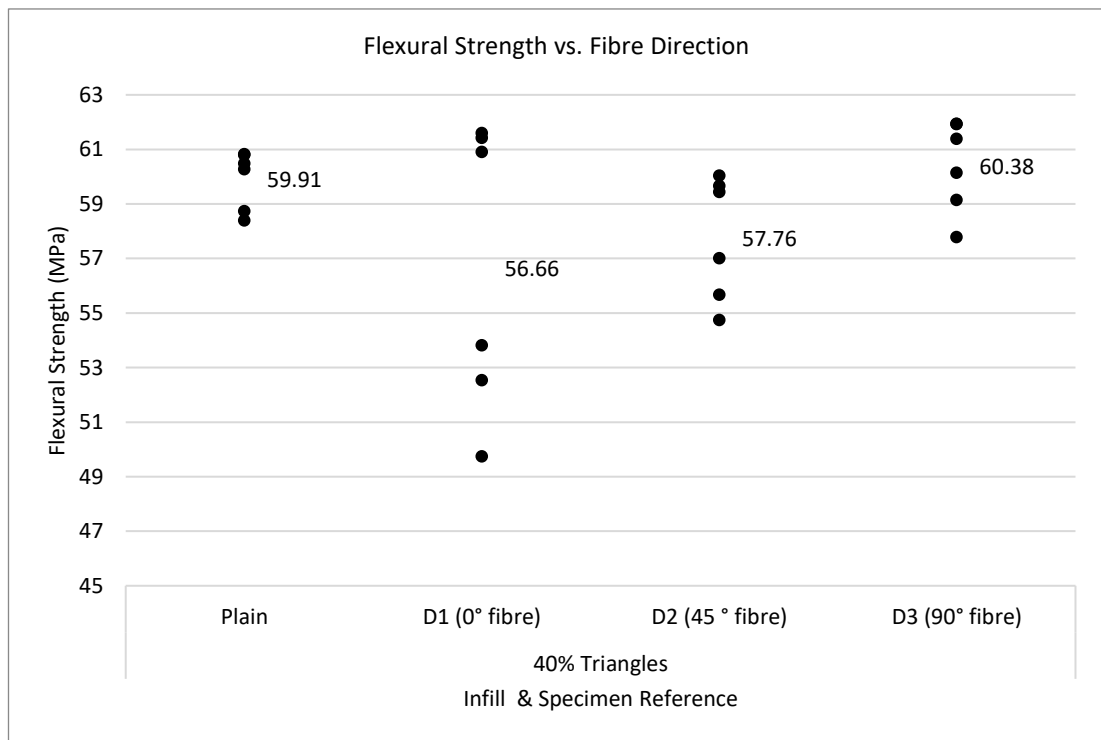


Figure 5.3.8:3 Flexural strength vs. fibre direction. As with modulus, a distinct split between sample sets is seen for D1 and in this instance, the split is observed for D2 as well. A split can be seen in D3 but to a lesser extent than in the modulus chart. These splits lead to difficulty in comparison with the plain sample.

The sample separation is clear for D1 and D2 with the second set showing the higher values.

The split in D3 is less pronounced in this instance.

Both D1 and D2 show a reduction in flexural strength by 5.4% and 3.6% respectively, sample D3 strength is increased by 0.78%, all when compared to the plain sample.

If the second, higher value set of samples are considered then sample D1 shows values slightly above that of the plain whilst D2 has equal values to plain.

The plain samples show the lowest variance with a standard deviation of 0.98 MPa.

5.3.9 Flexural Mass Modulus Ratios

As with tensile samples, a mass modulus ratio has been calculated for tensile results by dividing the flexural modulus (MPa) by the sample mass (g). Higher values show a more effective use of material. Table 5.3.9-1 shows Flexural Mass-Modulus Ratios (MMR_F) for all samples, calculated by dividing the flexural modulus by the sample mass. This gives an indication of the material efficiency in terms of flexural modulus.

Table 5.3.9-1 Mass modulus ratios for flexural samples.

Infill Parameters		Mass (g)	Flexural modulus (MPa)	Flexural Mass Modulus Ratio (MPa/g)	
Plain	20%	Cubic	2.17	2176	1004
		Grid	2.17	2259	1043
		Triangles	2.30	2130	926
	40%	Cubic	2.80	2329	832
		Grid	2.77	2305	833
		Triangles	2.77	2305	833
	80%	Cubic	3.60	2580	717
		Grid	3.55	2538	715
		Triangles	3.58	2481	692
		Concentric	3.63	2768	762
	100%	Lines	4.00	2774	693
	Fibre	40% Triangles	A1	2.70	2353
80% Concentric		A2	3.48	2937	843
Extra Layers		B1	3.15	2532	804
		B2	3.30	2318	702
		B3	3.77	2774	736
Fibre Direction		D1	2.67	2353	882
		D2	2.67	2281	855
		D3	2.68	2387	889

Figure 5.3.9:1 graphically displays MMR_F values. Circles represent plain samples and triangles fibre samples. Lines connect plain samples for cubic, grid and triangles infill between 20, 40 and 80% infill to visualise the decreasing trend as density increases.

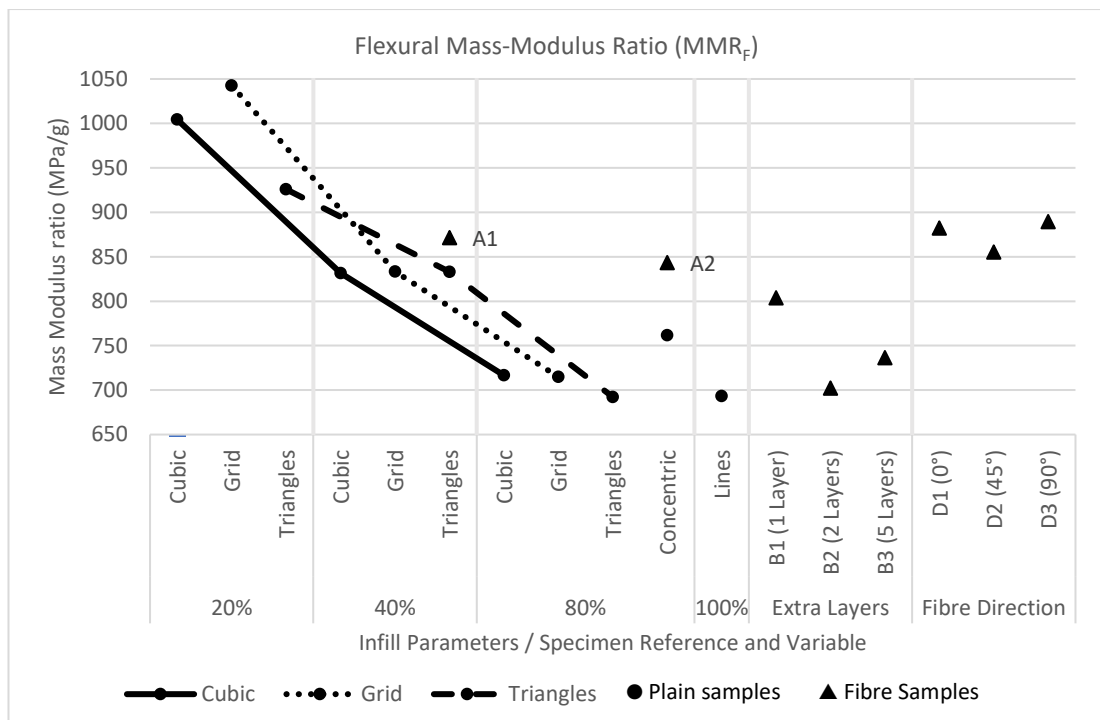


Figure 5.3.9:1 Flexural mass modulus ratios. This gives an indication of the material efficiency in terms of flexural modulus. Cubic, grid and triangles infill at 20, 40 and 80% density are connected to highlight the declining trend as infill density increases. Samples A1 and A2 are placed in columns with their plain counterparts and labelled. Triangles represent fibre inclusive samples, circles for plain samples.

At 20% infill grid infill shows the highest ratio at 1040 MPa/g and triangles the worst at 926 MPa/g. At 40% infill, there is a significant decline as mass increases by a greater proportion than the modulus. Ratios are equivalent for grid and triangles infill at 833 MPa/g with cubic at 832 MPa/g. Doubling the infill density again to 80% all three infill ratios decrease to 717, 715 and 692 MPa/g for cubic, grid and triangles, respectively. 80% concentric infill shows a ratio somewhere between 40 and 80% infill density of the three standard patterns. This shows that simply increasing infill density is an inefficient use of the added mass. It also indicates that the infill pattern is far less critical at the higher infill densities.

100% infill has a MMR_F value of 1 MPa/g higher than 80% triangles infill. Even though it exhibits the greatest flexural modulus it is the least efficient use of material. If the mass is a design consideration, 100% infill should be avoided.

The fibre equivalent samples, A1 and A2, show higher MMR_F values than their plain counterparts. 4.7% greater for A1 and 10.6% for A2. In both instances, the fibre samples were measured to be lighter in mass than the plain samples and had greater flexural modulus values.

Samples B1-3 with additional layers show mixed results. The addition of 2 layers (B1) results in the MMR_F value of 804 MPa/g, between plain 80% concentric infill and the fibre equivalent,

A2. Increasing the total number of additional layers to 4 causes the MMR_F to drop to 702 MPa/g, just above that shown by plain 100% infill. Sample B3 with 10 total additional layers increases the MMR_F to 736 MPa/g. This suggests a small amount of additional material within a sample would be an efficient way to increase flexural modulus. However, flexural modulus values for sample B2 were unexpectedly low and, as previously stated, may offer cause to suggest a manufacturing error.

Fibre direction samples (D1-3) have similar MMR_F values, with 45° fibre being the lowest. The 3 sample types have similar values to A1 and mass values are within 0.03g of one another. Their MMR_F are all above that of plain 40% infill samples.

5.3.10 Flexural Summary

- The importance of the fibre embedding process is shown by the split between results of the first set of 3 samples and the second, for samples A1, A2 and D1-3. This makes it difficult to draw a complete summary of the results presented.
- Further micro-CT imaging of samples prior to testing may show the difference in the separately produced samples. E.g. the unintuitive results are shown by samples B2.
- Infill seems to be more critical than if a fibre is present or not.
- Samples were printed in the XY plane, as with tensile specimens. This results in layer lines being perpendicular to the flexural loading only.
- 80% concentric and 100% infill displayed the highest flexural properties among plain samples, being similar in modulus and strength.
- Fibre containing 80% concentric infill shows higher strength and modulus values 100% plain infill.
- The addition of fibre to 40% triangular infill increases flexural modulus but lowers flexural strength.
- Additional material surrounding the fibre generally improves flexural properties. However, samples B2 with 4 total additional layers show an unexpected result which may be due to manufacturing error. Micro-CT could have been used to investigate samples before testing.
- It is unsuitable to say if fibre improves variance in flexural testing due to the split results.
- Fibre direction has a mixed impact. In terms of flexural modulus, both 0° and 90° increase the value. 45° fibre reduces the modulus compared to the plain equivalent sample but shows a closer spread of results. In terms of flexural strength, fibre at 0° and 45° reduce the value. Fibre at 90° shows a small improvement in strength. Fibre direction may have different impacts depending on the infill pattern and could be investigated further.
- For mass efficiency, lower infill densities are better, with grid being the most efficient infill pattern.
- At 20% infill density, the infill pattern is shown to have a larger impact than at 40 and 80%.
- Fibre samples have better MMR_f values than samples without fibre.
- Concentric infill shows better mass efficiency than the other 80% infill patterns.
- 100% infill is not an efficient use of material with regards to flexural properties.

- The direction of fibre in the specimen makes little difference to material efficiency. Fibre weighs a negligible amount relative to the specimen. It is more critical to optimise material usage.

5.4 Comparison with Material Vendor Specifications

Experimental results have been compared to values supplied by the material vendor, ICE Filaments. Table 5.3.10-1 lists specifications supplied by the material vendor, alongside experimental results obtained from 100% infill plain samples. The vendor's specifications do not state how test samples were manufactured, only the relevant ISO standard.

Table 5.3.10-1 Vendor material specifications vs. experimental result. Experimental results obtained from the plain 100% infill sample set.

Property	Manufacturer's Standard	Manufacturer's Value	Experimental Standard	Experimental Value
Yield Stress	ISO 527	69.8 MPa	ISO 527-2012	31.97 MPa
Strain at yield	ISO 527	4.8%	ISO 527-2012	1.38%
Strain a break	ISO 527	19.5%	ISO 527-2012	2.1%
Tensile modulus	ISO 527	3120 MPa	ISO 527-2012	2720 MPa
Impact Strength	ISO 179	3.4 kJ/m ²	Not Tested	Not Tested

Experimental values are shown to be significantly lower than the manufacturer's stated values. Initial testing revealed appreciably different results for different colours of the same material, which may contribute to the different values seen. Section 3.2.1 shows how even similar printing parameters can lead to vastly different mechanical results.

A request for further information was sent to the material vendor. It was confirmed that testing was performed on printed samples as opposed to the stock filament or bulk material. Information on printing hardware or software was not shared, with only a printing parameter guidance sheet offered as shown in Appendix F - Material Vendor Print Guidance.

This further highlights the difficulty of obtaining and comparing AM mechanical properties if not all manufacturing details are provided.

5.5 Fibre Pull-out

5.5.1 Tabulated Values

Result values for fibre pull-out testing are shown in Table 5.5.1-1. Initial pull-free force is obtained from the first peak value displayed in the force-displacement curve. Max pull-out force is the highest force value found on the same curve as they are not equal in all instances.

Table 5.5.1-1 Mean values for fibre pull-out testing. Initial pull-out force is taken from the first peak of the force/displacement curve. In some instances, the tensile force then increases above this value resulting in a different max force.

Sample	Length (mm)	Initial Pull-Free Force (N)	Std. Dev. (N)	Initial Pull-Free Force Per Unit Length (N/mm)	Max Pull-Out Force (N)	Std.Dev. (N)	Max Force Per Unit Length (N/mm)
A1	50.09	1.13	0.20	0.02	1.28	0.24	0.03
A2	50.08	6.94	3.20	0.14	6.94	3.20	0.14
B1	50.08	6.30	2.60	0.13	6.50	2.35	0.13
B2	50.08	5.94	0.06	0.12	7.60	1.13	0.15
B3	49.98	10.50	2.60	0.21	10.50	2.60	0.21
C1	50.14	6.59	1.46	0.13	6.61	1.43	0.13
C2	50.05	6.54	0.86	0.13	6.88	0.51	0.14
C3	50.95	6.01	3.84	0.12	6.82	2.73	0.13
E1	50.05	6.54	0.86	0.13	6.88	0.51	0.14
E2	50.07	6.30	4.05	0.13	6.30	4.05	0.13
E3	50.02	8.57	1.05	0.17	8.57	1.05	0.17

5.5.2 Pull-Free Force

Figure 5.5.2:1 shows a composite chart of force vs. displacement for samples B1a, B2b and C1a. Each curve shows an example of different force behaviour after the initial pull-free peak.

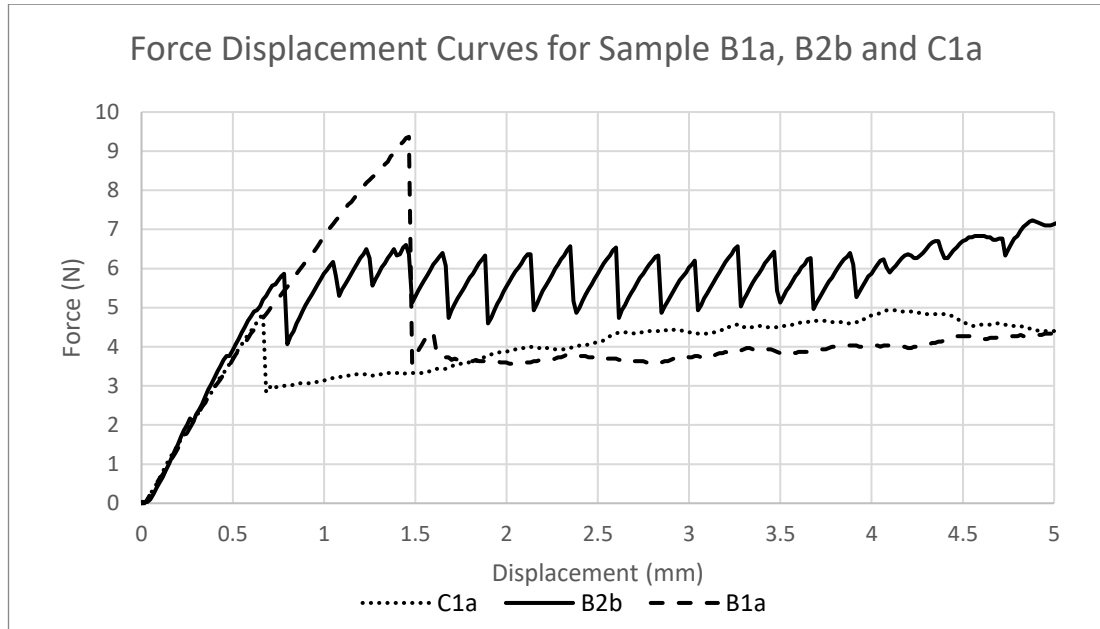


Figure 5.5.2:1 Force displacement curve for samples B1a, B2b and C1a. B1a shows an ideal example of the tensile force increasing up to the first peak at which point the fibre slips and breaks free of the surrounding material. After this point, a relatively consistent force is required to continue pulling the fibre through the sample. Here the pull free force = maximum force. Line B2b displays a continually rising and falling force value. This suggests the fibre is being pulled in a juddering motion rather than a constant force and smooth motion. Curve C1a shows the same expected initial peak as any form of bonding between the fibre and bulk material is overcome. However, the force required to move the fibre increases. In this instance, the maximum pull force \neq pull-free force.

Even though B1a and B2b are similar in construction, the force exerted on the fibre shows very different behaviour. B1a shows a consistent force value as the fibre is pulled following the initial peak, likely after any bonding between fibre and matrix is overcome and broken. Sample B2b shows force values rising and dropping continually in a sawtooth pattern, suggesting the fibre is not able to slide smoothly within the matrix. Curve C1a shows force values gradually rising up to and slightly beyond the initial pull free force.

The expected chart shape would be that of B1a, where a consistent force is required to pull the fibre through the matrix once the bonding between the fibre and matrix is broken. The sawtooth pattern displayed by B2b may be due to an inconsistency on the fibre, possibly caused during manufacturing, resulting in force growing to overcome resistance then slipping forward. The heat generated by friction may be an influencing factor for the gradual increase in curve C1a. Reasons as to why these different patterns are generated is speculation without further study.

Figure 5.5.2:2 shows pull-free force per sample unit length in N/mm. This accounts for variation in sample length.

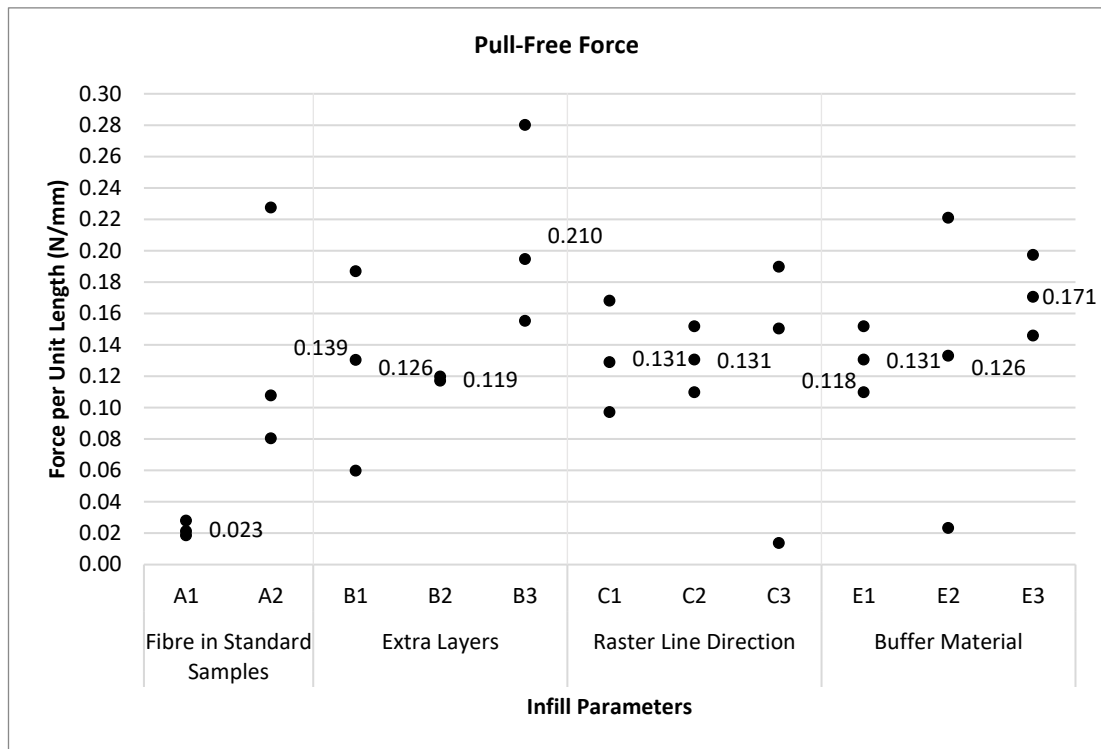


Figure 5.5.2:2 Pull-free force per unit length for each tested sample. Mean values are also shown. No clear conclusion can be determined from the presented data. The method of fibre embedding was done manually and may have a significant impact on the pull-free force. A more robust and repeatable method may be required to produce reliable results.

Most samples show large deviations in pull-free force. Sample A1 shows the second lowest deviation and lowest force value but also has the least material immediately surrounding the fibre with 40% triangle infill throughout the sample. The highest value is shown by sample B3; however, this cannot be said to be caused by the high infill density as sample E1 has the same fibre type and consists of greater infill density with the same raster line directions. This combined with the results of B1 and B2 indicates that the infill density of the sample may not impact the required force to pull free the fibre.

5.5.3 Pull-out Summary

From the data obtained sample B3 with 100% density surrounding layers required the greatest force and sample A1 the least. Vastly different force plots were seen even for samples of the same variable type making it difficult to draw a comprehensive conclusion with the data obtained.

This indicates a more robust testing procedure should be developed. Suggestions include:

- Development of a more consistent and repeatable method of fibre embedding.

- A smaller load cell. 10.5 N was the highest observed force using a 1 kN load cell.
- A larger number of samples.

5.6 Results Summary

- Micro-CT X-ray imaging was shown to be a successful way to image and visualise internal structures of PLA FDM printed specimens. Optical fibres of all tested buffer types were visible within the PLA matrix.
- Infill patterns axial to the fibre as well as fibre diameters larger than the layer height resulted in fibre being displaced from the intended path.
- 100% requested infill density still results in voids being present.
- Fibre is shown to have a larger impact on samples with lower infill densities.
- Unless material vendors will supply full details regarding material testing, mechanical property values should not be assumed to be accurate.

5.6.1 Recommended Actions

- A single embedded optical fibre has beneficial mechanical effects in most situations. As the intention is not to reinforce the structure with optical fibre, greater consideration should be towards the selected infill pattern and density. The selective addition of extra material in key points could improve mechanical properties in a material efficient manner.
- Use concentric infill for printed components with known loading scenarios resulting in tensile forces axial to the infill pattern or flexural forces perpendicular to the infill.
- The layer height of a printed component should be greater than the diameter of the embedded fibre to avoid fibre displacement.
- 100% infill may be a good option if the loading scenario is unknown or if print time, component mass and material usage are not a restriction.

5.6.2 Additional Considerations

- Mechanical testing was carried out on purely tensile or purely flexural samples. Real-world loading scenarios are likely to be a mixture of these and other loading directions.
- Printing times are not considered.
- Only one sample of each type was subject to micro-CT. Imaging of all samples before and after testing would allow a more comprehensive investigation.

6 Further Work

Realized shortcomings of the work in this project, recommended opportunities for continuation of this project and other relatable research paths are suggested.

6.1 Improvement to the Work Done in this Project

Narrow the number of fibre sample variables and focus on key differences between fibre and plain samples:

The range of sample types was chosen to be wide to give insight into the effects of embedded optical fibre. In some instances, further samples would have enabled more detailed comparisons. E.g. Fibre and plain samples at several infill densities with equal infill patterns to investigate if an embedded fibre makes an impact at all structure densities. Equivalent plain samples to B1-3 to determine if properties change due to the added layers or if the fibre still has an impact.

More robust manufacturing process:

The development of a more repeatable fibre embedding process would enable a better comparison of results. Highlighted by the split of results in flexural testing.

6.2 Continuation of this Project

Multiple fibre integration:

This project investigated a single embedded fibre. Multiple fibres would be a next logical step.

Fibre surface treatment:

Prior to insertion, fibres were cleaned with alcohol. Other possibilities include removing or roughing the buffer material.

Arbitrary fibre pathing:

Fibres were embedded in a straight line through the approximate centre, at the mid-layer of samples. Different fibre paths or integration into different layers were not explored.

Print orientations:

Samples in this project were printed in the XY plane. Printing fibre samples with their longest axis in the Z-axis would give insight into whether fibre improves properties perpendicular to the laminate layers. The fibre embedding procedure would have to be solved.

Different materials (matrix and fibre):

PLA was the only tested print material. Other materials may be differently affected by an embedded fibre. Likewise, with fibres (e.g. POF) and buffer materials.

Optical fibre pull-out:

Fibre pull-out results showed large variance and various force plots. More comprehensive testing and perhaps a more specialised testing procedure may allow better understanding. Micro-CT imaging could be utilized after the pull-out testing to investigate the structure.

Fibre-matrix interface materials:

A separate material could be applied before fibre embedding to improve bonding between the fibre and matrix. A form of adhesive would be an obvious starting point.

6.3 Future Opportunities

Automation of embedding process:

Fibres were manually embedded during this project; automation of this manufacturing step would allow more consistent samples to be produced but may be difficult as the optical fibre cannot be cut within the structure.

Slicer modification to consider fibre integration:

Open source slicer software could be modified to consider the fibre during slicing.

3 axis integration of fibre:

Embedding of optical fibres in 3 axes would require significant hardware and software modification but enable significant opportunities for smart fibre embedded components.

FEA/simulation of manufacturing processes:

Computer simulation of material deposition around the fibre could enable rapid optimisation of print parameters and fibre routing.

Post-processing of fibre samples:

Post-processing options such as vapour or heat treatment may improve fibre embedding.

7 Conclusion

As specified in the introduction, a number of project objectives were defined. Firstly, overviews of Additive Manufacturing, Fibre Optics and X-ray Micro-CT imaging were given to allow the reader a general understanding of the 3 major technologies employed in this project. AV Optics' ECHOES report was presented in a summarised format to highlight some of the possibilities and explore the potential offered by the combination of AM and optical fibre technologies.

A literature review explored the current state of the art regarding fibre integration within AM components. Most notably discovered was the apparent lack of specific research regarding the mechanical impacts of embedded optical fibres in FDM printed structures. Also deemed necessary was the testing of plain samples with the available hardware and material, due to both the lack of standardisation of AM part testing and wide variations in results from existing research.

Following the literature review, a methodology was devised to produce a broad set of results to lay the foundation for understanding the mechanical impacts of embedded optical fibre. Standard tensile and flexural mechanical testing was selected, and a fibre pull-out test method was devised to investigate bond strength between fibre and matrix material. Micro-CT imaging steps were also detailed to allow internal visualisation of an embedded optical fibre.

Results were presented in Chapter 5 and divided by test type. X-ray micro-CT was successfully used to visualise an embedded optical fibre and images were grouped and displayed by their variable parameter. Pertinent features were discussed and compared within each group. A large number of tensile and flexural results were displayed in chart format to offer a wide scope for future readers. Mass modulus ratios were devised and presented for tensile and flexural samples to better visualise the mass efficiency of different infill and fibre parameters. Fibre pull-out values were successfully obtained and displayed as a force per unit length but did not present conclusive data. For each testing method, different infill and fibre parameters were compared and discussed along with plain samples. Each results section was summarised in bullet point format for easy reference and a final results summary in the same manner alongside suggested actions and considerations based on the project findings.

Finally, suggestions were made for further work to improve the research produced in this project, a continuation of this study and related research opportunities with a larger scope.


Ultimately this project investigated the mechanical impacts of a single, manually embedded fibre optic in PLA printed via FDM. In reality, there exist many different methods of AM, printable materials and options for fibre embedding. This research project is the beginning of understanding the mechanical impacts of embedded optical fibres and offers an opportunity to extend the research in many directions.

Some key aspects can be stated to quantify the knowledge obtained during this study:

- In general, the inclusion of a single fibre at the mid-layer improves tensile and flexural mechanical properties.
- Embedded fibre is shown to have more impact on mechanical properties when infill density is lower.
- The infill shape has a significant impact on the quality of the fibre embedding. Infills with raster lines running axially to the fibre can cause the fibre to be displaced.
- The type of fibre diameter and buffer should be selected to match the printing parameters. Fibre diameter should not exceed the desired layer height to prevent fibre displacement and fibre buffer material should be chosen to have an operating temperature greater than the print temperature.
- Hence, the quality fibre embedding process is critical to performance.
- Concentric infill, with or without fibre, shows better tensile properties and similar flexural properties compared to full density samples.
- The inclusion of fibre at 40% infill improves all presented tensile properties and reduces variance. Fibre addition at 80% reduces modulus and UTS values by a small margin and increases proof stress, also by a small amount.
- A combination of an embedded optical fibre and increased infill density can improve mechanical properties to above that of 100% infill density.
- An optical fibre embedded into PLA should have strain relief external to the structure considered if tension on the fibre is expected.
- Material vendor mechanical specifications should not be taken as accurate and individual testing carried out as required. Material colour is also an aspect of consideration.

Appendices

Appendix A – Optical Fibre Specifications



SM Fiber

VERSION: MD24/5
RELEASE DATE: 09 MARCH 2016

Datasheet

Polyimide Coated SM Fiber

Fibercore's range of polyimide coated, bend-insensitive Single-Mode (SM) fibers are specifically designed for use in harsh environments. The fibers target micro-seismic "fracking" sensors

16000
1000
0.14NA 0.30NA

Related Products:

- SM Fiber for Visible RGB Through to Near IR (SM)
- High Temperature Acrylate Coated SM Fiber (SM-HT)
- Pure Silica Core SM Fiber (SM-SC)
- Photosensitive Fiber (PS)

SM1500(7.8/80)P for micro-acoustic "tracking sensors"

"Bridging fiber" for reduced splice losses between sensor fibers and telecoms fibers

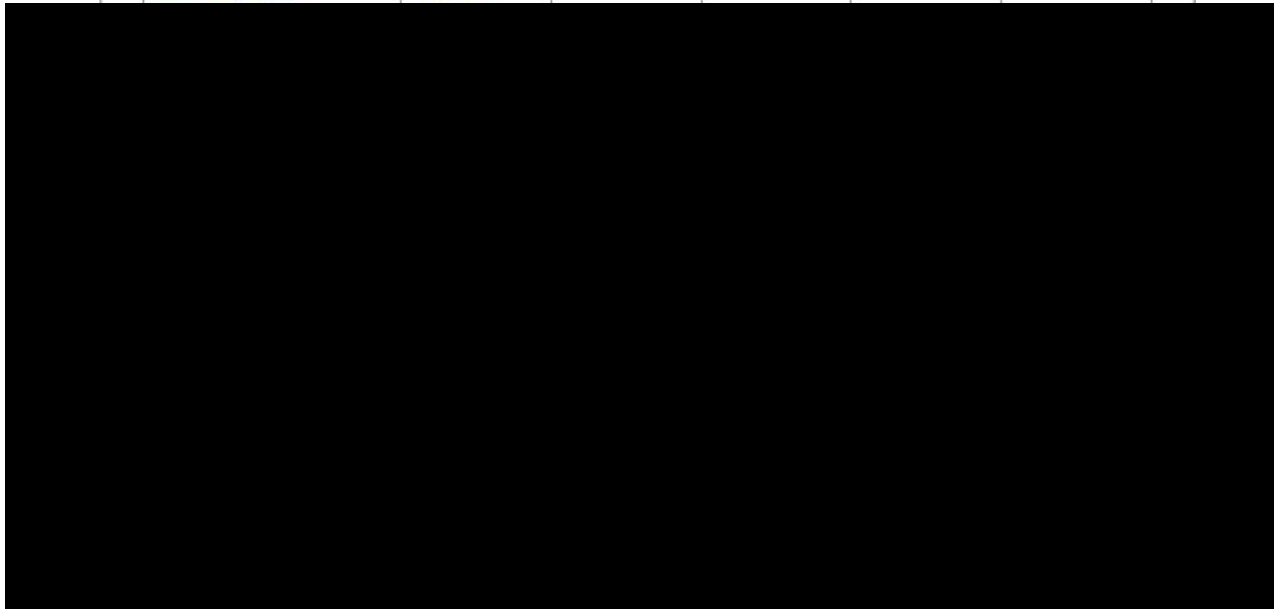
T: +44 (0)23 8076 9993
E: info@fibercore.com
www.fibercore.com

FIBERCORE
Insight | Innovation | Integrity



Specifications

	SM1250(10.4/125)P	SM1500(4.2/125)P	SM1500(6.4/125)P	SM1500(7.8/125)P	SM1500(9/125)P
Operating Wavelength (nm)	1260 - 1650	1520 - 1650			
Cut-Off Wavelength (nm)	1190 - 1330	1350 - 1520			
Numerical Aperture	0.11 - 0.14	0.29 - 0.31	0.19 - 0.21	0.15 - 0.17	0.13 - 0.15
Mode Field Diameter (µm)	9.6 - 11.2 @1550nm	4.0 - 4.5 @1550nm	6.0 - 6.8 @1550nm	7.4 - 8.6 @1550nm	8.5 - 9.9 @1550nm



Visit fibercore.com/fiberpaedia for our encyclopedia of industry terms/knowledge base.



T: +44 (0)23 8076 9893
 E: info@fibercore.com
www.fibercore.com



Corning® ClearCurve® Multimode Optical Fiber

Product Information



Bend Performance and Compatibility

Corning® ClearCurve® ultra-bendable, laser-optimized™ multimode optical fiber delivers enhanced macrobending performance while maintaining compatibility with current optical fibers, equipment, practices and procedures. ClearCurve® OM₂, OM₃ and OM₄ multimode fiber is designed to withstand tight bends and challenging cabling routes with substantially less signal loss than conventional multimode fiber.

How to Order

Contact your sales representative, the Optical Fiber Service Department. Ph: 1-607-248-4444 or +44-1244-534343. Email: cofic@corning.com. Please specify the attenuation, and quantity when ordering.

Numerical Aperture
0.200 ± 0.015

Dimensional Specifications

Glass Geometry		Coating Geometry	
Core Diameter	50.0 ± 2.5 μm	Coating Diameter	242 ± 5 μm
Cladding Diameter	125.0 ± 1.0 μm	Coating-Cladding Concentricity	< 12 μm
Core-Clad Concentricity	≤ 1.5 μm		
Cladding Non-Circularity	≤ 1.0%		
Core Non-Circularity	≤ 5%		

PI1468

ISSUED: JULY 2014
SUPERSEDES: JANUARY 2014

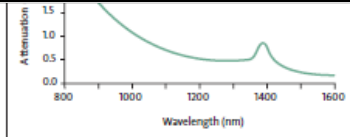
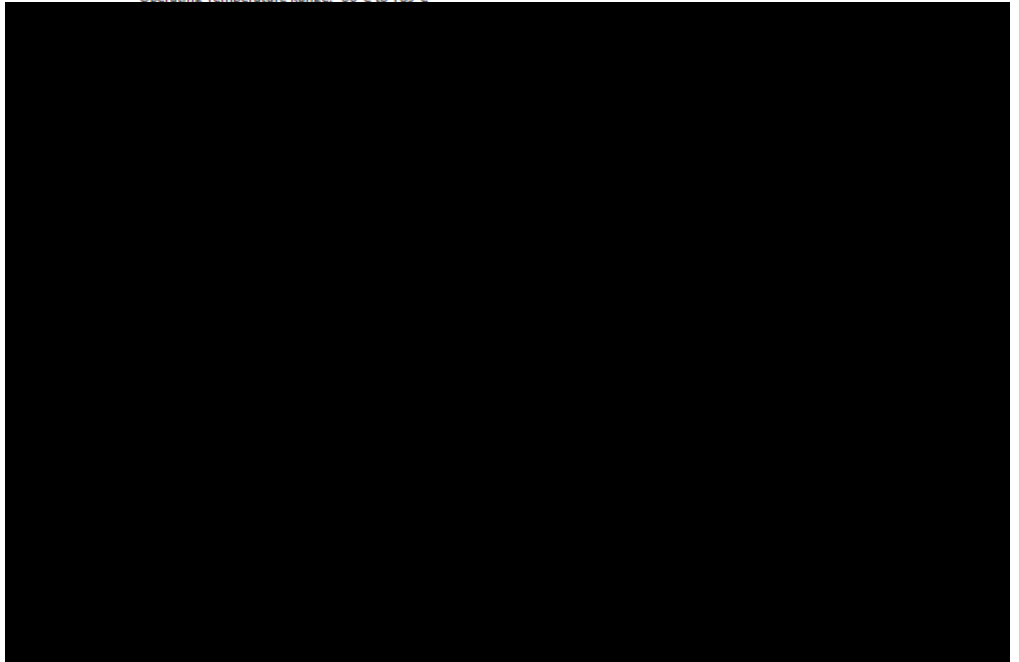
TL9000/ISO 9001 CERTIFIED



Environmental Specifications

Environmental Test	Test Condition	Induced Attenuation 850 & 1300 nm (dB/km)
Temperature Dependence	-60°C to +85°C*	≤ 0.10
Temperature Humidity Cycling	-10°C to +85°C and 4% to 98% RH	≤ 0.10
Water Immersion	23°C ± 2°C	≤ 0.20
Heat Aging	85°C ± 2°C	≤ 0.20
Damp Heat	85°C at 85% RH	≤ 0.20

*Reference temperature = +23°C
Operating Temperature Range: -60°C to +85°C



CORNING

Corning Incorporated
One Riverfront Plaza
Corning, NY 14831 U.S.A.
Ph: 607-248-2000 (U.S. and Canada)
+44-1244-525-320 (Europe)
Email: cofic@corning.com
www.corning.com/opticalfiber

Corning and ClearCurve are registered trademarks of Corning Incorporated, Corning, NY.
© 2014 Corning Incorporated. All Rights Reserved.



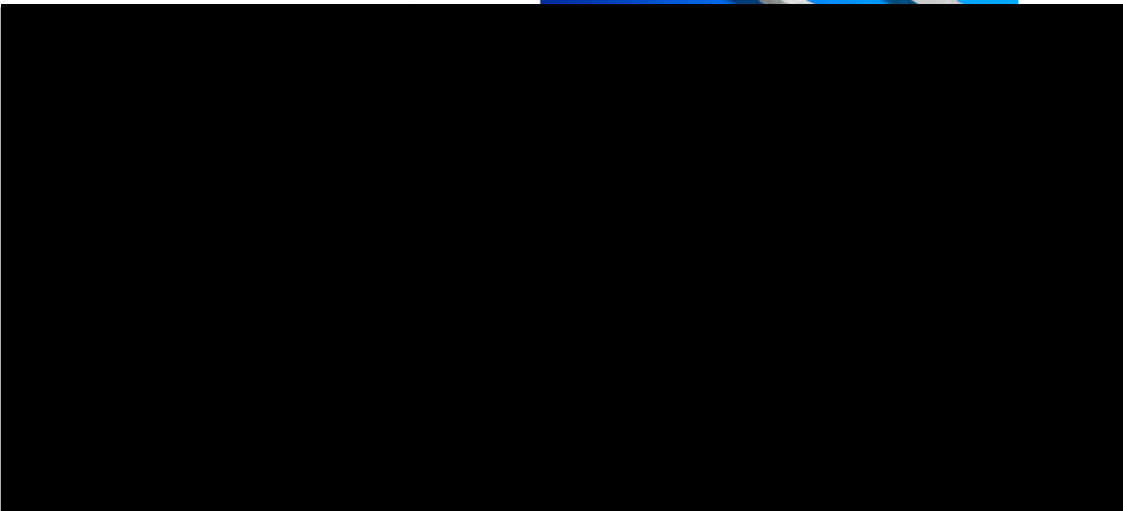
GORE Aerospace Fiber Optic Cables

Technical Note

Reliable signal transmission in challenging environments

Engineered with a unique buffering system, GORE® Aerospace Fiber Optic Ribbon Cables provide durable protection in challenging conditions while maintaining high-speed communication on avionics networks. These cables deliver reliable signal transmission in temperatures ranging from -60°C to 135°C (Tables 1 and 2).

The smaller construction of GORE® Aerospace Fiber Optic Ribbon Cables provides increased flexibility with a tight bend radius for easy installation in confined areas of an aircraft. These cables



ELECTRICAL/MECH/ENVIRO	Core/Cladding/Coating	02.5/125/250	50/125/243	02.5/125/243	50/125/243	62.5/125/245	
	Jacket Color	White				Orange	
	Overall Diameter mm (in)	0.245 (0.01)					
	Overall Thickness mm (in)	0.45 (0.018)				2.29 (0.090)	
	Minimum Bend Radius mm (in)	30 (1.18)					
	Temperature Range (°C)	-60 to 135			-60 to 85		

¹ Cables are available in a variety of configurations. Product specifications are for typical configurations.

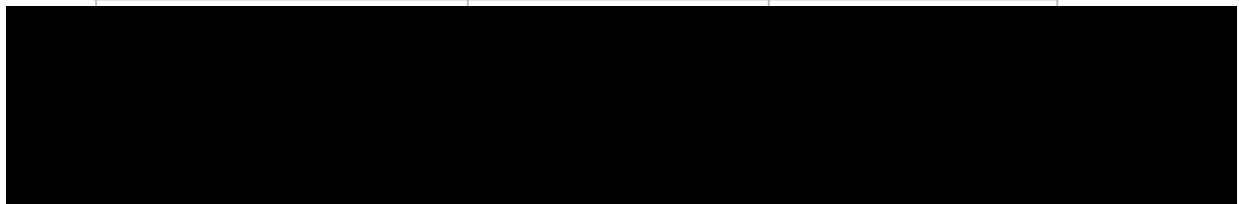


GORE Aerospace Fiber Optic Cables

Technical Note

TABLE 2: QUALIFICATIONS SUMMARY

Examination or Test	Standard	Status
Humidity	MIL-STD-202, Method 103	Passed
Salt Fog	MIL-STD-810, Method 509	Passed
Sand and Dust	MIL-STD-210	Passed
Flammability	FAR25.869	Passed



Dynalene HC-50 coolant		
Synthetic Lube		

ORDERING INFORMATION

For more information regarding specific design requirements or to place an order for GORE® Aerospace Fiber Optic Ribbon Cables, submit a request at www.gore.com/contact.

NOTICE — USE RESTRICTIONS APPLY
Not for use in food, drug, cosmetic or medical device manufacturing, processing, or packaging operations.

W. L. Gore & Associates

GORE and designs are trademarks of W. L. Gore & Associates. ©2015 W. L. Gore & Associates, Inc. ACS-0149-040-US-SEP15

gore.com



Appendix B – Cura 4.0.0 Fibre Printing Profile Settings

Cura Version	4.0.0	
Profile	Fibre printing	
Quality	Normal	
Material Extruder : 1	PLA	
Material estimation	89.1 g	
Printing Time	0 d 6 h 41 mn	
Extruder : 1 Quality		
Layer Height	0.2	mm
Initial Layer Height	0.27	mm
Line Width	0.35	mm
Wall Line Width	0.35	mm
Outer Wall Line Width	0.35	mm
Inner Wall(s) Line Width	0.35	mm
Top/Bottom Line Width	0.35	mm
Infill Line Width	0.35	mm
Skirt/Brim Line Width	0.35	mm
Support Line Width	0.35	mm
Support Interface Line Width	0.35	mm
Support Roof Line Width	0.35	mm
Support Floor Line Width	0.35	mm
Prime Tower Line Width	0.35	mm
Initial Layer Line Width	100	%
Extruder : 1 Shell		
Wall Extruder	-1	
Outer Wall Extruder	-1	
Inner Wall Extruder	-1	
Wall Thickness	0.7	mm
Wall Line Count	3	
Outer Wall Wipe Distance	0.2	mm
Top Surface Skin Extruder	-1	
Top Surface Skin Layers	0	
Top/Bottom Extruder	-1	
Top/Bottom Thickness	0.75	mm
Top Thickness	0.75	mm
Top Layers	3	
Bottom Thickness	0.75	mm
Bottom Layers	3	
Top/Bottom Pattern	lines	
Bottom Pattern Initial Layer	lines	
Connect Top/Bottom Polygons	FALSE	
Top/Bottom Line Directions	[]	
Outer Wall Inset	0.025	mm
Optimize Wall Printing Order	FALSE	
Outer Before Inner Walls	FALSE	

Alternate Extra Wall	FALSE	
Compensate Wall Overlaps	TRUE	
Compensate Outer Wall Overlaps	TRUE	
Compensate Inner Wall Overlaps	TRUE	
Minimum Wall Flow	0	%
Prefer Retract	FALSE	
Fill Gaps Between Walls	everywhere	
Filter Out Tiny Gaps	TRUE	
Print Thin Walls	FALSE	
Horizontal Expansion	0	mm
Initial Layer Horizontal Expansion	0	mm
Z Seam Alignment	sharpest_corner	
Z Seam X	111.5	mm
Z Seam Y	669	mm
Seam Corner Preference	z_seam_corner_inner	
Z Seam Relative	FALSE	mm
Ignore Small Z Gaps	FALSE	
Extra Skin Wall Count	1	
Enable Ironing	FALSE	
Iron Only Highest Layer	FALSE	
Ironing Pattern	zigzag	
Ironing Line Spacing	0.1	mm
Ironing Flow	10	%
Ironing Inset	0.175	mm
Ironing Speed	20	mm/s
Ironing Acceleration	3000	mm/s ²
Ironing Jerk	20	mm/s
Extruder : 1 Infill		
Infill Extruder	-1	
Infill Density	40	%
Infill Line Distance	2.625	mm
Infill Pattern	triangles	
Connect Infill Lines	FALSE	
Connect Infill Polygons	FALSE	
Infill Line Directions	[]	
Infill X Offset	0	mm
Infill Y Offset	0	mm
Infill Line Multiplier	1	
Extra Infill Wall Count	0	
Cubic Subdivision Shell	0.35	mm
Infill Overlap Percentage	10	%
Infill Overlap	0.035	mm
Skin Overlap Percentage	5	%
Skin Overlap	0.0175	mm
Infill Wipe Distance	0.0875	mm
Infill Layer Thickness	0.2	mm

Gradual Infill Steps	0	
Gradual Infill Step Height	1.5	mm
Infill Before Walls	TRUE	
Minimum Infill Area	0	mm ²
Infill Support	FALSE	
Infill Overhang Angle	40	°
Skin Removal Width	1.05	mm
Top Skin Removal Width	1.05	mm
Bottom Skin Removal Width	1.05	mm
Skin Expand Distance	1.05	mm
Top Skin Expand Distance	1.05	mm
Bottom Skin Expand Distance	1.05	mm
Maximum Skin Angle for Expansion	90	°
Minimum Skin Width for Expansion	0	mm
Extruder : 1 Material		
Default Printing Temperature	200	°C
Printing Temperature	200	°C
Printing Temperature Initial Layer	200	°C
Initial Printing Temperature	190	°C
Final Printing Temperature	185	°C
Extrusion Cool Down Speed Modifier	0.7	°C/s
Default Build Plate Temperature	60	°C
Build Plate Temperature	60	°C
Build Plate Temperature Initial Layer	60	°C
Adhesion Tendency	0	
Surface Energy	100	%
Shrinkage Ratio	0	%
Flow	100	%
Initial Layer Flow	100	%
Enable Retraction	TRUE	
Retract at Layer Change	FALSE	
Retraction Distance	6.5	mm
Retraction Speed	25	mm/s
Retraction Retract Speed	25	mm/s
Retraction Prime Speed	25	mm/s
Retraction Extra Prime Amount	0	mm ³
Retraction Minimum Travel	0.7	mm
Maximum Retraction Count	90	
Minimum Extrusion Distance Window	6.5	mm
Limit Support Retractions	TRUE	
Standby Temperature	175	°C
Nozzle Switch Retraction Distance	20	mm
Nozzle Switch Retraction Speed	20	mm/s
Nozzle Switch Retract Speed	20	mm/s
Nozzle Switch Prime Speed	20	mm/s
Extruder : 1 Speed		

Print Speed	60	mm/s
Infill Speed	60	mm/s
Wall Speed	50	mm/s
Outer Wall Speed	40	mm/s
Inner Wall Speed	50	mm/s
Top Surface Skin Speed	30	mm/s
Top/Bottom Speed	30	mm/s
Support Speed	40	mm/s
Support Infill Speed	40	mm/s
Support Interface Speed	26.6667	mm/s
Support Roof Speed	26.6667	mm/s
Support Floor Speed	26.6667	mm/s
Prime Tower Speed	60	mm/s
Travel Speed	150	mm/s
Initial Layer Speed	30	mm/s
Initial Layer Print Speed	30	mm/s
Initial Layer Travel Speed	75	mm/s
Skirt/Brim Speed	30	mm/s
Maximum Z Speed	0	mm/s
Number of Slower Layers	2	
Equalize Filament Flow	FALSE	
Maximum Speed for Flow Equalization	150	mm/s
Enable Acceleration Control	FALSE	
Print Acceleration	3000	mm/s ²
Infill Acceleration	3000	mm/s ²
Wall Acceleration	3000	mm/s ²
Outer Wall Acceleration	3000	mm/s ²
Inner Wall Acceleration	3000	mm/s ²
Top Surface Skin Acceleration	3000	mm/s ²
Top/Bottom Acceleration	3000	mm/s ²
Support Acceleration	3000	mm/s ²
Support Infill Acceleration	3000	mm/s ²
Support Interface Acceleration	3000	mm/s ²
Support Roof Acceleration	3000	mm/s ²
Support Floor Acceleration	3000	mm/s ²
Prime Tower Acceleration	3000	mm/s ²
Travel Acceleration	5000	mm/s ²
Initial Layer Acceleration	3000	mm/s ²
Initial Layer Print Acceleration	3000	mm/s ²
Initial Layer Travel Acceleration	5000	mm/s ²
Skirt/Brim Acceleration	3000	mm/s ²
Enable Jerk Control	FALSE	
Print Jerk	20	mm/s
Infill Jerk	20	mm/s
Wall Jerk	20	mm/s
Outer Wall Jerk	20	mm/s

Inner Wall Jerk	20	mm/s
Top Surface Skin Jerk	20	mm/s
Top/Bottom Jerk	20	mm/s
Support Jerk	20	mm/s
Support Infill Jerk	20	mm/s
Support Interface Jerk	20	mm/s
Support Roof Jerk	20	mm/s
Support Floor Jerk	20	mm/s
Prime Tower Jerk	20	mm/s
Travel Jerk	30	mm/s
Initial Layer Jerk	20	mm/s
Initial Layer Print Jerk	20	mm/s
Initial Layer Travel Jerk	30	mm/s
Skirt/Brim Jerk	20	mm/s
Extruder : 1 Travel		
Combing Mode	all	
Max Comb Distance With No Retract	0	mm
Retract Before Outer Wall	FALSE	
Avoid Printed Parts When Traveling	TRUE	
Avoid Supports When Traveling	FALSE	
Travel Avoid Distance	0.6562	mm
Start Layers with the Same Part	FALSE	
Layer Start X	0	mm
Layer Start Y	0	mm
Z Hop When Retracted	FALSE	
Z Hop Only Over Printed Parts	FALSE	
Z Hop Height	1	mm
Z Hop After Extruder Switch	TRUE	
Extruder : 1 Cooling		
Enable Print Cooling	TRUE	
Fan Speed	100	%
Regular Fan Speed	100	%
Maximum Fan Speed	100	%
Regular/Maximum Fan Speed Threshold	10	s
Initial Fan Speed	0	%
Regular Fan Speed at Height	0.27	mm
Regular Fan Speed at Layer	2	
Minimum Layer Time	5	s
Minimum Speed	10	mm/s
Lift Head	FALSE	
Support		
Generate Support	FALSE	
Support Extruder	0	
Support Infill Extruder	0	
First Layer Support Extruder	0	

Support Interface Extruder	0	
Support Roof Extruder	0	
Support Floor Extruder	0	
Support Placement	everywhere	
Support Overhang Angle	50	°
Support Pattern	zigzag	
Support Wall Line Count	0	
Connect Support Lines	FALSE	
Connect Support ZigZags	TRUE	
Support Density	15	%
Support Line Distance	2.3333	mm
Initial Layer Support Line Distance	2.3333	mm
Support Infill Line Direction	0	°
Enable Support Brim	FALSE	
Support Brim Width	8	mm
Support Brim Line Count	23	
Support Z Distance	0.1	mm
Support Top Distance	0.1	mm
Support Bottom Distance	0.1	mm
Support X/Y Distance	0.7	mm
Support Distance Priority	z_overrides_xy	
Minimum Support X/Y Distance	0.2	mm
Support Stair Step Height	0.3	mm
Support Stair Step Maximum Width	5	mm
Support Join Distance	2	mm
Support Horizontal Expansion	0.2	mm
Support Infill Layer Thickness	0.2	mm
Gradual Support Infill Steps	0	
Gradual Support Infill Step Height	1	mm
Minimum Support Area	0	mm ²
Enable Support Interface	FALSE	
Enable Support Roof	FALSE	
Enable Support Floor	FALSE	
Support Interface Thickness	1	mm
Support Roof Thickness	1	mm
Support Floor Thickness	1	mm
Support Interface Resolution	0.3	mm
Support Interface Density	100	%
Support Roof Density	100	%
Support Roof Line Distance	0.35	mm
Support Floor Density	100	%
Support Floor Line Distance	0.35	mm
Support Interface Pattern	concentric	
Support Roof Pattern	concentric	
Support Floor Pattern	concentric	
Minimum Support Interface Area	1	mm ²

Minimum Support Roof Area	1	mm ²
Minimum Support Floor Area	1	mm ²
Support Interface Horizontal Expansion	0	mm
Support Roof Horizontal Expansion	0	mm
Support Floor Horizontal Expansion	0	mm
Fan Speed Override	FALSE	
Supported Skin Fan Speed	100	%
Use Towers	TRUE	
Tower Diameter	3	mm
Minimum Diameter	3	mm
Tower Roof Angle	65	°
Drop Down Support Mesh	TRUE	
Build Plate Adhesion		
Enable Prime Blob	FALSE	
Extruder Prime X Position	0	mm
Extruder Prime Y Position	0	mm
Build Plate Adhesion Type	brim	
Build Plate Adhesion Extruder	0	
Skirt Line Count	1	
Skirt Distance	3	mm
Skirt/Brim Minimum Length	250	mm
Brim Width	8	mm
Brim Line Count	15	
Brim Replaces Support	TRUE	
Brim Only on Outside	TRUE	
Raft Extra Margin	15	mm
Raft Smoothing	5	mm
Raft Air Gap	0.3	mm
Initial Layer Z Overlap	0.15	mm
Raft Top Layers	2	
Raft Top Layer Thickness	0.2	mm
Raft Top Line Width	0.35	mm
Raft Top Spacing	0.35	mm
Raft Middle Thickness	0.3	mm
Raft Middle Line Width	0.7	mm
Raft Middle Spacing	0.9	mm
Raft Base Thickness	0.324	mm
Raft Base Line Width	0.8	mm
Raft Base Line Spacing	1.6	mm
Raft Print Speed	30	mm/s
Raft Top Print Speed	30	mm/s
Raft Middle Print Speed	22.5	mm/s
Raft Base Print Speed	22.5	mm/s
Raft Print Acceleration	3000	mm/s ²
Raft Top Print Acceleration	3000	mm/s ²

Raft Middle Print Acceleration	3000	mm/s ²
Raft Base Print Acceleration	3000	mm/s ²
Raft Print Jerk	20	mm/s
Raft Top Print Jerk	20	mm/s
Raft Middle Print Jerk	20	mm/s
Raft Base Print Jerk	20	mm/s
Raft Fan Speed	0	%
Raft Top Fan Speed	0	%
Raft Middle Fan Speed	0	%
Raft Base Fan Speed	0	%
Extruder : 1 Mesh Fixes		
Union Overlapping Volumes	TRUE	
Remove All Holes	FALSE	
Extensive Stitching	FALSE	
Keep Disconnected Faces	FALSE	
Merged Meshes Overlap	0.15	mm
Remove Mesh Intersection	FALSE	
Alternate Mesh Removal	TRUE	
Remove Empty First Layers	TRUE	
Special Modes		
Print Sequence	all_at_once	
Infill Mesh	FALSE	
Infill Mesh Order	0	
Cutting Mesh	FALSE	
Mold	FALSE	
Minimal Mold Width	5	mm
Mold Roof Height	0.5	mm
Mold Angle	40	°
Support Mesh	FALSE	
Anti Overhang Mesh	FALSE	
Surface Mode	normal	
Spiralize Outer Contour	FALSE	
Smooth Spirialized Contours	TRUE	
Relative Extrusion	FALSE	
Experimental		
Tree Support	FALSE	
Tree Support Branch Angle	40	°
Tree Support Branch Distance	1	mm
Tree Support Branch Diameter	2	mm
Tree Support Branch Diameter Angle	5	°
Tree Support Collision Resolution	0.175	mm
Tree Support Wall Thickness	0.35	mm
Tree Support Wall Line Count	1	
Slicing Tolerance	middle	
Top Surface Skin Line Width	0.35	mm
Top Surface Skin Pattern	lines	

Top Surface Skin Line Directions	[]	
Infill Travel Optimization	FALSE	
Auto Temperature	FALSE	
Flow Temperature Graph	[[3.5,200],[7.0,240]]	[[mm ³ ,°C]]
Minimum Polygon Circumference	1	mm
Maximum Resolution	0.01	mm
Maximum Travel Resolution	0.025	mm
Break Up Support In Chunks	FALSE	
Support Chunk Size	20	mm
Support Chunk Line Count	9	
Enable Draft Shield	FALSE	
Draft Shield X/Y Distance	10	mm
Draft Shield Limitation	full	
Draft Shield Height	10	mm
Make Overhang Printable	FALSE	
Maximum Model Angle	50	°
Enable Coasting	FALSE	
Coasting Volume	0.064	mm ³
Minimum Volume Before Coasting	0.8	mm ³
Coasting Speed	90	%
Alternate Skin Rotation	FALSE	
Cross 3D Pocket Size	2.625	mm
Cross Infill Density Image		
Cross Fill Density Image for Support		
Spaghetti Infill	FALSE	
Spaghetti Infill Stepping	TRUE	
Spaghetti Maximum Infill Angle	10	°
Spaghetti Infill Maximum Height	2	mm
Spaghetti Inset	0.2	mm
Spaghetti Flow	20	%
Spaghetti Infill Extra Volume	0	mm ³
Enable Conical Support	FALSE	
Conical Support Angle	30	°
Conical Support Minimum Width	5	mm
Fuzzy Skin	FALSE	
Fuzzy Skin Thickness	0.3	mm
Fuzzy Skin Density	1.25	1/mm
Fuzzy Skin Point Distance	0.8	mm
Flow rate compensation max extrusion offset	0	mm
Flow rate compensation factor	100	%
Wire Printing	FALSE	
WP Connection Height	5	mm
WP Roof Inset Distance	5	mm
WP Speed	5	mm/s
WP Bottom Printing Speed	5	mm/s

WP Upward Printing Speed	5	mm/s
WP Downward Printing Speed	5	mm/s
WP Horizontal Printing Speed	5	mm/s
WP Flow	100	%
WP Connection Flow	100	%
WP Flat Flow	100	%
WP Top Delay	0	s
WP Bottom Delay	0	s
WP Flat Delay	0.1	s
WP Ease Upward	0.3	mm
WP Knot Size	0.6	mm
WP Fall Down	0.5	mm
WP Drag Along	0.6	mm
WP Strategy	compensate	
WP Straighten Downward Lines	20	%
WP Roof Fall Down	2	mm
WP Roof Drag Along	0.8	mm
WP Roof Outer Delay	0.2	s
WP Nozzle Clearance	1	mm
Use adaptive layers	FALSE	
Adaptive layers maximum variation	0.1	mm
Adaptive layers variation step size	0.01	mm
Adaptive layers threshold	200	
Overhanging Wall Angle	90	°
Overhanging Wall Speed	100	%
Enable Bridge Settings	FALSE	
Minimum Bridge Wall Length	5	mm
Bridge Skin Support Threshold	50	%
Bridge Wall Coasting	100	%
Bridge Wall Speed	20	mm/s
Bridge Wall Flow	50	%
Bridge Skin Speed	15	mm/s
Bridge Skin Flow	60	%
Bridge Skin Density	100	%
Bridge Fan Speed	100	%
Bridge Has Multiple Layers	TRUE	
Bridge Second Skin Speed	15	mm/s
Bridge Second Skin Flow	100	%
Bridge Second Skin Density	75	%
Bridge Second Skin Fan Speed	0	%
Bridge Third Skin Speed	15	mm/s
Bridge Third Skin Flow	110	%
Bridge Third Skin Density	80	%
Bridge Third Skin Fan Speed	0	%
Machine		
Machine Type	Ultimaker 2+	

Show Machine Variants	TRUE	
Start G-code		
Material GUID	506c9f0d-e3aa-4bd4-b2d2-23e2425b1aa9	
Diameter	2.85	mm
Wait for Build Plate Heatup	TRUE	
Wait for Nozzle Heatup	TRUE	
Include Material Temperatures	TRUE	
Include Build Plate Temperature	TRUE	
Machine Width	223	
Machine Depth	223	
Build Plate Shape	rectangular	
Build Plate Material	glass	
Machine Height	205	
Has Heated Build Plate	TRUE	
Is Center Origin	FALSE	
Number of Extruders	1	
Number of Extruders that are enabled	1	
Outer nozzle diameter	1.05	mm
Nozzle length	5	mm
Nozzle angle	45	°
Heat zone length	20	mm
Filament Park Distance	20	mm
Enable Nozzle Temperature Control	FALSE	
Heat up speed	2	°C/s
Cool down speed	2	°C/s
Minimal Time Standby Temperature	50	s
G-code flavour	UltiGCode	
Firmware Retraction	TRUE	
Nozzle Disallowed Areas	[]	
Machine head polygon	[[-1, 1], [-1, -1], [1, -1], [1, 1]]	
Machine head & Fan polygon	[[-44, 14], [-44, -34], [64, 14], [64, -34]]	
Gantry height	52	
Nozzle ID	unknown	
Nozzle Diameter	0.4	mm
Offset With Extruder	TRUE	
Extruder Prime Z Position	0	mm
Absolute Extruder Prime Position	FALSE	
Maximum Speed X	300	mm/s
Maximum Speed Y	300	mm/s
Maximum Speed Z	40	mm/s
Maximum Feedrate	45	mm/s
Maximum Acceleration X	9000	mm/s ²
Maximum Acceleration Y	9000	mm/s ²
Maximum Acceleration Z	100	mm/s ²
Maximum Filament Acceleration	10000	mm/s ²

Default Acceleration	3000	mm/s ²
Default X-Y Jerk	20	mm/s
Default Z Jerk	0.4	mm/s
Default Filament Jerk	5	mm/s
Steps per Millimeter (X)	50	
Steps per Millimeter (Y)	50	
Steps per Millimeter (Z)	50	
Steps per Millimeter (E)	1600	
X Endstop in Positive Direction	FALSE	
Y Endstop in Positive Direction	FALSE	
Z Endstop in Positive Direction	TRUE	
Minimum Feedrate	0	mm/s
Feeder Wheel Diameter	10	mm
Extruder : 1 Machine		
Extruder	0	
Nozzle ID	unknown	
Nozzle Diameter	0.4	mm
Nozzle X Offset	0	mm
Nozzle Y Offset	0	mm
Extruder Start G-Code		
Extruder Start Position Absolute	FALSE	
Extruder Start Position X	0	mm
Extruder Start Position Y	0	mm
Extruder End G-Code		
Extruder End Position Absolute	FALSE	
Extruder End Position X	0	mm
Extruder End Position Y	0	mm
Extruder Prime Z Position	0	mm
Extruder Print Cooling Fan	0	

Appendix C – Filament Specification

Material vendor PLA filament data sheet.



ICE FILAMENTS PLA PRODUCT CARD

ICE Filaments PLA is a tough, easy to use high grade PLA type of filament, ideal for 3D printing. Slightly modified, the filament retains the typical features of PLA, but makes it tougher and less brittle. Due to a low shrinkage factor ICE Filaments PLA will not deform after cooling. Poly lactic acid is a biodegradable plastic made from renewable natural resources and one of the most popular materials for 3D printing.

FEATURES:

- Tougher and less brittle
- Easy to print at low temperature
- Low warping
- Biodegradable
- Limited smell



COLOURS:

ICE Filaments PLA is available from stock in a variety of colors. Other colors on request.



Impact Strength – Charpy notched 23°C	ISO 179	3,4 kJ/m ²
Moisture absorption	ISO 62	1968 ppm
Printing temperature	ICE FILAMENTS	180 – 210°C
Melting temperature	ISO 11357	77 – 146°C
Vicat softening temperature	ISO 306	60°C
Glass transition temperature	ISO 11357	57°C

ADDITIONAL INFO:

Due to its low tendency to warp ICE Filaments PLA can also be printed without a heated bed. If you have a heated bed, the recommended temperature is $\pm 35 - 60^{\circ}\text{C}$.

ICE Filaments PLA can be used on all common desktop FDM or FFF technology 3D printers.

Storage: cool and dry (15 – 25°C) and away from UV light. This enhances the shelf life significantly.

Appendix D – Tensile Modulus Correction

Tensile samples requiring modulus calculation correction.

Sample (Tensile)				Tensile Modulus (MPa)	Tensile Modulus with correction (MPa)	
Plain	20%	Cubic	2	1522	1472	
			1	1460	1417	
		Grid	2	1526	1488	
			4	1478	1441	
			6	1596	1555	
			1	1563	1562	
		Triangles	3	1596	1542	
			4	1542	1513	
			6	1614	1543	
			2	1629	1607	
		40%	Cubic	3	1693	1678
				4	1740	1735
	5			1735	1701	
	2			1630	1596	
	Grid		4	1646	1628	
			5	1700	1670	
			6	1742	1719	
			3	1650	1632	
	Triangles		5	1677	1658	
			1	2147	2144	
	80%		Cubic	2	2116	2140
				1	2339	2342
		Triangles	4	2286	2304	
			1	2955	3042	
		Concentric	4	2765	2786	
			5	2863	2913	
			1	2666	2685	
		100%	Lines	2	2748	2720
				3	2669	2679
				6	2827	2850
	1			2666	2685	

Appendix E – Flexural Modulus Correction

Flexural samples requiring modulus calculation correction.

Sample (Flexural)				Flexural Modulus (MPa)	Flexural Modulus with correction (MPa)
Plain	20%	Cubic	1	2197.23	1965.29
		Grid	1	2227.10	2049.00
	40%	Grid	2	2274.94	1465.46
			3	2350.48	1477.16
			4	2375.83	1793.58
			5	2312.49	1855.31
			6	2353.83	1553.87
			6	2412.52	1585.48
		Triangles	3	2248.33	2110.30
			4	2022.62	1789.17
			5	2380.70	1707.57
			6	2507.35	1690.47
	80%	Concentric	1	2769.86	2542.26
			5	2972.13	2668.82

Appendix F - Material Vendor Print Guidance for PLA

Version: 07/06/2019

	Nozzle size	Bed adhesion	Print temp.	Bed temp.	Layer height	Print speed	Fan speed	Flowrate	Retraction	Difficulty	Drying	Special	Food Approval EU*	FDA**
mcpp Power to Perform	PLA	PEI, glass, hairspray or gluestick	205±10°C	≤60°C	±0.1mm	Medium/high	Medium/high	100%	DD: ±2mm BT: ±5mm	Easy	Optional	-	Yes	Yes
	PLA GLITTER	PEI, glass, hairspray or gluestick	205±10°C	≤60°C	±0.1mm	Medium/high	Medium/high	100%	DD: ±2mm BT: ±5mm	Easy	Optional	-	No	No
	PLA MATT	PEI, glass, hairspray or gluestick	215±10°C	≤60°C	±0.1mm	Medium/high	Medium/high	105%	DD: ±2mm BT: ±5mm	Easy	Optional	Hardened steel nozzle advised	No	No
	PLA SATIN	PEI, glass, hairspray or gluestick	225±10°C	50-70°C	±0.1mm	Medium	Medium/high	95%	DD: ±1.5mm BT: ±6mm	Easy	Optional	-	-	-

Bibliography

- [1] Matias E, Rao B. 3D printing: On its historical evolution and the implications for business. *PICMET; 2015 Aug 2-6; Portland, OR, USA. IEEE*; pp. 551-58. Available from: <https://doi.org/10.1109/PICMET.2015.7273052>
- [2] Durakovic B. Design for additive manufacturing: Benefits, trends and challenges. *Periodicals of Engineering and Natural Sciences* [Internet]. 2018 [cited 2020 May 20]; 6(2): 171-91. Available from: <http://dx.doi.org/10.21533/pen.v6i2.224>
- [3] Saari M, Cox B, Galla M et al. Multi-material additive manufacturing of robot components with integrated sensor arrays. *Proc. SPIE 9494, Next-Generation Robotics II; and Machine Intelligence and Bio-inspired Computation: Theory and Applications IX; 2015 Jun 18; Baltimore, MD, USA. SPIE; 2015*. Available from: <https://doi.org/10.1117/12.2179507>
- [4] Hong C, Zhang Y, Borana L. Design, Fabrication and Testing of a 3D Printed FBG Pressure Sensor. *IEEE Access* [Internet]. 2019 [cited Sep 2020]; 7:38577-83. Available from: [10.1109/ACCESS.2019.2905349](https://doi.org/10.1109/ACCESS.2019.2905349)
- [5] 3Dnatives your source for 3D printing [Internet]. Jamie D.; 2018. Picture, 3D Printing vs CNC Machining: Which is best for prototyping?; [2018 March; cited 2018 December]. Available from: <https://www.3dnatives.com/en/3d-printing-vs-cnc-160320184/>
- [6] Hull CW, UVP Inc. Apparatus for production of three-dimensional objects by stereolithography. USA 4575330, 1986.
- [7] Crump SS, Stratasys Inc. Apparatus and method for creating three-dimensional objects. USA 5121329, 1992.
- [8] Committee F42 on Additive Manufacturing Technologies [Internet]. ASTM INTERNATIONAL; 1996; [cited 2020 September 28] Available from: <https://www.astm.org/COMMITTEE/F42.htm>
- [9] All3DP [Internet]. [Munich]: Leo Gregurić; [date unknown]. 3D Printed Rocket: The Latest Advancements in 2020; [2020 Feb 11; 2020 Sep 23]; Available from: <https://all3dp.com/2/3d-printed-rocket-the-latest-advancements/>
- [10] Relativity Space, Inc. [Internet]. [Los Angeles]: Relativity Space; [cited 2020 Sep 23]. Available from: <https://www.relativityspace.com/>
- [11] Fortune Business Insights [Internet]. [Pune]: [date unknown]. [webpage], Information & Technology / 3D Printing Market; [2020 Jan; cited 2020 Sep 23]; Available from: <https://www.fortunebusinessinsights.com/industry-reports/3d-printing-market-101902>
- [12] Grand View Research [Internet]. [San Francisco]: Grand View Research Inc.; 2020. [webpage], 3D Printing Industry Analysis; [2020 Feb; cited 2020 Sep 23]; Available from <https://www.grandviewresearch.com/industry-analysis/3d-printing-industry-analysis>
- [13] Markets and Markets [Internet]. [Pune]: Markets and Markets; c2020. [webpage], 3D Printing Market by Offering; [2019 Feb; cited 2020 Sep 23]; Available from: <https://www.marketsandmarkets.com/Market-Reports/3d-printing-market-1276.html>

- [14] British Standards Institution. BS EN ISO/ASTM 52900:2017: Additive manufacturing – General principles – Terminology [Internet]. London: BSI; [2020 Sep 19]. Available from: <https://bsol.bsigroup.com/Bibliographic/BibliographicInfoData/00000000030343265>
- [15] 3D Hubs [Internet]. [Amsterdam]: 3D Hubs B.V.; c2020. [Image], The SLA 3D printing process; [cited 2020 Sep 19]; Available from <https://www.3dhubs.com/knowledge-base/introduction-sla-3d-printing/>
- [16] 3D Hubs [Internet]. [Amsterdam]: 3D Hubs B.V.; c2020. [Image], The FDM printing process; [cited 2020 Sep 19]; Available from <https://www.3dhubs.com/knowledge-base/introduction-fdm-3d-printing/>
- [17] Post BK, Chesser PC, Lind RF, et al. Using Big Area Additive Manufacturing to directly manufacture a boat hull mould. *Virtual Phys Prototyp* [Internet]. 2018 [cited 2020 Sep 19]; 14(2):123-29. Available from: <https://doi.org/10.1080/17452759.2018.1532798>
- [18] NASA [Internet]. [Washington, DC]: NASA. [webpage]. 3D-Printed Habitat Challenge; [2020 Jun 24; cited 2020 Sep 28]; Available from: https://www.nasa.gov/directorates/spacetech/centennial_challenges/3DPHab/index.html
- [19] 3D Hubs [Internet]. [Amsterdam]: 3D Hubs B.V.; c2020. [Image], The Material Jetting process; [cited 2020 Sep 29]; Available from: <https://www.3dhubs.com/knowledge-base/introduction-material-jetting-3d-printing/>
- [20] 3D Hubs [Internet]. [Amsterdam]: 3D Hubs B.V.; c2020. [Image], The Binder Jetting process; [cited 2020 Sep 29]; Available from: <https://www.3dhubs.com/knowledge-base/introduction-binder-jetting-3d-printing/>
- [21] 3D Hubs [Internet]. [Amsterdam]: 3D Hubs B.V.; c2020. [Image], The SLM/DMLS printing process; [cited 2020 Sep 29]; Available from: <https://www.3dhubs.com/knowledge-base/introduction-metal-3d-printing/>
- [22] Muniyasamy S, Ofosu O, Jacob John M, et al. Mineralization of Poly (lactic acid) (PLA), Poly (3-hydroxybutyrate-co-valerate) (PHBV) and PLA/PHBV Blend in Compost and Soil Environments. *J Renew Mater* [Internet] 2016 [cited 2020 March 3]; 4(2):133–45. Available from: <https://doi.org/10.7569/JRM.2016.634104>
- [23] Galante R, Figueiredo-Pina CG, Serro AP. Additive manufacturing of ceramics for dental applications: A review. *Dent Mater* [Internet]. 2019 [cited 2020 Sep 29]; 35(6):825–46. Available from: <https://doi.org/10.1016/j.dental.2019.02.026>
- [24] Salet TAM, Ahmed ZY, Bos FP, et al. Design of a 3D printed concrete bridge by testing. *Virtual Phys Prototyp* [Internet] 2018 [cited 2020 Sep 16]; 13(3):222–36. Available from: <https://doi.org/10.1080/17452759.2018.1476064>
- [25] Sanjayan JG, Nematollahi B. 3D Concrete Printing for Construction Applications. In: Sanjayan JG, Nazari A, Nematollahi B, editors. *3D Concrete Printing Technology*. Butterworth-Heinemann; 2019, p. 1–11. Available from: <https://doi.org/10.1016/B978-0-12-815481-6.00001-4>
- [26] Bandyopadhyay A, Bose S, Das S. 3D printing of biomaterials. *MRS Bull* [Internet] 2015 [cited 2020 Sep 23]; 40(2):108-15. Available from: <https://doi.org/10.1557/mrs.2015.3>
- [27] Jang J, Park JY, Gao G, et al. Biomaterials-based 3D cell printing for next-generation therapeutics and diagnostics. *Biomaterials* [Internet]. 2018 [cited 2020 Sep 23]; 156:88–

106. Available from: <https://www.sciencedirect.com/science/article/pii/S0142961217307573?via%3Dihub>

- [28] Chia HN, Wu BM. Recent advances in 3D printing of biomaterials. *J Biol Eng* [Internet]. 2015 [cited 2020 Sep 23]; 9:4. Available from: <https://doi.org/10.1186/s13036-015-0001-4>
- [29] Hällgren S, Pejryd L, Ekengren B. 3D Data Export for Additive Manufacturing - Improving Geometric Accuracy. *Procedia CIRP* [Internet]. 2016 [cited 2021 Apr 6]; 50: 518-23. Available from: <https://doi.org/10.1016/j.procir.2016.05.046>
- [30] FS [Internet]. 2009. [Image], Optical fibre structure; [2012 Oct 20; cited 2020 Sep 29]; Available from: <https://community.fs.com/blog/the-advantages-and-disadvantages-of-optical-fibers.html>
- [31] Read I, AV Optics Limited. ECHOES Phase 1 Final report. Yeovil: AV Optics; 2018.
- [32] Hehr A, Norfolk M, Wenning J, et al. Integrating Fiber Optic Strain Sensors into Metal Using Ultrasonic Additive Manufacturing. *JOM* [Internet]. 2018 [cited 2018 Oct 5]; 70(3):315–20. Available from: <https://doi.org/10.1007/s11837-017-2709-8>
- [33] Maier RRJ, MacPherson WN, Barton JS, et al. Embedded Fiber Optic Sensors Within Additive Layer Manufactured Components. *IEEE Sens J* [Internet]. 2013 [cited 2020 Sep 19]; 13(3):969–79. Available from: <https://doi.org/10.1109/JSEN.2012.2226574>
- [34] Letcher T, Waytashek M. Material Property Testing of 3D-Printed Specimen in PLA on an Entry-Level 3D Printer. Montreal, Quebec, Canada: ASME; 2015. Available from: <https://doi.org/10.1115/IMECE2014-39379>
- [35] Nugroho A, Ardiansyah R, Rusita L, et al. Effect of layer thickness on flexural properties of PLA (PolyLactid Acid) by 3D printing. *J. Phys.: Conf. Ser* [Internet]. 2018 [cited 2020 Sep 19]; 1130. Available from: <https://doi.org/10.1088/1742-6596/1130/1/012017>
- [36] Kim H, Park E, Kim S, et al. Experimental Study on Mechanical Properties of Single- and Dual-material 3D Printed Products. *Procedia Manuf* [Internet]. 2017 [cited 2019 Jun 21]; 10:887–97. Available from: <https://doi.org/10.1016/j.promfg.2017.07.076>
- [37] Patel DM. Effects of Infill Patterns on Time, Surface Roughness and Tensile Strength in 3D Printing. *IJEDR* [Internet] 2017 [cited 2020 Sep 19]; 5(3):566-69.
- [38] Rismalia M, Hidajat SC, Permana IGR, et al. Infill pattern and density effects on the tensile properties of 3D printed PLA material. *J. Phys.: Conf. Ser* [Internet] 2019 [cited 2020 Jul 7]; 1402(4):[6 p.]. Available from: <https://doi.org/10.1088/1742-6596/1402/4/044041>
- [39] Jaya Christiyan KG, Chandrasekhar U, Venkateswarlu K. Flexural Properties of PLA Components Under Various Test Condition Manufactured by 3D Printer. *J. Inst. Eng. India Ser. C* [Internet] 2018 [cited 2020 Jul 7]; 99(3):363–67. Available from: <https://doi.org/10.1007/s40032-016-0344-8>
- [40] Travieso-Rodriguez JA, Jerez-Mesa R, Llumà J, et al. Mechanical Properties of 3D-Printing Polylactic Acid Parts subjected to Bending Stress and Fatigue Testing. *Materials* [Internet]. 2019 [cited 2020 Jul 7]; 12(23):[20 p.]. Available from: <https://doi.org/10.3390/ma12233859>
- [41] 9T Labs [Internet]. Zürich. [Webpage], CarbonKit; [cited 2019 Jan 22]. Available from: <https://www.9tlabs.com/carbonkit/>

- [42] Markforged [Internet]. Watertown: [cited 2019 Jan 22]. Available from: <https://markforged.com/>
- [43] Baumann F, Scholz J, Fleisher J. Investigation of a new approach for additively manufactured continuous fiber-reinforced polymers. *Procedia CIRP* [Internet]. 2017 [cited 2019 Jan 24]; 66:323-28. Available from: <https://doi.org/10.1016/j.procir.2017.03.276>
- [44] Kantaros A, Giannatis J, Karalekas D. A novel strategy for the incorporation of optical sensors in Fused Deposition Modeling parts. Stockholm, Sweden: 2013. Available from: https://www.researchgate.net/publication/269631461_A_novel_strategy_for_the_incorporation_of_optical_sensors_in_FDM_parts
- [45] Kantaros A, Karalekas D. Fiber Bragg grating based investigation of residual strains in ABS parts fabricated by fused deposition modeling process. *Materials & Design* [Internet]. 2013 [cited 2020 Aug 24]; 50:44-50. Available from: <https://doi.org/10.1016/j.matdes.2013.02.067>
- [46] Zelený R, Včelák J. Strain measuring 3D printed structure with embedded fibre Bragg grating. *Procedia Engineering* [Internet]. 2016 [cited 2018 Oct 22]; 168:1338-41. Available from: <https://doi.org/10.1016/j.proeng.2016.11.367>
- [47] Zubel MG, Sugden K, Webb DJ, et al. Embedding silica and polymer fibre Bragg gratings (FBG) in plastic 3D-printed sensing patches. Brussels, Belgium: SPIE; 2016. Available from: <https://doi.org/10.1117/12.2228753>
- [48] Kousiatza C, Karalekas D. In-situ monitoring of strain and temperature distributions during fused deposition modeling process. *Materials and Design* [Internet]. 2016 [cited 2020 Aug 24]; 97:400-06. Available from: <https://doi.org/10.1016/j.matdes.2016.02.099>
- [49] Lima RTP de. Development of Embedded Fiber Bragg Grating Sensors using 3D Printing Technique [master's thesis on the internet]. Porto: University of Porto; 2017 [cited 2020 Oct 19]. Available from: <https://www.semanticscholar.org/paper/Development-of-Embedded-Fiber-Bragg-Grating-Sensors-Lima/ca24b30da99530d35143f7991d0cae60d4176001?p2df>
- [50] Economidou SN, Karalekas D. Characterization of fused deposition modelling polymeric structures using embedded fiber Bragg grating sensors. In: Zhang J, Jung Y-G. *Additive Manufacturing: Materials, Processes, Quantifications and Applications*. Butterworth-Heinemann; 2018. p. 163-180. Available from: <https://doi.org/10.1016/B978-0-12-812155-9.00005-0>
- [51] Leal-Junior A, Casas J, Marques C, et al. Application of Additive Layer Manufacturing Technique on the Development of High Sensitive Fiber Bragg Grating Temperature Sensors. *Sensors* [Internet] 2018 [cited 2019 Jul 30]; 18: [15 p.]. Available from: <https://doi.org/10.3390/s18124120>
- [52] Fauver C, Petrushenko D, Gordon E, et al. *Structural Health Monitoring of Additively Manufactured Parts Using Fiber Bragg Gratings*. Springer, Cham; 2018. Available from: https://doi.org/10.1007/978-3-319-75390-4_18
- [53] Wittbrodt B, Pearce JM. The Effects of PLA Color on Material Properties of 3-D Printed Components. *Additive Manufacturing* [Internet]. 2015 [cited 2020 Sep 19]; 8:110-16. Available from: <https://doi.org/10.1016/j.addma.2015.09.006>

- [54] British Standards Institution. BS EN ISO 527-1:2012: Plastics – Determination of tensile properties Part 1: General principles [Internet]. BSI; [cited 2019 Apr 16]. Available from: <https://shop.bsigroup.com/ProductDetail?pid=00000000030216857>
- [55] British Standards Institution. BS EN ISO 527-2:2012: Plastics - Determination of tensile properties Part 2: Test conditions for moulding and extrusion plastics [Internet]. BSI; [cited 2019 Apr 16]. Available from: <https://shop.bsigroup.com/ProductDetail/?pid=00000000030216860>
- [56] British Standards Institution. BS EN ISO 178:2019: Plastics. Determination of flexural properties [Internet]. BSI; [cited 2020 Sep 19]. Available from: <https://shop.bsigroup.com/ProductDetail?pid=00000000030335678>
- [57] British Standards Institution. BS EN ISO 16012:2015: Plastics - Determination of linear dimensions of test specimens [Internet]. BSI; [cited 2020 Sep 19]. Available from: <https://shop.bsigroup.com/ProductDetail?pid=00000000030322406>